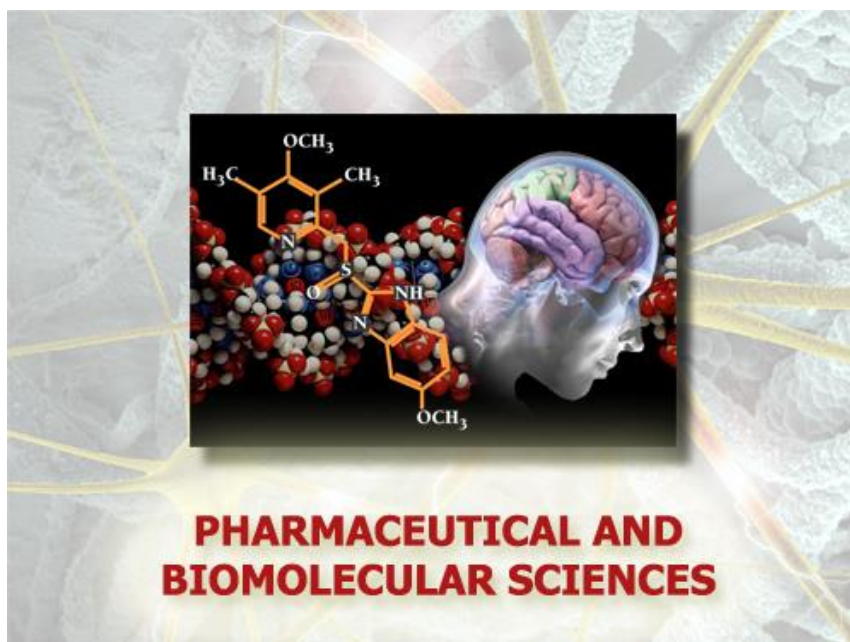**Università degli Studi di Torino**

**Scuola di Dottorato in
Scienze della Natura e Tecnologie Innovative**

Dottorato in
Scienze Farmaceutiche e Biomolecolari
(XXXV ciclo)

Ultrasonic strategy for the preparation of inorganic nanoparticles and controlled drug release

Candidato: Xiaolin Liu   **Tutor: Prof. Giancarlo Cravotto**
Co-Tutor: Prof. Zhilin Wu

Università degli Studi di Torino

Dottorato in
Scienze Farmaceutiche e Biomolecolari

Tesi svolta presso il
Dipartimento di Scienza e Tecnologia del Farmaco

CICLO: XXXV

TITOLO DELLA TESI: Ultrasonic strategy for the preparation of inorganic nanoparticles and controlled drug release

TESI PRESENTATA DA: Xiaolin Liu

TUTOR(S): Professor Giancarlo Cravotto

CO-TUTOR: Professor Zhilin Wu

COORDINATORE DEL DOTTORATO: Professor Roberta Cavalli

ANNI ACCADEMICI: Three years

SETTORE SCIENTIFICO-DISCIPLINARE DI AFFERENZA*: Chimica organica (CHIM/06)

Table of Contents

Preface

The present thesis is an original intellectual product of the author, Xiaolin LIU, submitted for the degree of Doctor in Pharmaceutical and Biomolecular Sciences at the University of Turin (Italy). The research herein was conducted under the supervision of Prof. Giancarlo Cravotto and Prof. Zhilin Wu at the Department of Drug Science and Technology of the University of Turin (Italy), between November 2019 and November 2022.

This research stems from my passion for ultrasonically preparing inorganic nanomaterials. With the continuous development of science and technology, nanomaterials are increasingly used in our daily lives. Ultrasound is a simple, easy-to-operate, and low-cost technique for preparing inorganic nanomaterials.

This doctoral study was funded by the China Scholarship Council and the University of Turin. This thesis has not been submitted for any other degree, diploma, or other qualification at any other university. One part of the investigations has been published in the following peer journal: X. L, Liu, et al., Medium-high frequency sonication dominates spherical-SiO_2 nanoparticle size. Ultrasonics Sonochemistry 90 (2022): 106181. In addition, a review article has been published: X. L. Liu, et al., Sonochemical Preparation of Inorganic Nanoparticles and Nanocomposites for Drug Release–A Review. Industrial & Engineering Chemistry Research 60 (2021): 10011-10032.

Acknowledgments

It is a real pleasure to have reached this moment after three years of doctoral study and lately the time spent writing my thesis. Studying for a doctorate has been a truly life-changing experience for me and it would not have been possible to do without the support and guidance that I received from numerous people. Here I take this opportunity to express my sincere gratitude to the supervisor, committees, colleagues, families, and friends.

First of all, I would like to express my special gratitude to my supervisor Professor Giancarlo Cravotto, for his great support, valuable guidance, and consistent encouragement during the past three years. I am also very grateful for his scientific advice, knowledge, insightful discussions, and suggestions. Many thanks for his concern and help during studying and living in Turin. And thank him, for providing me the opportunity to grow and work in his research group. It is truly an honour to be his Ph.D. student.

I also have heartfelt gratitude to Professor Zhilin Wu in our research group, he makes tremendous support and guidance for my Ph.D. research. Working with him in Italy has undoubtedly turned this tiring process into a real joy. His strong expertise, cautious optimism, and patient guidance have all enlightened and accelerated my research. Each time I got stuck on something, he came up with the solution and encouraged me a lot.

My sincere thanks also go to Professor Maela Manzoli, who helped me a lot with characterization materials, preparation of presentations, and revision of manuscripts. Without her support, it would not be possible to carry out some of the research. Thanks for her kind support, good suggestions, and precious time. Also, special thanks to her concern for me in our laboratory.

Besides my supervisor, I would like to thank the rest of my thesis committees: Prof. Sivakumar Manickam and Prof. Judy Lee for their insightful comments and suggestions, but also useful questions helping me to widen my research view.

Special mention is given to the China Scholarship Council, and the Department of Drug and Sciences and Doctoral School of the University of Turin, not only for

allowing me to undertake this research but also for allowing me to attend conferences.

I would like to thank Dr. Victoria Franzinetti for her help in my English study for three years. I also thank her for helping me to check and revise the thesis. I would like to thank her for her advice and help with my thesis and defense.

I thank all the members of Professor Cravotto's group: Dr. László Jicsinszky supported me in the experiment and data analysis. Stefano Mantegna and Dr. Giorgio Grillo supported me with experimental techniques in the laboratory. Additionally, thanks to Prof. Emanuela Calcio Gaudino, Prof. Silvia Tabasso, Dr. Luisa Boffa, Francesco Mariatti, Federico Verdini, Marco Belluati, Fabio Bucciol, Lorenzo Gallina, Giorgio Capaldi, Clelia Aimone and Roberto Solarino all kind help and accompany.

Last, but not least, I would like to express my appreciation to my family. Words cannot express how grateful to my mother and father for all the sacrifices, consistent love, and support. I also thank my sister, brother, and girlfriend for their great concern, support, and encouragement.

Acronyms and Abbreviations

Table A1. List of the acronyms of materials

Materials	Acronyms
Spherical SiO_2 nanoparticles	SSNs
Hollow mesoporous silica nanoparticles	HMSNs
Spherical SiO_2 nanoparticle@mesoporous silica	$SSN@mSiO_2$
Mesoporous silica nanoparticles	MSNs
VOR-loaded HMSNs	VOR-HMSNs
Nano-calcium carbonate	Nano-$CaCO_3$
$CaCO_3$@mesoporous silica	$CaCO_3@mSiO_2$

Table A2. List of the acronyms and abbreviations of compounds and solvents

Compounds/Solvents	Acronyms and Abbreviations
Ammonium hydroxide	NH_4OH
Tetraethyl orthosilicate	TEOS
Hexadecyl trimethyl ammonium bromide	CTAB
Voriconazole	VOR
Carbonic acid	Na_2CO_3
Hydrochloric acid	HCl
Phosphate buffer	PB
Calcium chloride	$CaCl_2$
Sodium hexametaphosphate	$(NaPO_3)_6$

IV

Table A3. **List of the acronyms and abbreviations of characterization methods**

Characterization methods	Acronyms and Abbreviations
Quasi Elastic Light Scattering	QELS
Field Emission Scanning Electron Microscope	FESEM
X-ray diffraction	XRD
Thermogravimetric analysis	TGA
Fourier–transform infrared spectroscopy	FT-IR
Electron paramagnetic resonance	EPR
Transmission electron microscopy	TEM
Brunauer-Emmett-Teller	BET
Barrett-Joyner-Halenda	BJH

Abstract

Inorganic nanomaterials refer to materials with a particle size of 1-100 nm. Inorganic nanomaterials are either metallic nanomaterials or non-metallic nanomaterials. However, inorganic non-metallic nanomaterials are the most important category of nanomaterials due to the variety of types and their wide application. Due to their nanometre size, inorganic nanomaterials have unique surface effects, small-size effects, quantum-size effects, macroscopic tunnelling effects, etc.

There are many methods for preparing inorganic nanoparticles. According to the nature of the reaction, the preparation method of inorganic nanomaterial can either use physical methods for instance evaporation-condensation, high-energy mechanical ball milling, sputtering method, etc. or using chemical methods for instance chemical precipitation, hydrothermal synthesis, microemulsion, and others. Sonochemical is quick synthetic method, which originates from the physical and chemical effects that are induced by ultrasound traveling in liquids. The chemical and physical processes induced by ultrasound offer the possibility for the formation of nanomaterials with various compositions and structures. The physical and chemical effects of ultrasound have therefore been exploited to produce nanostructured materials. Sonication of liquids generates highly reactive free radicals for primary sonochemistry, or induces the transformation of primary free radicals for secondary sonochemistry. Such free radicals are strong oxidizing or reducing agents that can act to initiate various chemical reactions in aqueous or non-aqueous solutions, including reduction, oxidation, or hydroxylation of solutes. Moreover, many physical effects (e.g., heating, shock waves, microjets) are induced by acoustic cavitation in liquids whose. Physical effects can affect the frequency and efficiency of chemical reactions in the material.

Recently, nanotechnology has been emerging rapidly as a useful tool for drug release and diagnosis, since inorganic nanoparticles generally possess versatile properties, that is, good specific surface area, magnetism, and easy functionalization with ligands, to enhance the controlled targeted drug release. Therefore, inorganic nanoparticles have been frequently applied in controlled drug release. Against these backgrounds, this doctoral thesis aims at the preparation of

spherical SiO_2 nanoparticles (SSNs) and nano-calcium carbonate (Nano-$CaCO_3$) nanoparticles using ultrasonic methods to reduce reaction time and particle size. The influence of ultrasonic cavitation bubbles on the number of nucleation was discussed. The surface of cavitation bubbles provided nucleation sites were proposed, which is useful for future study in the preparation of nanomaterials. Hollow mesoporous silica nanoparticles (HMSNs) were prepared by using SSNs and nano-$CaCO_3$ as hard templates. The drug loading and drug release properties of the prepared HMSNs were studied.

My thesis consists of 4 parts:

(1) SSNs have been inventively synthesized using the Stöber method with sonication with medium–high frequencies (80, 120, and 500 kHz), aiming to control SSN size and shorten reaction time. Compared to the conventional method ($\geqslant$6 h), such sonication allowed the Stöber reaction complete in 20–60 min with a low molar ratio of NH_4OH/tetraethyl orthosilicate (0.84). The hydrodynamic diameters of 63–117 nm of SSNs were obtained under sonication with 80, 120, and 500 kHz of ultrasonic frequencies. Moreover, the SSNs obtained were smaller at 120 kHz than at 80 kHz in a multi–frequencies ultrasonic reactor, and the SSN size decreased with increasing ultrasonic power at 20°C, designating the sonochemical unique character, namely, the SSN–size control is associated with the number of microbubbles originated by sonication (Fig. A1). With another 500 kHz ultrasonic bath, the optimal system temperature for producing smaller SSNs was proven to be 20°C. Furthermore, similarly, SSN size decreased with increasing ultrasonic power at 500 kHz. The smallest SSNs (63 nm, hydrodynamic diameter by Quasi Elastic Light Scattering (QELS), or 21 nm by field emission scanning electron microscope (FESEM) were obtained by sonication at 207 W for 20 min at 20°C and 500 kHz. Furthermore, the SSN size increased slightly with increasing sonication time and volume, favouring the scaleup of SSN preparation. The mechanisms of controlling the SSN size were further discussed in relation to the radical's role and effects of ammonia and ethanol concentration.
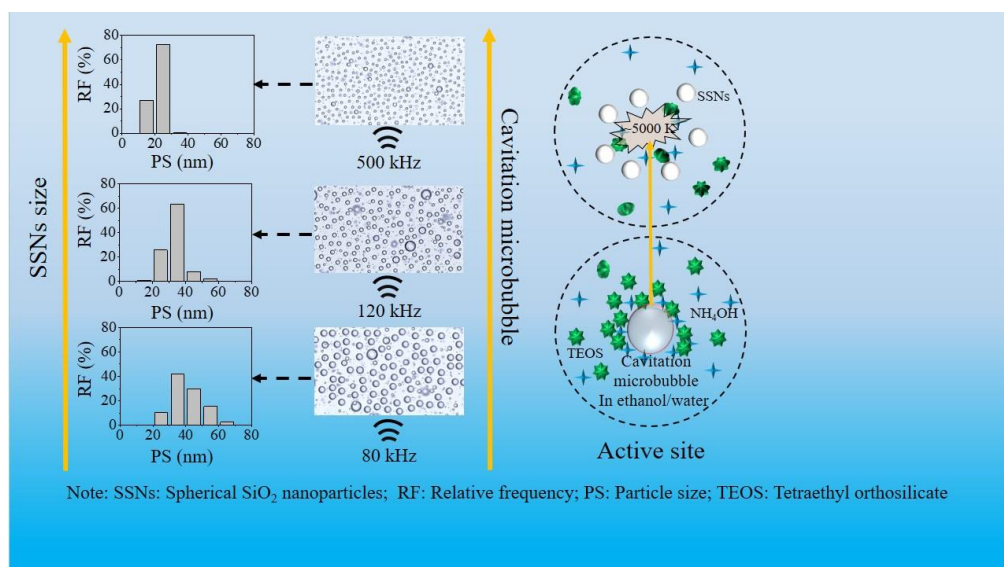
Fig. A1 Ultrasonic preparation of SSNs at 80 kHz, 120 kHz, and 500 kHz.

(2) Hollow mesoporous silica nanoparticles (HMSNs) were synthesized by double-template method with SSNs as the hard template and hexadecyl trimethyl ammonium bromide (CTAB) as the soft template. The mesoporous silica with core-shell structure was prepared by 500 kHz sonication. To reduce the reaction time, ultrasound was used to remove the SSNs core and a microwave was used to remove the soft template of CTAB to obtain HMSNs. The effects of ultrasonic frequency, ultrasonic power, ultrasonic time, ultrasonic volume, and bulk temperature on etching were investigated. The effect of ultrasonic frequency on the etching of silica nano-cores was not significant. At 40 kHz, the etching efficiency increased with the increasing of ultrasonic power. At 40 kHz, the SSN cores were completely etched by sonication for 30 min, while it took only 10 min at 19.5 kHz. Ultrasonic temperature, however, had a significant effect on the etching of SSN cores. The optimum etching temperature was 50°C. In addition, the effects of microwave treatment time and temperature on the CTAB removal were studied. The results show that CTAB can be completely removed at 80°C for 5 min. Finally, the drug loading and release characteristics of HMSNs were studied by using the antifungal drug voriconazole (VOR) as a model drug. The preparation of HMSNs, and the drug loading and release of HMSNs have been illustrated in Fig. A2. The loading efficiency (wt%) of VOR on the HMSNs was 9.63%, and the total VOR release amount of VOR-HMSNs material was 65.1% at 36 h. The Korsmeyer-Peppas and Higuchi kinetic model confirmed that the release mechanism of HMSNs nanoparticles followed Fickian diffusion at pH 7.4

and 37°C. At pH 5.8, the cumulative release amount of VOR from the VOR-HMSNs material was similar at pH 7.4. A Korsmeyer-Peppas kinetic model shows that the VOR molecules pass through the pore of the silica shell with Fickian diffusion mechanism at pH 5.8.
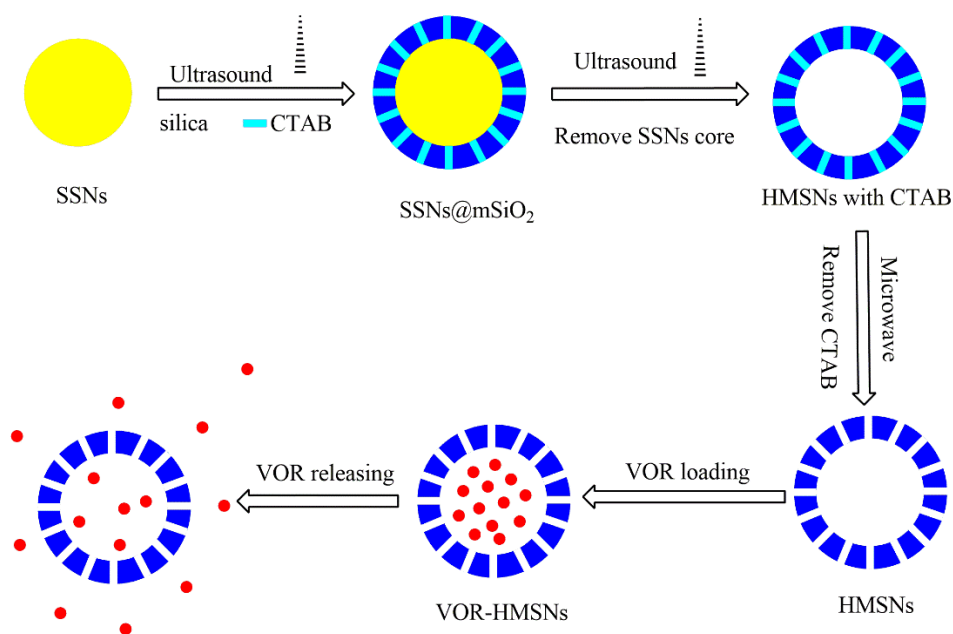
Fig. A2 **HMSNs obtained with sonication for VOR loading and release.**

(3) $CaCl_2$ and Na_2CO_3 solutions were used as reactants to prepare nano-$CaCO_3$ under sonication with low-frequency ultrasound (19.5 kHz). The effects of reactant concentration, sonication time, ultrasonic power, and reactant volume on the size of $CaCO_3$ particles were investigated. As shown in Fig. A3, the small nano-$CaCO_3$ particles were obtained with sonication compared to stirring. FESEM, X-ray diffraction (XRD), and Fourier-transform infrared (FT-IR) were used to characterize the morphology and crystallization of the prepared nano-$CaCO_3$ samples. FESEM showed that the flakes of nano-$CaCO_3$ were obtained under sonication, whilst the full cubes were with stirring. The prepared nano-$CaCO_3$ was proven to be calcite through XRD and FT-IR characterization. The sonochemical mechanism to prepare nano-$CaCO_3$ suggested that the nucleation rate of $CaCO_3$ particles was improved by cavitation bubbles and the crystal growth was inhibited by hydroxyl radicals. The surface of the cavitation bubbles provided active sites for $CaCO_3$ nucleation

resulting in an increasing nucleation rate. In addition, the generated hydroxyl radicals by sonication interacted with Ca^{2+} ions to inhibit the growth of crystals.
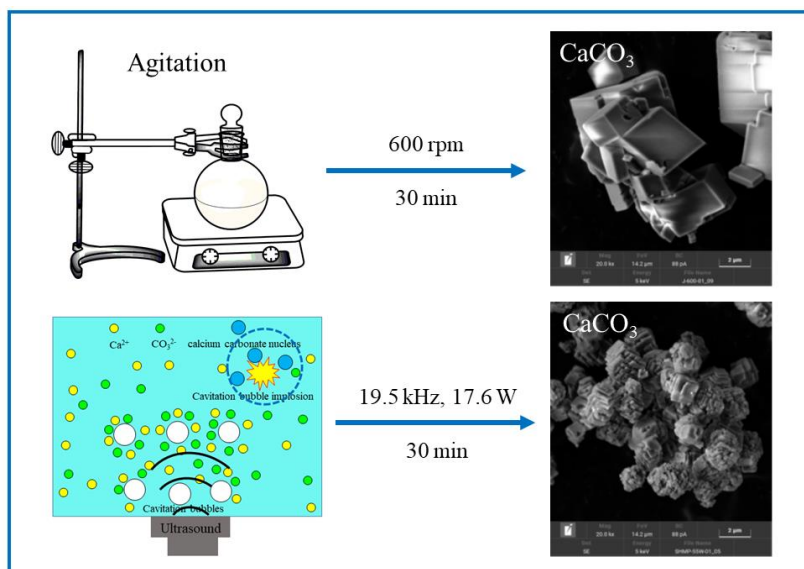
Fig. A3 The preparation of $CaCO_3$ by 19.5 kHz sonication and 600 rpm agitation.

(4) The nano-$CaCO_3$ as nano-templates were prepared with $CaCl_2$ and Na_2CO_3 solutions by 19.5 kHz sonication. HMSNs were synthesized by double-template method with nano-$CaCO_3$ as the hard template and CTAB as the soft template (as shown in Fig. A4). The transmission electron microscopy showed that the prepared HMSNs possess hollow structures, and the particle sizes of the obtained HMSNs nanoparticles were between 110-120 nm. The nitrogen adsorption isotherm showed that the HMSNs have a high surface area (401.57 m^2/g), pore volume (0.11 cm^3/g), and uniform pore size (2.22 nm) that facilitated the effective encapsulation of antifungal drug VOR within HMSNs. The loading efficiency (wt%) of VOR on the HMSNs was 7.96%, and the total VOR release amount of VOR-HMSNs material was 71.40% at 480 min. The Korsmeyer-Peppas and Higuchi kinetic models confirmed that the release mechanism of HMSNs nanoparticles followed Fickian diffusion at pH 7.4 and 37°C. Moreover, the cumulative VOR release at 42°C (86.05%) was higher than that at 37°C (71.40%). The cumulative release amount of VOR from the VOR-HMSNs material was 92.37% at pH 5.8. A Korsmeyer-Peppas kinetic model shows

that the VOR molecules pass through the pore of the silica shell with Fickian diffusion mechanism at pH 5.8.
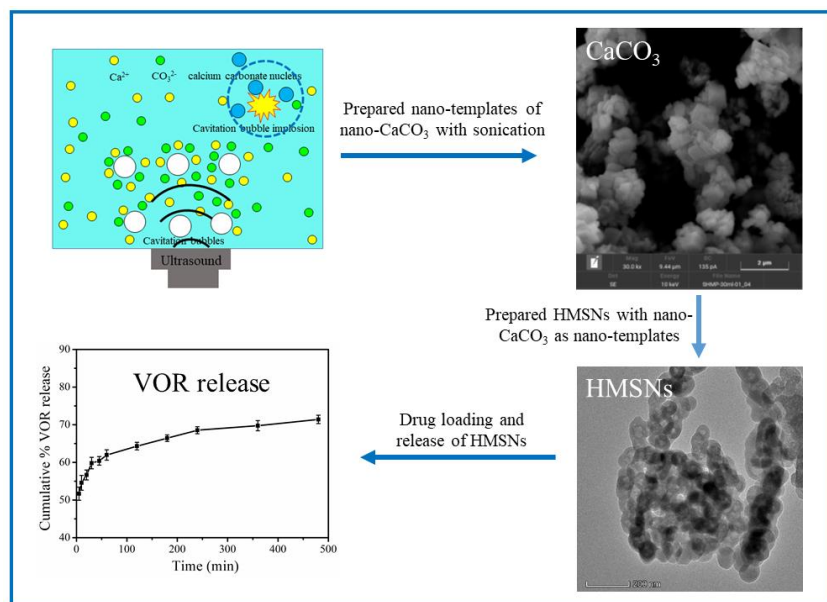
Fig. A4 HMSNs obtained with nano-CaCO$_3$ as the hard template for VOR loading and release.

Chapter 1: Theoretical Framework

1.1 Introduction

1.1.1 Inorganic nanomaterials

Nanomaterials are an important basis for the development of nanotechnology, and the most important object of nanotechnology research.

Researchers have been studying particles with a diameter of 1-100 nm which led to the establishment of colloidal chemistry since 1861.[1-3] However, it was not till the 1960s that nanoparticles were used as the object of the research.[4] Generally, in three-dimensional space, materials with at least one dimension in the nanoscale range are considered nanomaterials.[5]

The basic units of nanomaterials can be divided into three categories with dimensions:[5, 6]

① Zero-dimensional. The three-dimensional dimensions in space are all within the nanometer scale such as nanoscale particles, atomic clusters, etc.;

② One-dimensional. In three-dimensional space, two dimensions are within the nanometer scale, such as nanowires, nanorods, nanotubes, etc.;

③ Two-dimensional. In the three-dimensional space, one dimension is within the nanometer scale, such as ultra-thin film, multilayer film, superlattice, etc.

1.1.1.1 Types of inorganic nanomaterials

Inorganic nanomaterials are either metallic nanomaterials or non-metallic nanomaterials (Fig. 1.1). Non-metallic nanomaterials make up the main body of inorganic nanomaterials.
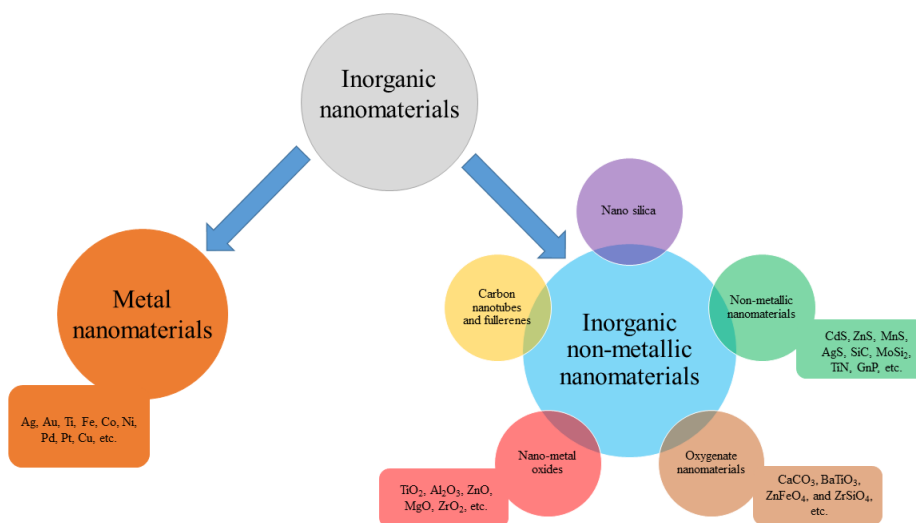
Fig. 1.1 The types of inorganic nanomaterials.

Metal nanomaterials

In the early 1960s, nano-metal particles were the earliest research objectives of nanotechnology.[4] Many nano-metal materials have been successfully developed since then, for example Ag, Au, Ti, Fe, Co, Ni, Pd, Pt, Cu, etc. Nano-metal particles have many crystal forms, such as polyhedrons, truncated polyhedrons, tetrahedrons, strips, needles, rings, spheres, triangles, rectangles, and hexagons.[7-10] Compared with macroscopic metals, the properties of nano-metal particles, such as optical, electrical, magnetic, thermal, and mechanical properties are different.[11-14]

Inorganic non-metallic nanomaterials

Inorganic non-metallic nanomaterials are the most important category of nanomaterials due to the variety of types and their wide application. At present, the main research and development of inorganic non-metallic nanomaterials are as follows:

(1) Nano-silica. Nano silica was first used as a rubber reinforcing agent. At present, nano-silica has been used in various coatings, adhesives, sealants, lubricants, catalyst carriers, cosmetics, medicines, pesticides, etc.[15-21]

(2) Nano-metal oxides. There are many varieties of nano-metal oxides, such as TiO_2, Al_2O_3, ZnO, MgO, ZrO_2, etc. The relatively stable nano-metal oxides can be obtained because the surface is modified more easily. Therefore, nano-metal oxides have been widely used in catalysts, ceramics, plastics, etc.[22-24]

(3) Other non-metallic nanomaterials, including sulfides (CdS, ZnS, MnS and AgS, etc.); carbides, silicides, nitrides, and phosphides (SiC, $MoSi_2$, TiN, and GnP, etc.).

(4) Oxygenate nanomaterials. Oxygenate nanomaterials are a class of nanomaterials with many special properties and wide applications, such as $CaCO_3$, $BaTiO_3$, $ZnFeO_4$, and $ZrSiO_4$. Among them, nano-calcium carbonate has been widely used in industries such as rubber, plastics, coatings, inks, and papermaking owing to low costs.[25-27]

(5) Carbon nanotubes and fullerenes. Carbon nanotubes are hollow "microtube" carbons with an outer diameter ranging from a few to tens of nanometers by coiling of the hexagonal grid-like graphite. Carbon nanotubes are one of the most important frontier research fields due to their unique structure and properties. Fullerenes are clusters composed of several carbon atoms, usually referring to spherical cage-like carbon clusters composed of C_{60}. The solutions of C_{60} and C_{70} are transparent with the intensity of light small. Contrarily, solutions of C_{60} and C_{70} become opaque with the light intensity exceeds a certain value. Therefore, fullerenes can be used as a photosensitive device.[28, 29]

1.1.1.2 *Properties of inorganic nanomaterials*

At the nanoscale, the properties of materials significantly change, since the wave nature of the electronwave and the interaction between atoms are affected by the scale.[30] Therefore, the properties of inorganic nanomaterials are different from traditional materials, such as melting point, magnetic properties, electrical properties, optical properties, mechanical properties, and chemical activity.[31] Due to their nanometer size, inorganic nanomaterials have unique surface effects,

small size effects, quantum size effects and macroscopic tunneling effects, etc. (Fig. 1.2).[32-34]
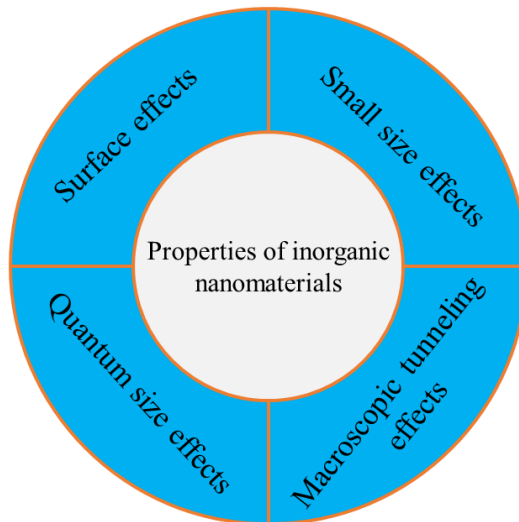
Fig. 1.2 The properties of inorganic nanomaterials.

These four basic properties of nanomaterials are summarized as follows:[35]

Surface effects

Reduction of particle size to nanoscale leads to a significant increase in the number, surface area, and surface energy of particles. Due to the vacancy effect of surface particles, there is a lack of adjacent particles around, resulting in insufficient coordination of surface particles. At the same time, the high surface energy of particles leads to the high activity of the surface atoms. Therefore, the particles can easily obtain stability by combining with external atoms due to their extremely unstable.

Small size effects

The change of macroscopic physical properties with the particle size becoming smaller is known as the "small size effect". Compared with larger particles, the melting point, magnetic properties, and electrical and optical properties of nanoparticles change due to their small size and large surface area.

Quantum size effects

In nanoscale materials, energy bands can be split into discrete energy levels (the quantization of energy levels). On the contrary, the energy bands of metal bulk materials can be regarded as continuous. The spacing of energy levels in nanomaterials increases as the particle size decreases. A series of abnormal properties can appear in nanoscale materials after the energy level spacing is higher than the average energy level spacing of thermal energy, photon energy, electrostatic energy, and magnetic energy. This effect is called the quantum size effect. The quantum size effect leads the magnetic, optical, electrical, acoustic, thermal, and superconductivity properties of nanoparticles to be significantly different from those of bulk materials.

Macroscopic tunneling effects

The ability of microscopic particles to cross the potential energy barrier is called the tunneling effect. In recent years, some macroscopic physical quantities have been discovered, such as the magnetization of tiny particles, the magnetic flux of quantum coherent devices, and charges can pass through the potential barrier of macroscopic systems to produce changes due to having tunnel effects. Thus, macroscopic tunneling effects, together with the quantum size effect, will be the basis of future microelectronic devices.

1.1.1.3   Preparation methods of inorganic nanomaterial

Nanoparticle materials have been studied for decades. Since the successful synthesis of bulk nanomaterials in the laboratory, the research and preparation of nanomaterials aroused general interest in materials science and condensed matter physics. There are many methods for preparing nanoparticles. According to the nature of the reaction, the preparation methods of inorganic nanomaterial can be either with physical methods (evaporation-condensation method, high-energy mechanical ball milling method, sputtering method, etc.) or using chemical methods (chemical precipitation method, hydrothermal synthesis method, microemulsion method, etc.) (Fig. 1.3).[36-38]
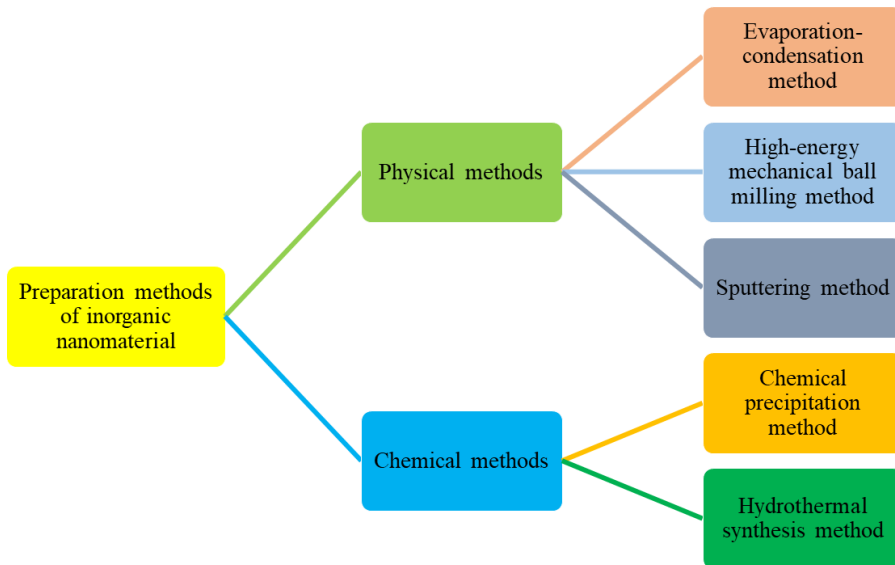
Fig. 1.3 The preparation methods of inorganic nanomaterial.

Physical methods

(1) Evaporation-condensation method[39, 40]

The method of evaporation-condensation is as follows: the container with the substance to be evaporated is evacuated to a high vacuum or filled with low-pressure inert gas. Then, the evaporation source is heated leading the substance (metal, alloy, or compound) to evaporate into Mist atoms and the Mist atoms are condensed on the condenser with the inert gas flow. The thus obtained nanoparticles are collected by scraping. The evaporation-condensation method is mainly used to prepare metal or metal oxide nanoparticles. The purity, particle size, and particle size distribution of the nanoparticles obtained can meet the ideal requirements. The crystal shape of prepared nanoparticles is difficult to control, and the production efficiency is low using the evaporation-condensation method. Therefore, the evaporation-condensation method was only used in the laboratory.

(2) High-energy mechanical ball milling method[41]

High-energy mechanical ball milling: mechanical energy is used to crush large grains into nanocrystals through ball milling. At the same time, intermetallic

compounds, metal carbides, and metal sulfides can be directly synthesized by the wet phase reaction between particles. Like the high-energy mechanical ball milling method, a high-speed jet impact method also uses mechanical energy to crush large particles. However, the wide distribution of particle size was obtained by these methods and needed to be further classified.

(3) Sputtering method[41]

Accelerated high-energy ions hit to vaporize causing emitted neutral (or ionized) atoms and atomic clusters to form nanoparticles. The sputtering method can be divided into ① Ion sputtering method: the nanoparticles are obtained by using Ar^+, Kr^+, and H^+ to bombard the block in a low-pressure inert atmosphere; ② Laser erosion method: gasification is caused by laser eroding the block to form nanoparticles; ③ Plasma sputtering method: plasma is used as the bombardment source to sputter the block to obtain nanoparticles. The sputtering method can vaporize almost anything, however, an amount of agglomerates is produced.

Chemical methods

(1) Chemical precipitation method[41]

The methods of chemical precipitation can be classed as i) co-precipitation method, ii) homogeneous precipitation method, iii) polyol precipitation method, iv) precipitation transformation method, and v) direct transformation method. With a precipitating agent added to a soluble salt solution containing one or more ions, insoluble hydroxides, hydrated oxides, or salts are formed by hydrolysis and precipitated from the solution. Nanoparticle materials are obtained by undergoing thermal hydrolysis or dehydration treatment after the original anions are removed from the solvent and the solution. Many nanometer oxide powders can be prepared by the chemical precipitation method due to the simple process. However, the obtained nanometer has low purity and large particle size.

(2) Hydrothermal synthesis method[41]

Insoluble substances are dissolved and recrystallized with water as the reaction medium under reaction conditions of high-temperature and high-pressure. Hydrothermal technology has two characteristics, one is a relatively high temperature, and the other one is a reaction in a closed container to avoid the

volatilization of components. Nanomaterial preparation under hydrothermal conditions includes hydrothermal crystallization, hydrothermal synthesis, hydrothermal decomposition, hydrothermal dehydration, hydrothermal oxidation hydrothermal reduction, etc. Compared with the general chemical method, the hydrothermal method can obtain dispersed and well-crystallized material without high-temperature burning treatment, and avoids the possible hard agglomeration of nanomaterial. Moreover, the crystal structure, crystal morphology, and grain purity of nanomaterial can be controlled by adjusting the experimental conditions in the hydrothermal process.

In summary, the physical method is a top-down method to turn large bulk materials into tiny particles.[37] The chemical preparation method is a bottom-up method to make smaller atoms, ions, and molecules form larger nanoscale crystals, clusters, or molecules through reactions.[37] The chemical method is currently widely used in laboratories and industries.

1.1.1.4   *Applications of inorganic nanomaterials*

Increasing attention has been recently paid to the preparation and application of nanoparticles. Nanoparticles possess unusual physicochemical and biological characteristics due to their nanometer size. Therefore, nanoparticles have been widely used in chemical, biological, electronic sensing, and medical fields.

Applications of inorganic nanomaterials in chemistry

As far as the chemical application of inorganic nanomaterials is concerned, catalysis is one of the most important applications. Inorganic nanomaterials are widely used as catalysts in chemical engineering processes, environmental protection and remediation, green chemistry, efficient conversion of biomass, and renewable energy.[42] Inorganic nanomaterial catalysts include multi-component active nanometal phases with highly porous nanomaterial supports, which can effectively enhance the structure or performance of active materials.[42] These types of nanocatalysts are considered to share the advantages of homogeneous and heterogeneous catalysts, namely high efficiency and selectivity, stability, and easy recovery/recycling.[43]

Applications of inorganic nanomaterials in biology

Nanomaterials become attractive support materials for constructing immobilized enzymes due to their large surface area, strong mechanical strength, high resistance to organic solvents, and high thermal stability.[44] Nanoparticles often exhibit unique properties. For example, the Brownian motion of nanoparticles, and the self-assembly behavior of discrete nanostructures provide opportunities for enzyme immobilization.[45] However, the greatest impact is the surface area and size of nanomaterials, since the ratio of surface and volume increases with particle size decreasing resulting in large enzyme loading and low mass transfer resistance.[45] Furthermore, many new nanomaterials have been used in enzyme immobilization with the advancement of nanoscience.[45]

Applications of inorganic nanomaterials in the medical field

Due to their unique properties, nanomaterials have been widely used in various fields, especially in the field of biomedicine. In nanomedicine, inorganic nanomaterials refer to nanomaterials with inorganic substances as the main body.[46] Compared with organic nanomaterials, inorganic nanomaterials have unique physical and chemical properties, such as optical, electrical, magnetic, ultrasonic, catalytic properties, etc.[46] In addition, inorganic nanomaterials have better chemical and mechanical stability than most organic nanomaterials.[47] Inorganic nanomaterials have considerable potential for biomedical applications, especially in cancer imaging and therapy, since inorganic nanomaterials possess diverse properties, including structure, composition, morphology, and physicochemical properties.[48-50] In the past few decades, inorganic nanomaterials have been widely used in the field of biomedicine, especially in the field of cancer therapy.[51-54]

1.1.2 Ultrasound

Ultrasound is a wave with a frequency above the range of normal human hearing, i.e. above 16 kHz (16,000 cycles per second).[55, 56] As early as 1927, researchers began to pay attention to the sonochemical effect, although, it became more widely used with the development of high-intensity ultrasound equipment in the 1980s.[57] In recent years, sonochemistry has developed rapidly in many fields

such as synthetic chemistry, material science, biology, the chemical industry, etc.[58-60] The application of ultrasound in material science is mainly to synthesize metals, oxides, carbides, and sulfides with nanostructures, especially catalysts, preparation of biomaterials, synthesis of polymers, and surface modification.[61-64]

Physical and chemical effects of ultrasonic cavitation

The wavelength range of ultrasonic waves (about $10\text{-}10^{-3}$ cm) is much greater than the molecular scale. Therefore, the chemical action of ultrasonic waves does not directly interact with substances, but mainly through the cavitation in liquids. Cavitation refers to a series of physical and chemical processes with formed, rapidly growing, and explosively collapse of bubbles in a liquid under the action of high-intensity ultrasound (Fig. 1.4).[62, 64]
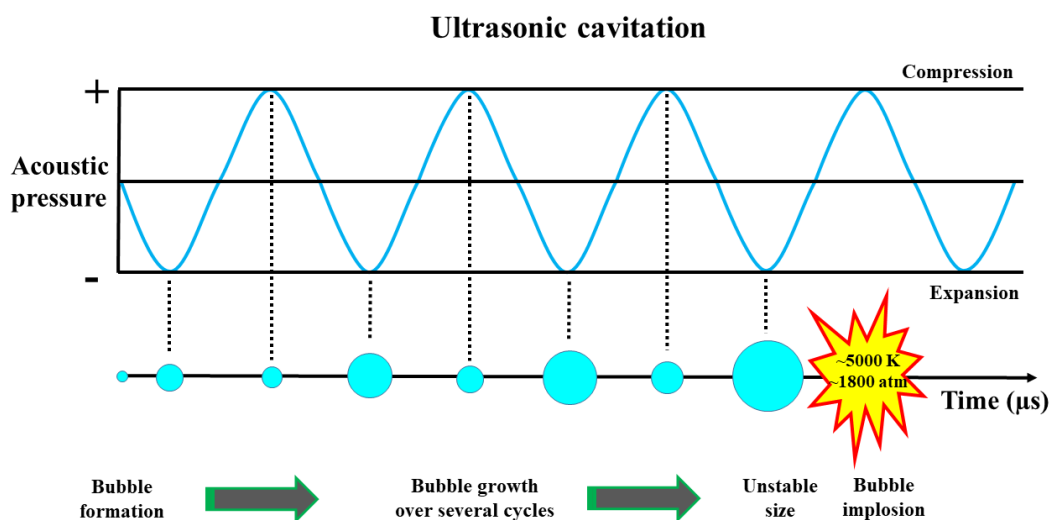
Fig. 1.4 The formation, growth, and implosion of cavitation bubbles in a liquid under sonication.

In the process of cavitation, the collapse of bubbles produces instantaneous high-pressure and high-intensity local heating. Energy density is 10^{11} orders of magnitude larger than that of the sound field, inducing high-energy chemical reactions. This is equivalent to providing an instantaneous high-temperature and high-pressure microreactor. The "hot spots" theory describing the cavitation

phenomenon suggests that the diameter of the cavitation bubble is estimated to be less than 170 μm. The lifetime of a cavitation bubble is less than 350 μs. The temperature and pressure of the hot spot are as high as about 5000 K and 1800 atm, respectively, and the rates of heating and cooling are higher than 10^{10} k/s.[65]

Sonochemical reactions are a series of chemical effects of high-intensity ultrasonic cavitation. Sonochemical reactions may occur in three areas in the collapsing bubble: inside the bubble, at the interface of the bubble, and in the bulk liquid phase. In addition, the sonochemical reaction can also occur in solid or solid-gas systems with the presence of ultrasonic radiation.[62]

Free radicals and excited molecules are generated inside the cavitation bubble. The free radical types and activated molecules are related to the nature of the solvent. For example, under the action of high-intensity ultrasound, hydrogen molecules and hydrogen peroxide are first produced in water. Superoxide (HO_2), atomic hydrogen, and hydrated electrons are also produced. Oxidation-reduction reactions can be caused by these intermediate products. Free radicals and excited substances (such as OH·, H·, halogen atoms X·, OH, C_2*, CN*, etc.) are generated under sonication in organic solvents. The types of free radicals produced by short carbon chain hydrocarbons are similar to their pyrolysis, such as H_2, CH_4, C_2H_2, etc.[61, 64]

A unique physical effect is produced with cavitation, such as the gradients of high-temperature gradient, pressure gradient, or possible field strength at the interface of the cavitation bubbles. A large shear and stress gradient is generated with liquid movement near the cavitation bubbles. Solvent molecules around the cavitation bubbles rapidly evaporate with cavitation and a strong shock wave is produced at the collapses of cavitation bubbles. The micro-jet impact appears as an asymmetric bubble collapse on the solid surface and the velocity of the shock wave is about 100 m/s. Microjets and shock waves can cause solid corrosion, breakage, and collisions of particles. Thus, well-behaved materials are obtained in the precursors by cavitation producing strong physical and chemical changes.[61, 64]

Effect of ultrasound on the number and size of cavitation bubbles

Ultrasound has a wide variety of applications, ranging from polymerization reactions and fabrication of nanoparticles to food science and biomedical

applications.[66-69] Most of these processes arise from acoustic cavitation. In general, there are three types of acoustic bubbles: dissolved bubbles, stable (degassing) bubbles, and transient bubbles.[70] Sonochemistry mainly consists of transient bubbles. In liquids, the interaction of the acoustic field with micron-size bubbles results in the phenomenon of acoustic cavitation.[71] In this field, bubbles can be grown in the appropriate size range by a combination of rectified diffusion growth and bubble coalescence pathways. In acoustic cycles, with bubbles reaching a critical size range, bubbles can experience rapid growth and then inertial collapse. Inside cavitation bubbles, the high temperatures and pressures are transiently generated with the near-adiabatic collapse of the bubbles. The overall efficiency of the sonochemical process is related to the number and size of cavitation bubbles. However, the number and size of bubbles depend on the frequency and power of ultrasound.[72]

(1) Effect of ultrasonic frequency

The number of cavitation bubbles increases with the increasing ultrasonic frequency. In contrast, the size of cavitation bubbles decreases with increasing ultrasonic frequency.[73] At higher frequencies, the time of bubble growth (during the rarefaction cycle of the ultrasound) and collapse (during the compression cycle of the ultrasound) is relatively short.[74] In addition, the variation amplitude of the bubble volume decreases as the increasing ultrasonic frequency. With the increasing ultrasonic frequency, the growth time of bubbles is shorter and the variation amplitude of the bubble volume becomes smaller, resulting in the size of bubbles decreasing with the increasing ultrasonic frequency.[74] The resulting tendency for the number of bubbles to increase with increasing ultrasonic frequency can be explained by the rate of bubble generation. As the increasing ultrasonic frequency, the maximum size of the bubble decreases, correspondingly, the lifetime of the bubble also decreases.[73] Cavitation bubbles can be broken into daughter bubbles during one acoustic cycle.[73] The expansion and collapse of the bubbles occur rapidly as the ultrasonic frequency increases due to the shorter acoustic period at higher frequencies. The number of acoustic cycles is more per second under higher frequencies, resulting in a higher rate of bubble generation. This is the reason for the increasing number of cavitation bubbles with ultrasonic frequency.

(2) Effect of ultrasonic power

The number and size of cavitation bubbles also depend on the ultrasonic power. The number and size of cavitation bubbles increase with the increasing ultrasonic power. When higher acoustic powers are applied, the bubbles are exposed to greater negative pressures during the rarefaction cycle of the ultrasound wave, resulting in a higher bubble size.[74] In addition, the transmission of ultrasonic energy into the reactor increases as the ultrasonic power increases.[75] Due to this energy, the pulsation and collapse of the bubbles occur more rapidly. According to the effect of ultrasonic frequency on the rate of bubble generation, the rapid bubble expansion and collapse lead to a higher bubble generation rate. Therefore, the number of cavitation bubbles increases with the increasing of acoustic power.

1.1.3 Preparation of inorganic nanoparticles with ultrasonic

The chemical and physical processes induced by ultrasound offer the possibility for the formation of nanomaterials with various compositions and structures. The physical and chemical effects of ultrasound have therefore been exploited to produce nanostructured materials. Sonication of liquids generates highly reactive free radicals for primary sonochemistry or induces the transformation of primary free radicals for secondary sonochemistry.[76] These free radicals can act to initiate various chemical reactions in aqueous or non-aqueous solutions, including reduction, oxidation, or hydroxylation of solutes as strong oxidizing or reducing agents. Moreover, many physical effects, e.g., heating, shock waves, microjets, are induced by acoustic cavitation in liquids and can affect the frequency and efficiency of chemical reactions in the material.[77, 78] In short, most of the applications of ultrasound are based on chemical and physical effects, such as the fragmentation of brittle materials, the emulsification of immiscible liquids, the agglomeration of malleable materials, and the exfoliation of layered materials into 2D layers and the fabrication of drug systems.[79-81]

Chemical effects of ultrasound for nanomaterials preparation

The chemical effect of ultrasound mainly comes from the hot spots created by the collapsing of bubbles. All chemical bonds are dissociated because they produce

sufficiently high local temperatures with effective compression heating.[82] Inside the collapsing bubble, the reaction occurs between volatiles and gases present. This reaction is called a primary sonochemical reaction. Secondary sonochemical reactions occur as initially formed species migrate into the surrounding liquid. In the liquid, many radical species can generate within an ultrasonic hot spot. Then these free radical species can undergo a variety of secondary reactions with solutes in the surrounding liquid.[83]

Nanomaterials can be synthesized with sonochemistry by using volatile or nonvolatile precursors. Under sonication, during the collapsing of bubbles, volatile precursors (e.g., a volatile organometallic compound) generate free metal atoms due to the high temperature causing bond dissociation.[84] In the solution, if appropriate templates or stabilizers are present, these atoms can be injected into the liquid phase and nucleate to form nanoparticles or other nanostructured materials. Nonvolatile precursors may still undergo sonochemical reactions, even outside of the collapsing bubbles by undergoing reactions with radicals or other high-energy species produced from the sonolysis of vapor molecules inside the collapsing bubbles that then diffuse into the liquid phase to initiate a series of reactions (e.g., reduction of metal cations).[84]

(1) Nanomaterials prepared from volatile precursors

Volatile organometallic compounds such as $Fe(CO)_5$ or $Cr(CO)_6$ are irradiated with ultrasonic in nonvolatile solvents (e.g., silicone oil or long-chain hydrocarbons) resulting in the dissociation of the metal-carbonyl bonds and release of individual elemental metal atoms.[85] These atoms will be thermally excited to the point that they emit visible light analogous to emissions from flame excitation; their atomic emission lines have been used to characterize the bubble conditions.[86] Nonvolatile solvents are necessary because additional vapor, especially from polyatomics, absorbs the available energy in the collapsing bubble (via rotational and vibrational molecular modes, ionization, and competing bond dissociation) and the conditions achieved are much less extreme.[84]

(2) Nanomaterials prepared from nonvolatile precursors

Nanomaterials can also be prepared with sonochemistry by using nonvolatile precursors in a volatile solvent (usually water or alcohol). Compared with traditional

reduction techniques, the solvent vapor produces strong reductants with sonication. Therefore, these have some advantages. For example, no additional reducing agents are required, the reduction rate is generally very fast, and very small nanoclusters can be made in this way when suitable stabilizers are present.[84] The highly reactive H· and OH· radicals are generated by using ultrasonic irradiation of water to be responsible for redox chemistry.[84] Secondary radicals (R·) are produced with highly reactive H· and OH· radicals further reacting with organic additives in solution, e.g., 2-propanol or ethanol, to significantly increase the reduction rate.[84]

Physical effects of ultrasound for nanomaterials synthesis

In addition, the physical effects of ultrasound such as heating, microjets, shock waves, shear forces, interparticle collisions, rapid mixing, and turbulence, are also important in the formation of nanomaterials.[84]

Shock waves and microjets are the most important physical phenomena for the preparation or modification of nanomaterials. Shock waves are produced with the cavitation collapse of the bubbles and propagate into the liquid medium. Several different physical effects and chemical consequences are caused by the shock waves, including enhanced mass transport due to strong turbulent mixing and acoustic streaming. In addition, shock waves can accelerate solid particles suspended in the liquid. The collisions of particle-to-particle can reach speeds of hundreds of meters per second to cause changes in particle size distribution, particle morphology, and surface composition.[87, 88] Microjets are produced with the bubble collapses near an expanding surface such as a surface several times larger than the bubble radius.[84] The material is ejected into the solution as the microjets hit the surface of the material. Microstreaming makes ultrasonic irradiation an effective means to mix liquids, erode solid surfaces, and facilitate interparticle collisions in suspensions of solid particles in liquids.[84, 87-90]

Crystal formation and growth mechanism of inorganic nanomaterials in sonochemical syntheses

A series of unique chemical and physical effects are generated with cavitation in ultrasonic irradiation to increase the reaction rate, product yield, mass transfer, and reactant diffusion. These are well reflected in the ultrasonic preparation of

inorganic nanomaterials. It is well known that nucleation and crystallization are crucial in the preparation of inorganic nanomaterials. However, ultrasound can significantly improve crystal nucleation and growth. Ultrasonic crystallization is crystallization under sonication and has significant potential for improving the crystallization process. As a branch of sonochemistry, ultrasonic crystallization has been gradually developed. Compared with traditional crystallization methods, ultrasonic crystallization is a novel and effective method to improve the crystallization process. In the process of supercooled and supersaturated crystallization, ultrasonic crystallization can accelerate the nucleation speed of crystals, and better control the formation and growth of crystals.[91]

Ultrasonic crystallization mainly focuses on the nucleation, growth, fragmentation, and agglomeration of crystals. Nucleation consists of two different processes, primary and secondary nucleation: primary nucleation is the creation of crystals in a solution without existing crystals, and secondary nucleation is the formation of crystals in a solution with pre-existing crystals.[92, 93] Primary nucleation is a key stage of crystallization. There are many mechanisms for nucleation and crystallization induced by ultrasonic irradiation. However, all proposed mechanisms agree that the effect of sonication on crystallization is not due to the propagation of sound waves, but rather due to the phenomenon of cavitation.[94-98] Compression and rarefaction of the medium are generated during the propagation of ultrasonic waves. Gas bubbles are formed in the rarefaction phase of the wave collapse under the action of the next compression phase leading to the generation of intense high pressure and temperature. Evaporation occurs on the surface of the cavity during the expansion of a cavitation bubble. One of the mechanisms suggests that local supersaturation of the solute as the evaporation of the solvent leads to nucleation.[99] Another mechanism has proposed that the higher local supersaturation appears at the cavity surface with cooling of the cavity surface during expansion and is sufficient to cause nucleation.[94]

Some mechanisms are related to pressure shock waves. Solute molecules are thrown with high force by shock waves generated during cavity collapse.[100] The barrier of surface and volume-free energy necessary for nucleation is overcome by these solute molecules colliding with each other.[100] Another hypothesis related to the shock wave effect proposes that nucleation is caused by the separation of

solute and solvent near the bubble wall since the high pressure occurs in the final stages of bubble collapse.[101]

1.1.4 Inorganic nanomaterials for drug release

Recently, nanotechnology has been emerging as a useful tool for drug release and diagnosis, since inorganic nanoparticles and nanocomposites generally possess versatile properties, that is, good specific surface area, magnetism, and easy functionalization with ligands, to enhance the controlled targeted drug release. Therefore, inorganic nanoparticles, such as gold, semiconductor nanocrystals, superparamagnetic nanoparticles, zinc oxide nanoparticles, silicon nanoparticles, and their nanocomposites have been frequently applied in controlled drug release. The drug release strategy is usually intended to be stimuli-responsive, which includes internal and external stimuli (Fig. 1.5).[102-107]

Compared to normal tissues, lesioned cells may modify the surrounding environment, such as pH value and enzyme content. Various drug-release systems have been developed to respond to internal stimuli following the above-mentioned physiological basis. The internal drug release strategy includes pH-, enzyme-, and redox-responsiveness.[108-110] The pH-responsive effect has been widely studied.[111-115] The pH values might decrease around lesion cells and the acidified environment usually causes the protonation of drugs and weakens electrostatic interactions and hydrogen-bond interactions between the nanocarrier and the drug, etc. After cell internalization, a lower pH can initiate the conjugation and release of the drug on the nanocarriers.[116] By contrast, the drug-conjugated nanocarrier is stable at pH 7.4. In addition, the core/shell nanocomposites with pH-sensitive polymer were also used to control the drug release.[117]

External stimuli principally include light, heat, ultrasound, magnetic fields, etc.[118-120] Relevant aspects of the temperature-responsive effect have been extensively reported.[121-124] Temperature dependent drug release is attributed to gel swelling and shrinking.[125] In general, temperature-sensitive polymers can be used to encapsulate inorganic nanoparticles, in which the phase transition occurs at ca. 306 K. The gel swells when hydrogel incorporates water below a lower

critical solution temperature. If the temperature exceeds the lower critical solution temperature, the gel shrinks, collapses, and releases drugs.[57, 126, 127]
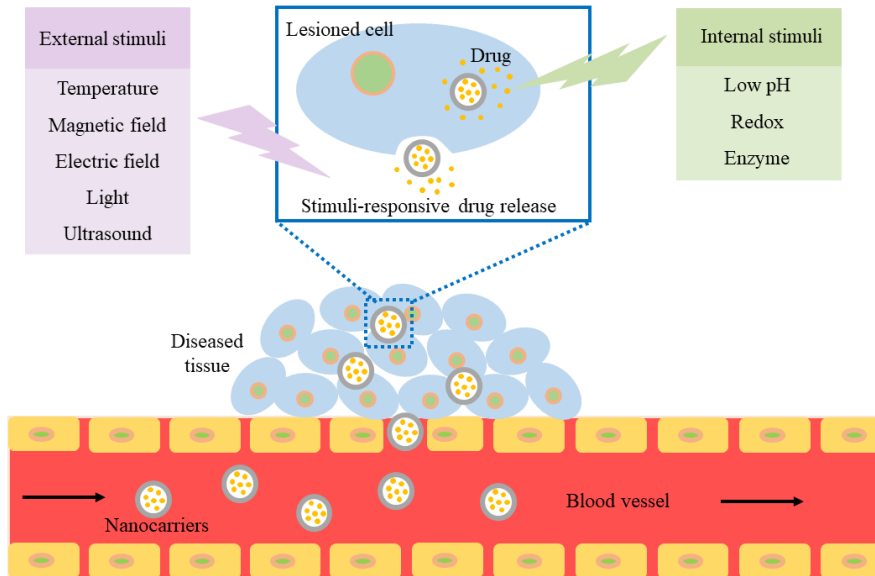
Fig. 1.5 Stimuli-responsive schematic of drug release strategy.

References

[1] S.K. Ghosh, T. Pal, Interparticle coupling effect on the surface plasmon resonance of gold nanoparticles: from theory to applications, Chemical Reviews, 107 (2007) 4797-4862.

[2] G.A. Somorjai, Y. Li, Introduction to surface chemistry and catalysis, John Wiley & Sons, 2010.

[3] R.J. Varghese, S. Parani, S. Thomas, O.S. Oluwafemi, J. Wu, Introduction to nanomaterials: synthesis and applications, in: Nanomaterials for Solar Cell Applications, Elsevier, 2019, pp. 75-95.

[4] S. Horikoshi, N. Serpone, Microwaves in nanoparticle synthesis: fundamentals and applications, John Wiley & Sons, 2013.

[5] C.M. Lieber, One-dimensional nanostructures: chemistry, physics & applications, Solid State Communications, 107 (1998) 607-616.

[6] S. Fu, Z. Sun, P. Huang, Y. Li, N. Hu, Some basic aspects of polymer nanocomposites: A critical review, Nano Materials Science, 1 (2019) 2-30.

[7] J. Hu, Y. Liu, Pd nanoparticle aging and its implications in the Suzuki cross-coupling reaction, Langmuir, 21 (2005) 2121-2123.

[8] K. An, G.A. Somorjai, Size and shape control of metal nanoparticles for reaction selectivity in catalysis, ChemCatChem, 4 (2012) 1512-1524.

[9] T.S. Sreeprasad, T. Pradeep, Noble metal nanoparticles, Springer Handbook of Nanomaterials, (2013) 303-388.

[10] K.E. Hermann, Polyhedral metal nanoparticles with cubic lattice: theory of structural properties, arXiv preprint arXiv:2201.07038, (2022).

[11] F.E. Kruis, H. Fissan, A. Peled, Synthesis of nanoparticles in the gas phase for electronic, optical and magnetic applications-a review, Journal of Aerosol Science, 29 (1998) 511-535.

[12] M.A. Meyers, A. Mishra, D.J. Benson, Mechanical properties of nanocrystalline materials, Progress in Materials Science, 51 (2006) 427-556.

[13] A. González, C. Noguez, Influence of morphology on the optical properties of metal nanoparticles, Journal of Computational and Theoretical Nanoscience, 4 (2007) 231-238.

[14] P.G. Jamkhande, N.W. Ghule, A.H. Bamer, M.G. Kalaskar, Metal nanoparticles synthesis: An overview on methods of preparation, advantages and

disadvantages, and applications, Journal of Drug Delivery Science and Technology, 53 (2019) 101174.

[15] E. Amerio, P. Fabbri, G. Malucelli, M. Messori, M. Sangermano, R. Taurino, Scratch resistance of nano-silica reinforced acrylic coatings, Progress in Organic Coatings, 62 (2008) 129-133.

[16] M.D. CD, S.B. PM, J. Rani, J. Daisy, K. Prabith, E. Ayswarya, Synthesis, characterisation and application of rice husk nanosilica in natural rubber, International Journal of Science, Environment and Technology, 2 (2013) 1027-1035.

[17] H. Zhou, H.-Y. Liu, H. Zhou, Y. Zhang, X. Gao, Y.-W. Mai, On adhesive properties of nano-silica/epoxy bonded single-lap joints, Materials & Design, 95 (2016) 212-218.

[18] P. Guo, L. Chen, J. Wang, Z. Geng, Z. Lu, G. Zhang, Enhanced tribological performance of aminated nano-silica modified graphene oxide as water-based lubricant additive, Applied Nano Materials, 1 (2018) 6444-6453.

[19] Z. Lu, L. Xu, Y. He, J. Zhou, One-step facile route to fabricate functionalized nano-silica and silicone sealant based transparent superhydrophobic coating, Thin Solid Films, 692 (2019) 137560.

[20] C. Chircov, A. Spoială, C. Păun, L. Crăciun, D. Ficai, A. Ficai, E. Andronescu, Ș.C. Turculeţ, Mesoporous silica platforms with potential applications in release and adsorption of active agents, Molecules, 25 (2020) 3814.

[21] S. Peito, D. Peixoto, I. Ferreira-Faria, A.M. Martins, H.M. Ribeiro, F. Veiga, J. Marto, A.C. Santos, Nano-and microparticle-stabilized Pickering emulsions designed for topical therapeutics and cosmetic applications, International Journal of Pharmaceutics, (2022) 121455.

[22] M.R.M. Farahani, F. Banikarim, Effect of nano-zinc oxide on decay resistance of wood-plastic composites, BioResources, 8 (2013) 5715-5720.

[23] A. Gnanaprakasam, V. Sivakumar, M. Thirumarimurugan, Influencing parameters in the photocatalytic degradation of organic effluent via nanometal oxide catalyst: a review, Indian Journal of Materials Science, 2015 (2015) 1-16.

[24] M. Elsafi, M.F. Dib, H.E. Mustafa, M. Sayyed, M.U. Khandaker, A. Alsubaie, A.S. Almalki, M.I. Abbas, A.M. El-Khatib, Enhancement of ceramics based red-clay by bulk and nano metal oxides for photon shielding features, Materials, 14 (2021) 7878.

[25] O. Söhnel, J. Mullin, Precipitation of calcium carbonate, Journal of Crystal Growth, 60 (1982) 239-250.

[26] F.J. Yu, Z.H. Wang, Study on the synthesis of high quality nanometer calcium carbonate using ultrasonic technology, in: Advanced Materials Research, Trans Tech Publ, 2010, pp. 235-240.

[27] M.E. Hoque, M. Shehryar, K.N. Islam, Processing and characterization of cockle shell calcium carbonate ($CaCO_3$) bioceramic for potential application in bone tissue engineering, Material Science & Engineering, 2 (2013) 132.

[28] R.G. Shrestha, L.K. Shrestha, A.H. Khan, G.S. Kumar, S. Acharya, K. Ariga, Demonstration of ultrarapid interfacial formation of 1D fullerene nanorods with photovoltaic properties, Applied Materials & Interfaces, 6 (2014) 15597-15603.

[29] F. Huang, Y. Li, H. Xia, J. Zhang, K. Xu, Y. Peng, G. Liu, Towards high performance broad spectral response fullerene based photosensitive organic field-effect transistors with tricomponent bulk heterojunctions, Carbon, 118 (2017) 666-674.

[30] T. Hanemann, D.V. Szabó, Polymer-nanoparticle composites: from synthesis to modern applications, Materials, 3 (2010) 3468-3517.

[31] S. Kango, S. Kalia, A. Celli, J. Njuguna, Y. Habibi, R. Kumar, Surface modification of inorganic nanoparticles for development of organic-inorganic nanocomposites-A review, Progress in Polymer Science, 38 (2013) 1232-1261.

[32] C. Fang, X. Yu, R. Yu, P. Liu, X. Qiao, Preparation and properties of isocyanate and nano particles composite modified asphalt, Construction and Building Materials, 119 (2016) 113-118.

[33] X. Chen, L. Cheng, H. Li, A. Barhoum, Y. Zhang, X. He, W. Yang, M.M. Bubakir, H. Chen, Magnetic nanofibers: unique properties, fabrication techniques, and emerging applications, ChemistrySelect, 3 (2018) 9127-9143.

[34] Q. Wu, W.S. Miao, H.J. Gao, D. Hui, Mechanical properties of nanomaterials: A review, Nanotechnology Reviews, 9 (2020) 259-273.

[35] G. Yu, Y. Cheng, Z. Duan, Research progress of polymers/inorganic nanocomposite electrical insulating materials, Molecules, 27 (2022) 7867.

[36] S. Iravani, H. Korbekandi, S.V. Mirmohammadi, B. Zolfaghari, Synthesis of silver nanoparticles: chemical, physical and biological methods, Research in Pharmaceutical Sciences, 9 (2014) 385.

[37] P. Pandey, M. Dahiya, A brief review on inorganic nanoparticles, Journal of Critical Reviews, 3 (2016) 18-26.

[38] Y. Xie, D. Kocaefe, C. Chen, Y. Kocaefe, Review of research on template methods in preparation of nanomaterials, Journal of Nanomaterials, 2016 (2016).

[39] A. Samokhin, N. Alexeev, A. Vodopyanov, D. Mansfeld, Y.V. Tsvetkov, Metal oxide nanopowder production by evaporation–condensation using a focused microwave radiation at a frequency of 24 GHz, Journal of Nanotechnology in Engineering and Medicine, 6 (2015) 011008.

[40] A. Vodop'yanov, D. Mansfeld, A. Samokhin, N. Alekseev, Y.V. Tsvetkov, Production of nanopowders by the evaporation–condensation method using a focused microwave radiation, Radiophysics and Quantum Electronics, 59 (2017) 698-705.

[41] A.V. Rane, K. Kanny, V. Abitha, S. Thomas, Methods for synthesis of nanoparticles and fabrication of nanocomposites, in: Synthesis of Inorganic Nanomaterials, Elsevier, 2018, pp. 121-139.

[42] U. Ashik, A. Viswan, S. Kudo, J.-i. Hayashi, Nanomaterials as catalysts, in: Applications of Nanomaterials, Elsevier, 2018, pp. 45-82.

[43] K. Philippot, P. Serp, Concepts in nanocatalysis, Nanomaterials in Catalysis, (2013) 1-54.

[44] S.-Y. Lee, J.-H. Lee, J.-H. Chang, J.-H. Lee, Inorganic nanomaterial-based biocatalysts, BMB Reports, 44 (2011) 77-86.

[45] J.H. Lee, S.Y. Lee, Z.K. Xu, J.H. Chang, Nanomaterial‐based biocatalyst, Nanocatalysis Synthesis and Applications, (2013) 615-641.

[46] X. Wang, X. Zhong, J. Li, Z. Liu, L. Cheng, Inorganic nanomaterials with rapid clearance for biomedical applications, Chemical Society Reviews, 50 (2021) 8669-8742.

[47] K. Zarschler, L. Rocks, N. Licciardello, L. Boselli, E. Polo, K.P. Garcia, L. De Cola, H. Stephan, K.A. Dawson, Ultrasmall inorganic nanoparticles: State-of-the-art and perspectives for biomedical applications, Nanomedicine: Nanotechnology, Biology and Medicine, 12 (2016) 1663-1701.

[48] X.J. Loh, T.-C. Lee, Q. Dou, G.R. Deen, Utilising inorganic nanocarriers for gene delivery, Biomaterials Science, 4 (2016) 70-86.

[49] K.S. Soni, S.S. Desale, T.K. Bronich, Nanogels: An overview of properties, biomedical applications and obstacles to clinical translation, Journal of Controlled Release, 240 (2016) 109-126.

[50] W. Tao, N. Kong, X. Ji, Y. Zhang, A. Sharma, J. Ouyang, B. Qi, J. Wang, N. Xie, C. Kang, Emerging two-dimensional monoelemental materials (Xenes) for biomedical applications, Chemical Society Reviews, 48 (2019) 2891-2912.

[51] G. Lin, P. Mi, C. Chu, J. Zhang, G. Liu, Inorganic nanocarriers overcoming multidrug resistance for cancer theranostics, Advanced Science, 3 (2016) 1600134.

[52] S. Veeranarayanan, T. Maekawa, External stimulus responsive inorganic nanomaterials for cancer theranostics, Advanced Drug Delivery Reviews, 138 (2019) 18-40.

[53] L. Cheng, X. Wang, F. Gong, T. Liu, Z. Liu, 2D nanomaterials for cancer theranostic applications, Advanced Materials, 32 (2020) 1902333.

[54] W. Paul, C.P. Sharma, Inorganic nanoparticles for targeted drug delivery, Biointegration of Medical Implant Materials, (2020) 333-373.

[55] L.H. Thompson, L. Doraiswamy, Sonochemistry: science and engineering, Industrial & Engineering Chemistry Research, 38 (1999) 1215-1249.

[56] Y.L. Pang, A.Z. Abdullah, S. Bhatia, Review on sonochemical methods in the presence of catalysts and chemical additives for treatment of organic pollutants in wastewater, Desalination, 277 (2011) 1-14.

[57] W.T. Richards, A.L. Loomis, The chemical effects of high frequency sound waves I. A preliminary survey, Journal of the American Chemical Society, 49 (1927) 3086-3100.

[58] M.H. Islam, B.G. Pollet, Acoustic cavitation and sonochemistry in industry: State of the art, Energy Aspects of Acoustic Cavitation and Sonochemistry, (2022) 265-279.

[59] K. Qi, C. Zhuang, M. Zhang, P. Gholami, A. Khataee, Sonochemical synthesis of photocatalysts and their applications, Journal of Materials Science & Technology, 123 (2022) 243-256.

[60] M. Saleem, M. Naz, S. Shukrullah, M. Shujah, M. Akhtar, S. Ullah, S. Ali, One-pot sonochemical preparation of carbon dots, influence of process parameters and potential applications: A review, Carbon Letters, 32 (2022) 39-55.

[61] S. Kenneth, The chemistry of ultrasound, Encyclopedia Britannica, (1994) 138-155.

[62] D. Peters, Ultrasound in materials chemistry, Journal of Materials Chemistry, 6 (1996) 1605-1618.

[63] P.W. Cains, P.D. Martin, C.J. Price, The use of ultrasound in industrial chemical synthesis and crystallization. 1. Applications to synthetic chemistry, Organic Process Research & Development, 2 (1998) 34-48.

[64] J.L. Luche, Synthetic organic sonochemistry, Synthetic Organic Sonochemistry, 1998.

[65] K.S. Suslick, S.-B. Choe, A.A. Cichowlas, M.W. Grinstaff, Sonochemical synthesis of amorphous iron, Nature, 353 (1991) 414-416.

[66] T.J. Mason, L. Paniwnyk, J. Lorimer, The uses of ultrasound in food technology, Ultrasonics Sonochemistry, 3 (1996) S253-S260.

[67] T.J. Mason, J.P. Lorimer, Applied sonochemistry: the uses of power ultrasound in chemistry and processing, Wiley-Vch Weinheim, 2002.

[68] A. Gedanken, Using sonochemistry for the fabrication of nanomaterials, Ultrasonics Sonochemistry, 11 (2004) 47-55.

[69] T. Yu, Z. Wang, T.J. Mason, A review of research into the uses of low level ultrasound in cancer therapy, Ultrasonics Sonochemistry, 11 (2004) 95-103.

[70] A. Dehane, S. Merouani, O. Hamdaoui, Effect of carbon tetrachloride (CCl_4) sonochemistry on the size of active bubbles for the production of reactive oxygen and chlorine species in acoustic cavitation field, Chemical Engineering Journal, 426 (2021) 130251.

[71] M. Ashokkumar, F. Grieser, Single bubble sonoluminescence–a chemist's overview, ChemPhysChem, 5 (2004) 439-448.

[72] A. Brotchie, F. Grieser, M. Ashokkumar, Effect of power and frequency on bubble-size distributions in acoustic cavitation, Physical Review Letters, 102 (2009) 084302.

[73] S. Merouani, H. Ferkous, O. Hamdaoui, Y. Rezgui, M. Guemini, A method for predicting the number of active bubbles in sonochemical reactors, Ultrasonics Sonochemistry, 22 (2015) 51-58.

[74] P. Kanthale, M. Ashokkumar, F. Grieser, Sonoluminescence, sonochemistry (H_2O_2 yield) and bubble dynamics: frequency and power effects, Ultrasonics Sonochemistry, 15 (2008) 143-150.

[75] S. Merouani, O. Hamdaoui, F. Saoudi, M. Chiha, Influence of experimental parameters on sonochemistry dosimetries: KI oxidation, Fricke reaction and H_2O_2 production, Journal of Hazardous Materials, 178 (2010) 1007-1014.

[76] R. Ji, R. Pflieger, M. Virot, S.I. Nikitenko, Multibubble sonochemistry and sonoluminescence at 100 kHz: the missing link between low-and high-frequency ultrasound, The Journal of Physical Chemistry B, 122 (2018) 6989-6994.

[77] K. Yamamoto, P.M. King, X. Wu, T.J. Mason, E.M. Joyce, Effect of ultrasonic frequency and power on the disruption of algal cells, Ultrasonics Sonochemistry, 24 (2015) 165-171.

[78] N.S.M. Yusof, M. Ashokkumar, Sonochemical synthesis of gold nanoparticles by using high intensity focused ultrasound, ChemPhysChem, 16 (2015) 775-781.

[79] J.H. Bang, K.S. Suslick, Applications of ultrasound to the synthesis of nanostructured materials, Advanced Materials, 22 (2010) 1039-1059.

[80] D.G. Shchukin, D. Radziuk, H. Möhwald, Ultrasonic fabrication of metallic nanomaterials and nanoalloys, Annual Review of Materials Research, 40 (2010) 345-362.

[81] J.J. Hinman, K.S. Suslick, Nanostructured materials synthesis using ultrasound, Sonochemistry: From Basic Principles to Innovative Applications, (2017) 59-94.

[82] T. Ouerhani, R. Pflieger, W. Ben Messaoud, S.I. Nikitenko, Spectroscopy of sonoluminescence and sonochemistry in water saturated with N_2–Ar mixtures, The Journal of Physical Chemistry B, 119 (2015) 15885-15891.

[83] P. Riesz, D. Berdahl, C. Christman, Free radical generation by ultrasound in aqueous and nonaqueous solutions, Environmental Health Perspectives, 64 (1985) 233-252.

[84] H. Xu, B.W. Zeiger, K.S. Suslick, Sonochemical synthesis of nanomaterials, Chemical Society Reviews, 42 (2013) 2555-2567.

[85] K.S. Suslick, E.B. Flint, M.W. Grinstaff, K.A. Kemper, Sonoluminescence from metal carbonyls, The Journal of Physical Chemistry, 97 (1993) 3098-3099.

[86] W.B. McNamara III, Y.T. Didenko, K.S. Suslick, Sonoluminescence temperatures during multi-bubble cavitation, Nature, 401 (1999) 772-775.

[87] S.J. Doktycz, K.S. Suslick, Interparticle collisions driven by ultrasound, Science, 247 (1990) 1067-1069.

[88] T. Prozorov, R. Prozorov, K.S. Suslick, High velocity interparticle collisions driven by ultrasound, Journal of the American Chemical Society, 126 (2004) 13890-13891.

[89] K.S. Suslick, Sonochemistry, Science, 247 (1990) 1439-1445.

[90] K.S. Suslick, G.J. Price, Applications of ultrasound to materials chemistry, Annual Review of Materials Science, 29 (1999) 295-326.

[91] Z. Zhang, D.W. Sun, Z. Zhu, L. Cheng, Enhancement of crystallization processes by power ultrasound: current state‐of‐the‐art and research advances, Comprehensive Reviews in Food Science and Food Safety, 14 (2015) 303-316.

[92] H. Kiani, D.-W. Sun, A. Delgado, Z. Zhang, Investigation of the effect of power ultrasound on the nucleation of water during freezing of agar gel samples in tubing vials, Ultrasonics Sonochemistry, 19 (2012) 576-581.

[93] H. Kiani, D.-W. Sun, Z. Zhang, The effect of ultrasound irradiation on the convective heat transfer rate during immersion cooling of a stationary sphere, Ultrasonics Sonochemistry, 19 (2012) 1238-1245.

[94] S.L. Hem, The effect of ultrasonic vibrations on crystallization processes, Ultrasonics, 5 (1967) 202-207.

[95] N. Lyczko, F. Espitalier, O. Louisnard, J. Schwartzentruber, Effect of ultrasound on the induction time and the metastable zone widths of potassium sulphate, Chemical Engineering Journal, 86 (2002) 233-241.

[96] S. Kim, C. Wei, S. Kiang, Crystallization process development of an active pharmaceutical ingredient and particle engineering via the use of ultrasonics and temperature cycling, Organic Process Research & Development, 7 (2003) 997-1001.

[97] Z. Guo, A.G. Jones, N. Li, The effect of ultrasound on the homogeneous nucleation of $BaSO_4$ during reactive crystallization, Chemical Engineering Science, 61 (2006) 1617-1626.

[98] C. Virone, H. Kramer, G. Van Rosmalen, A. Stoop, T. Bakker, Primary nucleation induced by ultrasonic cavitation, Journal of Crystal Growth, 294 (2006) 9-15.

[99] H. Harzali, F. Espitalier, O. Louisnard, A. Mgaidi, Sono-crystallization of $ZnSO_4 \cdot 7H_2O$, Physics Procedia, 3 (2010) 965-970.

[100] V.S. Nalajala, V.S. Moholkar, Investigations in the physical mechanism of sonocrystallization, Ultrasonics Sonochemistry, 18 (2011) 345-355.

[101] R. Grossier, O. Louisnard, Y. Vargas, Mixture segregation by an inertial cavitation bubble, Ultrasonics Sonochemistry, 14 (2007) 431-437.

[102] E.J. Anglin, L. Cheng, W.R. Freeman, M.J. Sailor, Porous silicon in drug delivery devices and materials, Advanced Drug Delivery Reviews, 60 (2008) 1266-1277.

[103] P. Ghosh, G. Han, M. De, C.K. Kim, V.M. Rotello, Gold nanoparticles in delivery applications, Advanced Drug Delivery Reviews, 60 (2008) 1307-1315.

[104] A.M. Smith, H. Duan, A.M. Mohs, S. Nie, Bioconjugated quantum dots for in vivo molecular and cellular imaging, Advanced Drug Delivery Reviews, 60 (2008) 1226-1240.

[105] C. Sun, J.S. Lee, M. Zhang, Magnetic nanoparticles in MR imaging and drug delivery, Advanced Drug Delivery Reviews, 60 (2008) 1252-1265.

[106] F. Leone, A. Gignone, S. Ronchetti, R. Cavalli, L. Manna, M. Banchero, B. Onida, A green organic-solvent-free route to prepare nanostructured zinc oxide carriers of clotrimazole for pharmaceutical applications, Journal of Cleaner Production, 172 (2018) 1433-1439.

[107] D. Rosenblum, N. Joshi, W. Tao, J.M. Karp, D. Peer, Progress and challenges towards targeted delivery of cancer therapeutics, Nature Communications, 9 (2018) 1410.

[108] Q. Hu, P.S. Katti, Z. Gu, Enzyme-responsive nanomaterials for controlled drug delivery, Nanoscale, 6 (2014) 12273-12286.

[109] G. Saravanakumar, J. Kim, W.J. Kim, Reactive‐oxygen‐species‐responsive drug delivery systems: promises and challenges, Advanced Science, 4 (2017) 1600124.

[110] Z. Shi, Q. Li, L. Mei, pH-Sensitive nanoscale materials as robust drug delivery systems for cancer therapy, Chinese Chemical Letters, 31 (2020) 1345-1356.

[111] C. Zheng, Y. Wang, S.Z.F. Phua, W.Q. Lim, Y. Zhao, ZnO–DOX@ZIF-8 core–shell nanoparticles for pH-responsive drug delivery, ACS Biomaterials Science & Engineering, 3 (2017) 2223-2229.

[112] H. Chen, Z. Ye, L. Sun, X. Li, S. Shi, J. Hu, Y. Jin, Q. Xu, B. Wang, Synthesis of chitosan-based micelles for pH responsive drug release and antibacterial application, Carbohydrate Polymers, 189 (2018) 65-71.

[113] C. Xu, Y. Yan, J. Tan, D. Yang, X. Jia, L. Wang, Y. Xu, S. Cao, S. Sun, Biodegradable nanoparticles of polyacrylic acid–stabilized amorphous $CaCO_3$ for tunable pH‐responsive drug delivery and enhanced tumor inhibition, Advanced Functional Materials, 29 (2019) 1808146.

[114] W. Cai, M. Guo, X. Weng, W. Zhang, G. Owens, Z. Chen, Modified green synthesis of $Fe_3O_4@SiO_2$ nanoparticles for pH responsive drug release, Materials Science and Engineering: C, 112 (2020) 110900.

[115] X. Liu, C. Wang, X. Wang, C. Tian, Y. Shen, M. Zhu, A dual-targeting Fe_3O_4@C/ZnO-DOX-FA nanoplatform with pH-responsive drug release and synergetic chemo-photothermal antitumor in vitro and in vivo, Materials Science and Engineering: C, 118 (2021) 111455.

[116] X.-G. Wang, Z.-Y. Dong, H. Cheng, S.-S. Wan, W.-H. Chen, M.-Z. Zou, J.-W. Huo, H.-X. Deng, X.-Z. Zhang, A multifunctional metal–organic framework based tumor targeting drug delivery system for cancer therapy, Nanoscale, 7 (2015) 16061-16070.

[117] S. Bharti, G. Kaur, S. Gupta, S. Tripathi, PEGylation of CdSe/ZnS core/shell nanoparticles and its behavior at different pH, Journal of Luminescence, 181 (2017) 459-466.

[118] T.-Y. Liu, S.-H. Hu, D.-M. Liu, S.-Y. Chen, I.-W. Chen, Biomedical nanoparticle carriers with combined thermal and magnetic responses, Nano Today, 4 (2009) 52-65.

[119] A.K. Wood, C.M. Sehgal, A review of low-intensity ultrasound for cancer therapy, Ultrasound in Medicine & Biology, 41 (2015) 905-928.

[120] Y. Liu, P. Bhattarai, Z. Dai, X. Chen, Photothermal therapy and photoacoustic imaging via nanotheranostics in fighting cancer, Chemical Society Reviews, 48 (2019) 2053-2108.

[121] M. Amoli-Diva, R. Sadighi-Bonabi, K. Pourghazi, Switchable on/off drug release from gold nanoparticles-grafted dual light-and temperature-responsive hydrogel for controlled drug delivery, Materials Science and Engineering: C, 76 (2017) 242-248.

[122] R. Elashnikov, P. Slepička, S. Rimpelova, P. Ulbrich, V. Švorčík, O. Lyutakov, Temperature-responsive PLLA/PNIPAM nanofibers for switchable release, Materials Science and Engineering: C, 72 (2017) 293-300.

[123] Z. Jin, K. Wu, J. Hou, K. Yu, Y. Shen, S. Guo, A PTX/nitinol stent combination with temperature-responsive phase-change 1-hexadecanol for magnetocaloric drug delivery: Magnetocaloric drug release and esophagus tissue penetration, Biomaterials, 153 (2018) 49-58.

[124] Y. Choi, J. Kim, S. Yu, S. Hong, pH-and temperature-responsive radially porous silica nanoparticles with high-capacity drug loading for controlled drug delivery, Nanotechnology, 31 (2020) 335103.

[125] R.G. Sousa, A. Prior-Cabanillas, I. Quijada-Garrido, J.M. Barrales-Rienda, Dependence of copolymer composition, swelling history, and drug concentration

on the loading of diltiazem hydrochloride (DIL. HCl) into poly [(N-isopropylacrylamide)-co-(methacrylic acid)] hydrogels and its release behaviour from hydrogel slabs, Journal of Controlled Release, 102 (2005) 595-606.

[126] X. Mou, Z. Ali, S. Li, N. He, Applications of magnetic nanoparticles in targeted drug delivery system, Journal of Nanoscience and Nanotechnology, 15 (2015) 54-62.

[127] A. Baeza, R. Castillo, A. Torres-Pardo, J. González-Calbet, M. Vallet-Regí, Electron microscopy for inorganic-type drug delivery nanocarriers for antitumoral applications: what does it reveal?, Journal of Materials Chemistry B, 5 (2017) 2714-2725.

Chapter 2: Medium-high Frequency Sonication Dominates Spherical-SiO$_2$ Nanoparticle Size

Abstract

Spherical SiO$_2$ nanoparticles (SSNs) have been inventively synthesized using the Stöber method with sonication at medium–high frequencies (80, 120, and 500 kHz), aiming to control SSN size and shorten reaction time. Compared to the conventional method, such sonication allowed the Stöber reaction complete in 20–60 min with a low molar ratio of NH$_4$OH/tetraethyl orthosilicate (0.84). Hydrodynamic diameters of 63–117 nm of SSNs were obtained under sonication with 80, 120, and 500 kHz of ultrasonic frequencies. Moreover, the SSNs obtained were smaller at 120 kHz than at 80 kHz in a multi–frequencies ultrasonic reactor, and SSN size decreased with increasing ultrasonic power at 20°C, designating the sonochemical unique character, namely, the SSN–size control is associated with the number of microbubbles originated by sonication. With another 500 kHz ultrasonic bath, the optimal system temperature for producing smaller SSNs was proven to be 20°C. Furthermore, similarly, SSN size decreased with increasing ultrasonic power at 500 kHz. The smallest SSNs (63 nm, hydrodynamic diameter by QELS, or 21 nm by FESEM) were obtained by sonication at 207 W for 20 min at 20°C and 500 kHz. Furthermore, SSN size increased slightly with increasing sonication time and volume, favouring the scale–up of SSN preparation. The mechanisms of controlling the SSN size were further discussed by the radical's role and effects of ammonia and ethanol concentration.
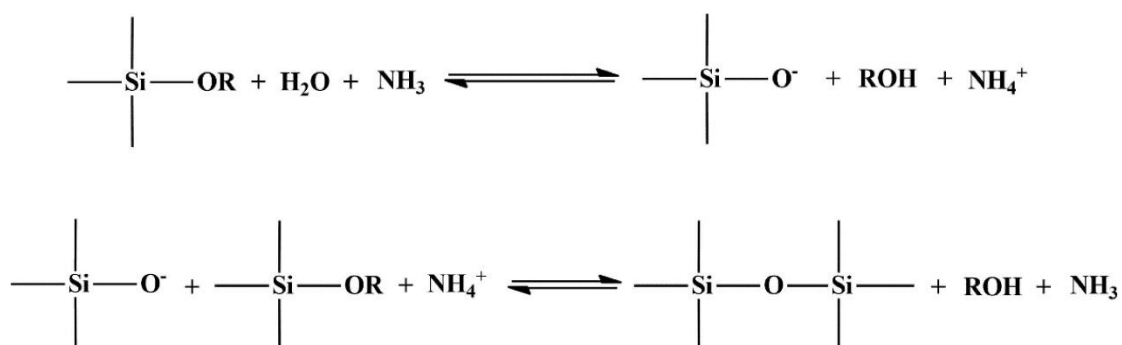
2.1 Introduction

Spherical SiO$_2$ nanoparticles (SSNs) are widely applied in biomedical fields including biosensors, DNA transfection, cancer treatment, etc.[1-3] The Stöber process, via the hydrolysis and polycondensation of tetraethyl orthosilicate (TEOS) in alkaline ethanol (Scheme 2.1), is a common method for the preparation of monodisperse SSNs.[4, 5] In the conventional process, SSN size is modulated by many factors, such as the ethanol/NH$_4$OH/TEOS/H$_2$O ratio, reaction temperature and time, etc.

Ismai et al. explored the effects of TEOS (0.2–0.4 mol/L) and ammonia (0.11–0.3 mol/L) concentrations on SSN size.[6] Both the hydrolysis and condensation rates become faster with increasing TEOS and ammonia concentrations, producing

fewer nuclei and larger particle sizes. Under the optimal conditions, 50 nm silica particles were obtained with 0.2 mol/L ammonia and 0.2 mol/L TEOS at ambient temperature for 24 h. Wang et al. also studied the effect of TEOS (0.22–1.115 mol/L) and ammonia concentrations on silica particle size in the mixture of water and isopropanol.[7] With a constant NH_4OH/TEOS molar ratio (0.81), 30 nm or 860 nm silica particles were obtained with 0.22 or 1.115 mol/L TEOS at 20°C for 5 h, respectively. As a catalyst, higher ammonia accelerates the hydrolysis and condensation and promotes the production of more oligomers to form larger particles. It is conspicuous that smaller SSNs are obtained with the lower NH_4OH/TEOS molar ratio, but long reaction times (5-24 h) are required, whereas the higher reaction rate with the higher NH_4OH/TEOS molar ratio leads to larger particle sizes (ca. 800 nm).[5] The sonochemical method has long been used in the preparation of nanoparticles and nanocrystals to accelerate the synthesis and reduce nanoparticle size.[8-11] Ultrasonic cavitation is generally regarded as the origin of sonochemistry, namely, the implosion of cavitation microbubbles generates extremely high local temperature and pressure, high–speed microjets, strong shock waves, and shear forces, which contribute to the fabrication of nanostructured materials.[12, 13] The number and size of cavitation bubbles are also critical for the fabrication of nanostructured materials. Cavitation bubble surfaces can act as crystal nucleation sites, leading to increasing nucleation rates.[14-16] Therefore, the reduction in crystal size and the narrowness of the crystal size distribution can be explained by the number of cavitation bubbles induced by sonication. Specifically, the number of cavitation bubbles increases with increasing ultrasonic frequency and power, resulting in an increasing number of crystal nuclei.[17, 18] Moreover, the activity of cavitation bubbles is substantially dependent on the size of the bubbles, which decreases with increasing ultrasonic frequency, but the size of the bubbles increases with increasing ultrasonic power.[19-23] In 1996, Enomoto et al. attempted to improve the Stöber process using sonication at 20 kHz and 1.9-25.4 W/cm^2 for 90 min at 20°C.[24] With 3.0 mol/L ammonia and 0.1 mol/L TEOS (NH_4OH/TEOS molar ratio: 30), however, larger SSN sizes (330-380 nm) were obtained by sonication compared to the 310 nm SSNs produced without sonication. This behaviour was explained by the presence of sonication-induced agglomeration. In 2018, Lin et al. reported the rapid synthesis of silica particles by ultrasound-assisted Stöber method.[25] With 1.36 mol/L ammonia and 0.58 mol/L TEOS (NH_4OH/TEOS molar ratio: 2.34) in 46 mL of the

reaction mixture, ca. 615 nm silica particles were obtained by 25 kHz sonication at 160 W for 5 min and stirred at 999 rpm simultaneously. In 2022, Kamila et al. found that the larger silica particles are generated by the sonochemical method as compared with the sol-gel Stöber method again.[26] In the preparation, the Stöber mixture containing 2.85 mol/L ammonia and 1 mol/L TEOS (NH₄OH/TEOS molar ratio: 2.85) with ethanol and water was stirred at 450 rpm for 90 min at room temperature, or sonicated with an ultrasonic probe for 30 min (5 s pulse on and 2 s pulse off). The average particle sizes obtained by the conventional sol-gel or sonochemical Stöber method were 223 nm or 398 nm, respectively.

In contrast, Rahman et al. obtained 93 nm SSNs by the Stöber method with sonication at 42 kHz for 7 h at ca. 45°C, however, it was just comparable to those generated using magnetic agitation with 1.87 mol/L ammonia and 0.7 mol/L TEOS (NH₄OH/TEOS molar ratio:2.67).[27] In 2009, Yao et al. reported the preparation of 80 nm SSNs with 4.89 of NH₄OH/TEOS molar ratio using the sonochemical method.[28] The mixture containing 8 mL of ammonia and 2.5 mL of TEOS with ethanol, water, and dye thionine was sonicated at 20 kHz and 100 W/cm^2 for 30 min under ambient air. To obtain smaller SSNs, furthermore, the NH₄OH/TEOS molar ratio was decreased to 0.25 in a Stöber mixture containing 1 mL of ammonia and 6.3 mL of TEOS with ethanol, water, and a certain amount of PEG 1000.[29] The reaction was carried out with ultrasonic vibration for 5.5 h at 45°C. In addition, some post-treatments, such as aging and calcination, were performed to achieve an average size of 9 nm.

$$\equiv\text{Si}-\text{OR} + \text{H}_2\text{O} + \text{NH}_3 \rightleftharpoons \equiv\text{Si}-\text{O}^- + \text{ROH} + \text{NH}_4^+$$

$$\equiv\text{Si}-\text{O}^- + \equiv\text{Si}-\text{OR} + \text{NH}_4^+ \rightleftharpoons \equiv\text{Si}-\text{O}-\text{Si}\equiv + \text{ROH} + \text{NH}_3$$

Scheme 2.1 Stöber preparation of monodisperse SSNs by hydrolysis and condensation of TEOS.[2]

To date, the ultrasonic frequencies applied for the sonochemical preparation of silica particles were between 20 and 42 kHz, leading to larger silica particles (mostly over 300 nm and rarely below 50 nm). Also, most ultrasonic treatment times exceed 1 h. Therefore, the proposed advantages of sonication, i.e., reducing SSNs size and reaction time, are not evident at low frequencies. In this work, the Stöber reaction mixture has been sonicated at medium–high frequencies (80, 120, and 500 kHz) to obtain smaller SSNs sizes (80 kHz: 40 nm, 120 kHz: 32 nm, 500 kHz: 21 nm) in up to 1 h reaction. The effects of ultrasonic frequency and power, temperature, sonication time, and reaction volume on SSN size and yield under a static air atmosphere have been investigated. The roles of the size and number of cavitation microbubbles, the radicals initiated under sonication, and the concentration of ammonia and ethanol in modulating SSN size are discussed.

2.2 Methods

2.2.1 Materials

TEOS (98.0%, Aldrich), ethanol (≥99.8%, Sigma-Aldrich), NH_4OH (30.0%, Carlo Erba), n-butanol (98.0%, E. Merck, Darmstadt) were used without additional purification.

2.2.2 Experimental devices

A low–frequency ultrasonic device (20 kHz) consists of an ultrasonic generator (Maximum electrical output power: 70 W) equipped with a titanium horn (tip diameter: 13 mm) and a 20–mL cylindrical glass reactor (HNG–20500–SP, Hainertec (Suzhou) Co., ltd, China). The reaction temperature was controlled by an ice bath. The diagram of the setup refers to our previous work.[30] A multi–frequency device (40, 80, and 120 kHz) consists of a sonic digital cleaning generator (Maximum electrical output power: 150 W) and a 5.6–L ultrasonic bath (28 cm × 20 cm × 10 cm) equipped with cooling water serpentine at 1 cm from the bottom (MG 200, Weber Ultrasonics, Germany, Fig. 2.1A). A high–frequency device (500 kHz) consists of an ultrasonic cleaning generator (Maximum electrical output power: 250 W) and a 5.6–L ultrasonic bath (28 cm × 20 cm × 10 cm) equipped with cooling water

serpentine at 1 cm from the bottom (UMC, Weber Ultrasonics, Germany, Fig. 2.1B). The ultrasonic powers delivered were determined calorimetrically with water as heating media and all ultrasonic power mentioned below refers to the power measured calorimetrically.[31] As a conventional method, a 20–mL cylindrical glass reactor placed on a magnetic stirrer (AREX VELP Scientifica, Italy) was also used to prepare SSNs at room temperature for comparison. A centrifuge (Allegra 64R Benchtop Centrifuge, Beckman Coulter, Italy) was used to collect the prepared SSNs from reaction systems and washing liquids. The SSNs were collected with the centrifuge (20,000 rpm, 15 min) and washed twice with ethanol and then washed once with distilled water.
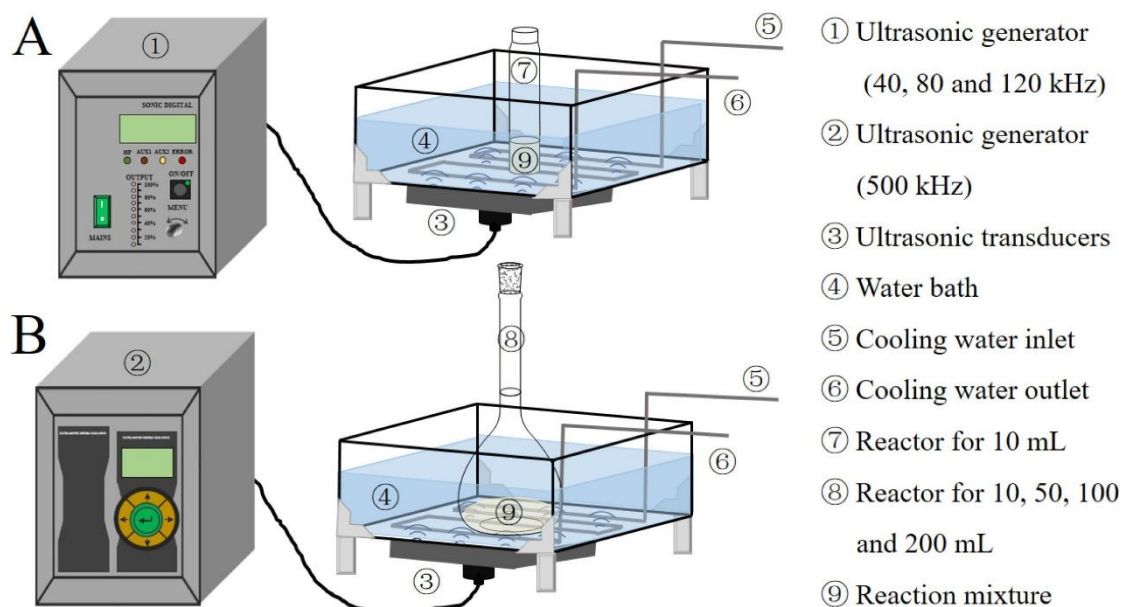

Fig 2.1 **Setups for sonication with ultrasonic generators and baths (A) 40, 80, and 120 kHz; (B) 500 kHz.**

2.2.3 Typical runs of SSNs preparation

All the preparation of SSNs was carried out under air atmosphere. The sonochemical processes of the SSNs preparation with various ultrasonic reactors are described as follows:

(A) SSNs preparation using sonication at 20 kHz: 6.00 mL of 99.8% ethanol, 3.00 mL H$_2$O, and 0.25 mL of TEOS were added to a 20–mL cylindrical reactor (ID: 25 mm) in turn. Subsequently, 0.40 mL of 8.1% NH$_4$OH as a catalyst was added to the above mixture, so that the molar ratio of 99.8% ethanol/8.1% NH$_4$OH/TEOS/H$_2$O was 92.92/0.84/1.00/150.89. Then, ca. 10 mL of the above reaction mixture was sonicated using an ultrasonic horn with 20 kHz and 40 W for 60 min at 20°C in an ice bath. The ultrasonic power density and power intensity were calculated to be 4.15 W/mL and 30.15 W/cm^2, respectively. For comparison, ca. 10 mL of the same reaction mixture as above was stirred using a magnetic stirrer with 450 rpm at 20°C for 24 h.

(B) SSNs preparation using sonication at 40, 80, and 120 kHz: 3 L of water as an ultrasonic medium was placed in a 5.6–L ultrasonic bath. Firstly, the degassing was performed for 20 min with sonication, and the temperature of the ultrasonic bath was maintained at 20 ± 0.3°C with cooling water. 10 mL of the same reaction mixture as above in 40–mL cylindrical reactor (ID: 25 mm) was sonicated with different ultrasonic frequencies and powers (40 kHz: 97 W; 80 kHz: 17–63 W; 120 kHz: 17–78 W) at 20°C for 20 min respectively.

(C) SSNs preparation using sonication at 500 kHz: The same ultrasonic medium and the temperature control as above were applied in a 500 kHz ultrasonic bath. The same reaction mixtures as above with different volumes (10–200 mL) were sonicated with different ultrasonic powers (63–207 W) at 15-35°C for 20–60 min, respectively.

2.2.4 Characterization of SSNs

The collected SSNs were dispersed in 4 mL of distilled water. 1 mL of the above SSNs dispersion was centrifuged and oven-dried at 45°C to measure yield with the weighing method. The remaining 3 mL of the SSNs dispersion was used for particle size analysis with Quasi Elastic Light Scattering (QELS). Unless otherwise specified, the SSN size mentioned herein refers to the hydrodynamic SSN size determined by QELS. After the measurement with QELS, the white SSNs were collected by centrifugation (20,000 rpm for 15 min) and lyophilized for the further characterization with Field Emission Scanning Electron Microscope (FESEM),

Fourier–transform infrared spectroscopy (FT–IR), Powder X–ray diffraction (XRD), and Thermogravimetric analysis (TGA), etc.

SSN particle sizes were measured via a QELS method at 25°C using particle sizing Brookhaven Instruments (Holtsville, NY, USA) with the software of 90 plus/BI–MASS. The scattering angle and operating wavelength were 90° and 675.0 nm, respectively. The samples were measured in water. Ultra–high resolution FESEM measurements were performed on a Tescan S9000G FESEM 3010 microscope (30 KeV) equipped with a high–brightness Schottky emitter. For analysis, the powder samples were deposited on a stub coated with a conducting adhesive and inserted in the chamber by a fully motorized procedure. The FT–IR spectra (Spectrum Two, PerkinElmer, USA) were measured by a spectrometer from 500 to 4000 cm^{-1} at 2 cm^{-1} resolution with 64 scans. XRD patterns were collected with a PW3050/60 X'Pert PRO MPD diffractometer from PANalytical working in Bragg–Brentano geometry, using as a source the high–powered ceramic tube PW3373/10 LFF with a Cu anode (Cu Kα1 radiation λ = 1.5406 Å) equipped with a Ni filter to attenuate K_{β}. Scattered photons were collected by a real-time multiple strip (RTMS) X'celerator detector. Data were collected in the 5° ≤ 2θ ≤ 90° angular range, with 0.02° 2θ steps. The powdered sample was examined in its as-received form and posed in a spinning sample holder to minimize the preferred orientations of crystallites. TGA was used to measure the thermal stability of SSNs. About 10 mg of the sample was heated to 1000°C under a nitrogen atmosphere with an airflow of 20 mL/min. In the first step, the temperature increased from 35°C to 120°C with a heating rate of 10°C/min and held at 120°C for 10 min. In the second step, the temperature increased from 120°C to 800°C at 20°C/min and held at 800°C for 10 min. In the third step, the temperature increased from 800°C to 1000°C at 20°C/min and maintained at 1000°C for 5 min.

2.3   Results and discussion

The physical effects of ultrasonic cavitation, such as local temperature and pressure, shear stress, shock wave, microjet, etc., favor mass transfer and heat transfer, and in particular, promoting the reactions in heterogeneous systems. TEOS is poorly soluble in water but is miscible with alcohol.[32] Ammonia is very volatile, meaning that both TEOS and ammonia may accumulate on the surface of

the cavitation bubbles, accelerating the hydrolysis and condensation of TEOS around the active cavities.[33] Probably, the radicals generated under sonication are also involved in the above reactions.[34] Thus, sonication can be employed to enhance the hydrolysis and condensation of TEOS.[35] It was possible to produce the smaller SSNs when the reactant ratios were optimized, in particular, when reducing the ammonia concentration during sonication.[27, 34]

2.3.1 Optimization of reactants ratio

The effect of different reactant ratios on the size of the SSNs was investigated using the Box–Behnken methodology. In 6 mL of ethanol, the volume ranges of NH$_4$OH, H$_2$O, and TEOS were selected to be: 0.40-0.60 mL, 2.0-3.0 mL, and 0.25-1.00 mL for the optimized experiments. Experimental design and data analyses were performed using Design–Expert software (free trial version 12.0, Stat–Ease, Inc., USA). All experiments were carried out in duplicate. Approximate 10 mL of the Stöber reaction mixture with various reactants ratios was sonicated at 120 kHz and 78 W for 20 min at 20°C. As a result, the smallest SSNs (average size: 71 nm) were obtained with the optimized Stöber mixture (99.8% ethanol: 6.00 mL, 8.1% NH$_4$OH: 0.40 mL, 98.0% TEOS: 0.25 mL, H$_2$O: 3.00 mL). The optimization results are shown in Table 2.1 and Fig. 2.2. The optimal reactant volume ratio was: ethanol/NH$_4$OH/TEOS/H$_2$O = 24.0/1.6/1.0/12.0, which is equivalent to a molar ratio of 92.92/0.84/1.00/150.89.

The response polynomial model to calculate SSN size (Y), measured using QELS, can be expressed as a function of the proportions of NH$_4$OH (X$_1$), H$_2$O (X$_2$), and TEOS (X$_3$). The relationship between responses (Y) and variables can be found below:

Y=163.66+352.19X$_1$-88.21X$_2$+185.15X$_3$

The optimized solution (99.8% ethanol: 6.00 mL, 8.1% NH$_4$OH: 0.40 mL, 98.0% TEOS: 0.25 mL, H$_2$O: 3.00 mL) was chosen for the preparation of SSNs. The SSN size (71 nm) obtained was in good agreement with the predicted values (86 nm).

Table 2.1 The optimization of reactants ratio in terms of SSN size (measured by QELS). Other conditions: ca. 10 mL of the mixture, containing 6 mL of ethanol, was sonicated at 120 kHz and 130 W for 20 min at 20°C in a 3 L water bath.

|	8.1% NH_4OH (mL/mM)	H_2O (mL/mM)	Volume of TEOS (mL/mM)	Particle size (nm) (batch 1)	Particle size (nm) (batch 2)	Average particle size (nm)	Standard deviation
1	0.50/0.10	3.00/15.86	1.00/0.43	245.1	247.9	246.5	2.0
2	0.50/0.11	2.50/14.43	0.62/0.29	261.5	259.6	260.6	1.3
3	0.60/0.12	3.00/16.29	0.62/0.27	236.2	237.3	236.8	0.8
4	0.40/0.09	2.00/12.31	0.62/0.31	240.7	245.5	243.1	3.4
5	0.60/0.13	2.00/12.04	0.62/0.30	296.0	304.2	300.1	5.8
6	0.50/0.11	2.50/14.43	0.62/0.29	259.0	260.4	259.7	1.0
7	0.40/0.08	2.50/14.02	1.00/0.45	316.3	306.4	311.4	7.0
8	0.40/0.09	2.50/15.17	0.25/0.12	128.1	127.5	127.8	0.4
9	0.40/0.08	3.00/16.62	0.62/0.28	105.0	98.1	101.6	4.9
10	0.50/0.11	2.50/14.43	0.62/0.29	264.6	261.5	263.1	2.2
11	0.50/0.12	2.00/12.69	0.25/0.13	223.2	216.6	219.9	4.7
12	0.50/0.11	2.00/11.69	1.00/0.47	319.9	324.5	322.2	3.3
13	0.60/0.12	2.50/13.74	1.00/0.44	328.5	328.0	328.3	0.4
14	0.50/0.10	3.00/17.08	0.25/0.11	100.6	108.3	104.5	5.4
15	0.60/0.13	2.50/14.84	0.25/0.12	202.3	198.60	200.5	2.6
16	0.50/0.10	3.00/16.46	0.62/0.27	205.8	209.3	207.6	2.5
17	0.50/0.11	2.00/12.17	0.62/0.30	253.3	251.8	252.6	1.1
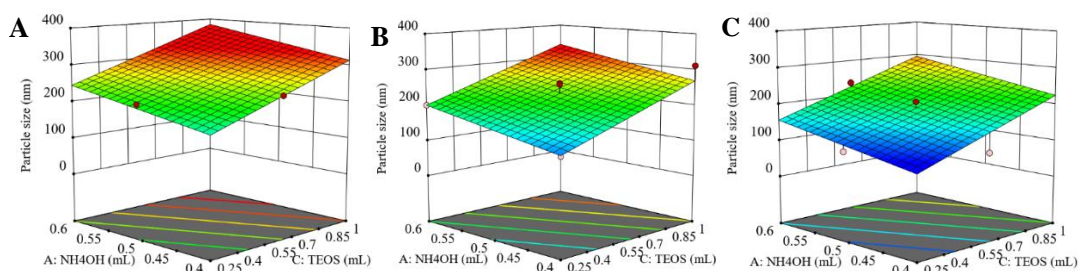
Fig. 2.2 Effects of proportions of ammonia and TEOS on SSN size in 2.0 mL (A), 2.5 mL (B), and 3.0 mL (C) of H_2O and 6 mL of ethanol. Other conditions: ca. 10 mL of the mixture was sonicated at 120 kHz and 130 W for 20 min at 20°C in a 3 L water bath.

2.3.2 Effects of ultrasonic frequency and power on SSN size and yield

With the optimal reactant ratio obtained in the above study, ca. 10 mL of the above reaction mixture was either stirred or sonicated at lower frequencies (20 and 40 kHz) at 20°C. During 24 h of agitation (450 rpm), unfortunately, the reaction mixture always appeared clear and transparent state, and no white suspension appeared. The same phenomenon was observed during 20 kHz sonication with an ultrasonic horn at 40 W for 60 min. It is speculated that the NH$_4$OH/TEOS molar ratio (0.84) used in the above Stöber mixtures was lower as compared with those (NH$_4$OH/TEOS molar ratio: 2.33–30.00) reported in previous studies.[24-27] In contrast, SSNs were produced under the 40 kHz sonication at 97 W for 20 min in an ultrasonic bath, but preparation reproducibility was poor. The follow-up studies, therefore, focused on medium-high frequency (80 and 120 kHz, and 500 kHz) with two ultrasonic baths, respectively. Due to the difference in their structures and power ranges of ultrasonic reactors, unfortunately, the results obtained using the 500 kHz ultrasonic bath could not be compared with results obtained using the multi-frequencies (40–120 kHz) ultrasonic bath.

Fig. 2.3A and B show the effects of the ultrasonic frequency and power on the SSN size and yield obtained in the multi-frequency ultrasonic bath (80 and 120 kHz), respectively. As shown in Fig. 2.3A, the SSN sizes obtained at 120 kHz were distinctly smaller than those obtained at 80 kHz and the SSN size decreased with increasing ultrasonic powers. Under sonication, the relationship between SSN sizes and ultrasonic power with various frequencies can be well-fitted by the linear equation, as follows:

$$d_{80kHz} = -0.741 \times P_{US} + 129.44, \quad R^2 = 0.978$$

(2-1)

$$d_{120Hz} = -0.413 \times P_{US} + 104.28, \quad R^2 = 0.975$$

(2-2)

where d_{80kHz} and d_{120kHz} are the hydrodynamic diameters of SSNs obtained at 80 and 120 kHz; P_{US} is the ultrasonic power.
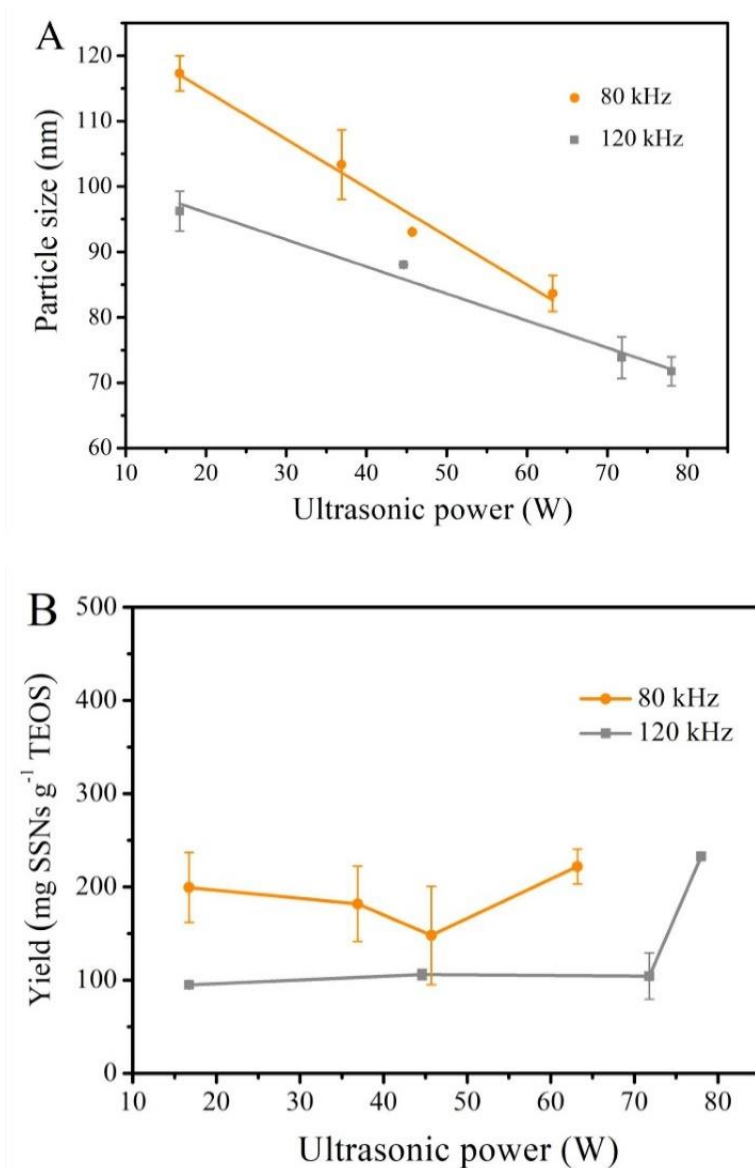
Fig. 2.3 Dependence of SSN hydrodynamic diameter size by QELS (A) and yield (B) on ultrasonic power at 80 and 120 kHz. Conditions: ca. 10 mL of the mixture (99.8% ethanol: 6.00 mL; 8.1% NH_4OH: 0.40 mL; 98.0% TEOS: 0.25 mL; H_2O: 3.00 mL) was sonicated for 20 min at 20°C in a 3 L water bath.

In terms of equations (2-1) and (2-2), the slope (0.741) obtained by 80 kHz is higher than that (0.413) obtained by 120 kHz, indicating that the effect of ultrasonic power on SSN size is more profound at 80 kHz than at 120 kHz. At 80 kHz, the

hydrodynamic SSN sizes decreased from 117 to 84 nm with increasing ultrasonic power (17–63 W). At 120 kHz, the SSN sizes decreased from 92 to 72 nm with increasing ultrasonic power (17–78 W).

In Fig. 2.3B, the SSN yields at 120 kHz were obviously lower than those obtained at 80 kHz. At lower power settings, SSN yields slightly decreased at 80 kHz as ultrasonic power increased, while the yields changed minimally at 120 kHz. At the highest ultrasonic power, SSN yields increased sharply at 80 and 120 kHz. This unpredictable result may be caused by the complex effects of ultrasonic frequency and power, which should be further explored in the future. Fig. 2.4 shows the dependence of the SSN size and yield obtained on the ultrasonic power in a high-frequency ultrasonic bath (500 kHz).
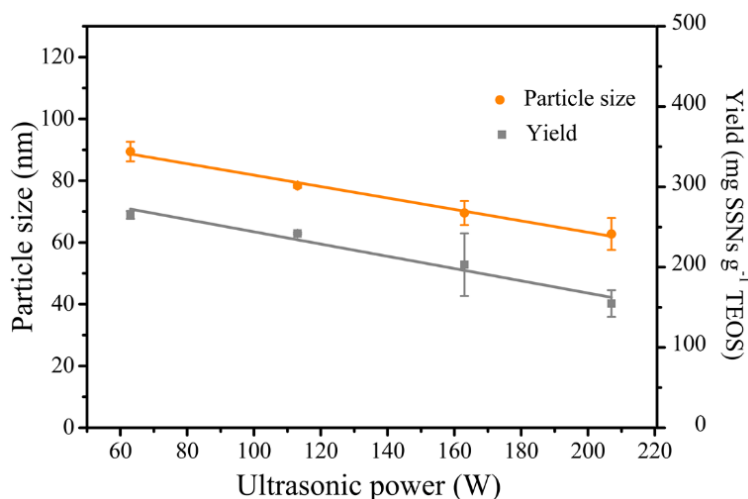

Fig. 2.4 Dependence of SSN hydrodynamic diameter size by QELS and yield on ultrasonic power at 500 kHz. Conditions: ca. 10 mL of the mixture (99.8% ethanol: 6.00 mL; 8.1% NH₄OH: 0.40 mL; 98.0% TEOS: 0.25 mL; H₂O: 3.00 mL) was sonicated for 20 min at 20°C in a 3 L water bath.

As shown in Fig. 2.4, the SSN sizes obviously decreased with increasing ultrasonic power. Under 500 kHz sonication, the relationship between SSN sizes and ultrasonic power can be also well-fitted by the linear equation (2-3). In terms of equation (2-3), the slope (0.185) obtained by 500 kHz is quite low, indicating that

the effect of ultrasonic power on SSN size is relatively less at 500 kHz. The smallest SSNs (63 nm by QELS, or 21 nm by FESEM) were obtained by sonication at 500 kHz and 207 W for 20 min at 20°C. Moreover, the yield of SSNs linearly decreased with increasing power and reached a minimum value at 207 W (155 mg SSNs/g TEOS), as shown in equation (2-4):

$$d_{500kHz} = -0.185 \times P_{US} + 100.31, \quad R^2 = 0.991 \tag{2-3}$$

$$Y_{500kHz} = -0.764 \times P_{US} + 320.51, \quad R^2 = 0.952 \tag{2-4}$$

where d_{500kHz} is the hydrodynamic diameters of SSNs obtained at 500 kHz; P_{US} is the ultrasonic power; Y_{500kHz} is the yield of SSNs obtained at 500 kHz.

In general, the smaller bubbles cause Rayleigh contraction, whereas larger bubbles are not involved in the sonochemical reaction.[27] Sonication with medium–high frequencies (80–1100 kHz) generated more numerous and smaller microbubbles than that at low frequencies (20–42 kHz), thus increasing the number of active bubbles, which refer to active bubbles with the optimal sizes that can produce stronger physical and chemical phenomena, such as reactive oxygen species, sonoluminescence, sonochemluminescence, etc.[18, 20, 21, 36, 37] In addition, the amount of water vapor trapped inside bubbles at the collapse decreases with increasing ultrasonic frequency, resulting in highly active bubbles, meaning that those inactive bubbles became active and those active bubbles turned into more active ones.[38] Consequently, the number of "active bubbles" remarkably increased under the sonication with the higher frequencies, leading to smaller SSNs.

In 1999, Burdin et al. reported that active bubbles have a typical radius of 8 µm by 20 kHz sonication as determined by laser light diffraction.[39] Also, it was reported that the average bubble radius (135 µm) at 20 kHz was about 6.8 times that (20 µm) at 40 kHz, while the average number of bubbles at 40 kHz was about 4.6 times that at 20 kHz.[40] In 2002, Yasui calculated the range of the ambient bubble radius with increasing ultrasonic frequency, i.e., 0.1–100 µm, 0.1–10 µm, and 0.1–3 µm at 20, 140, and 1000 kHz.[38] In 2005, Lee et al. and Brotchie et al. summarized that the ranges of bubble size created by 20, 515, and 1100 kHz in

water were 2.0–25.0, 2.8–3.7, and 0.9–1.38 μm, respectively.[19, 20] In 2021, Yasui reported the ambient bubble radii generated under various frequencies, i.e., 5 μm for 20 kHz, 3.5 μm for 100 and 300 kHz, and 1 μm for 1 MHz.[23] In particular, both the bubble dynamics and the bubble size are very similar between high frequencies.[41] In 2009, Brotchie et al. reported that the ambient bubble radii in the frequency range of 200–650 kHz, i.e., 3.9, 3.2, and 2.9 μm for 213, 355, and 647 kHz, respectively.[20] In 2013, Merouani et al. summarized the mean measured bubble radius induced by various medium–high frequencies, i.e., 3.9–8.0 μm at 213–230 kHz, 3.2–7.0 μm at 355–350 kHz, 2.8–4.3 μm at 515 kHz, 2.7 μm at 860 kHz, and 0.9–2.0 μm at 1000–1140 kHz.[21, 42] In 2021, Dehane et al. reported that the optimum ambient bubble radius (3.1 and 2.4 μm) was achieved at 300 and 515 kHz.[43] Moreover, the number of bubbles depends strongly on the operating parameters of the sonication.[44, 45] The increasing ultrasonic frequency leads to a substantial increase in the number of bubbles formed in the reactor.[42] Pétrier et al. reported the number of active bubbles, i.e., $0.73–1.1 \times 10^4$, $5.2–5.4 \times 10^6$, $3.7–5.3 \times 10^7$, and $6.4–9.1 \times 10^7$ N (L^{-1} s^{-1}) created by 20, 200, 500, and 800 kHz.[44, 45] Merouani et al. reported the number of active bubbles, i.e., 2.8×10^7, 3.9×10^8, 3.0×10^9, and 3.1×10^9 N (L^{-1} s^{-1}) created by 300, 585, 860, and 1140 kHz.[42] Therefore, the number of bubbles increases with the frequency increase while the size of bubbles decreases. It is inferred that the size of SSNs may be controlled by the number of bubbles and the size of the bubbles, as shown in Fig. 2.3A.

On the other hand, increasing ultrasonic power resulted in more numerous and larger microbubbles.[20, 21, 23, 37, 46] It has been demonstrated that the optimal ambient radius increased linearly with increasing acoustic amplitude up to 3 atm. However, slight minima of optimal radius were observed for the curves obtained at 500 and 1000 kHz.[21] In 2016, Merouani and Hamdaoui studied the effect of power intensity on the optimum ambient bubble radius created with various medium–high frequencies, i.e., at 140, 515, and 1000 kHz, 11.1, 2.5, and 1.5 μm with 0.75 W/cm^2, while 13.25, 3.0, and 1.6 μm with 1 W/cm^2, respectively.[37] As shown in Fig. 2.3A and 2.4, the SSN size generally decreased with increasing ultrasound power. Combining the effect of the ultrasonic frequency on the particle size of SSNs, it can be speculated that the SSN size is mainly controlled by the number of active bubbles, not by the size of bubbles, as TEOS and ammonia are more evenly distributed around the larger number of active bubbles. Therefore,

smaller SSNs were generated with increasing ultrasonic powers, and the smallest SSNs (63 nm) were achieved by 500 kHz sonication at highest ultrasonic power (207 W).

As shown in Fig. 2.3B, the yields of SSNs obtained at 120 kHz were significantly lower than those obtained at 80 kHz within a comparable ultrasonic power range. For the given amounts of TEOS and ammonia in the reaction system, the number of cavitation bubbles increased with increasing ultrasonic frequencies, resulting in better dispersion of TEOS and ammonia and the decreasing concentration at nucleation sites, thereby the lower yield. At 500 kHz, the yield of SSNs decreased with increasing power and reached a minimum value at 207 W (155 mg SSNs/g TEOS). Similar to the effect of frequency, the larger number of active bubbles were generated as the increasing power, leading to TEOS and ammonia being more dispersed, thereby decreasing the yield of SSNs.

2.3.3 Influence of reaction volume on SSN size and yield

As presented above, the smallest SSNs (63 nm) and the corresponding yields (155 mg SSNs/g TEOS) were obtained in ca. 10 mL of reaction mixture sonicated at 500 kHz, 207 W for 20 min at 20°C. In the larger reaction volume (ca. 50 mL), however, the reaction mixture always appeared clear and transparent state, and no white suspension appeared during 20 min of sonication. To scale up SSNs synthesis, the sonication time was extended to 60 min for each batch of reaction. The influence of sonication time on SSN size and yield will be discussed in Section 2.3.4. 50–200 mL of the reaction mixture was sonicated at 500 kHz, 207 W for 60 min at 20°C, respectively. Fig. 2.5 shows the sizes and yields of the SSNs prepared at larger volumes.

The average hydrodynamic sizes of SSNs reached 66, 68, and 77 nm in 50, 100, and 200 mL, respectively, which are 5–23% higher than those (63 nm) prepared in 10 mL of the reaction mixture. It suggests that SSN–synthesis scale–up is feasible in the same ultrasonic reactor, and the synthesis efficiency very slightly fluctuates over the 50–200 mL range.
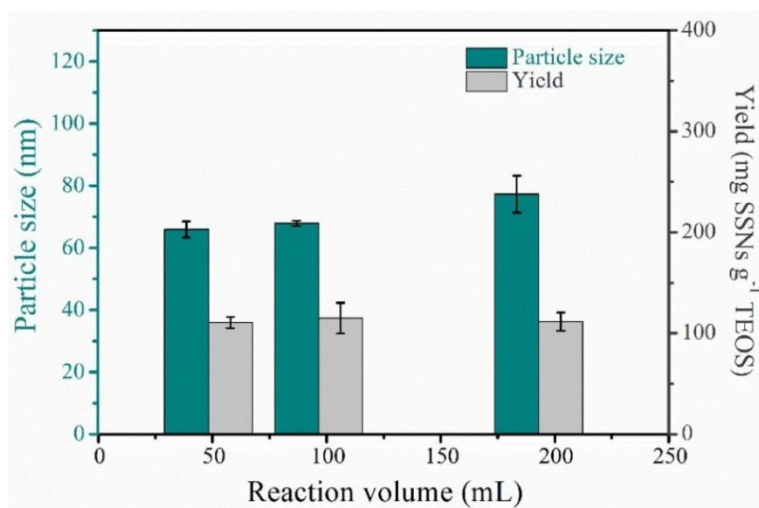
Fig. 2.5 Influence of reaction volume on SSN size (QELS) and yield. Conditions: various volumes of the mixture (99.8% ethanol/8.1% NH$_4$OH/98.0% TEOS/H$_2$O = 24.0:1.6:1.0:12.0 (volume)) were sonicated at 500 kHz, 207 W for 60 min at 20°C in a 3 L water bath.

2.3.4 Dependence of SSN size and yield on the system temperature

The cavity number, size, collapse intensity and local temperature, and sonochemical efficiency are strongly dependent on the bulk–liquid temperature.[46, 47] Fig. 2.6 shows that a larger SSN size and higher yield were achieved at 15°C than at 20°C under 60 min sonication at 500 kHz and 207 W. Upon increasing the temperature further, a few SSNs were produced at 25°C. More surprisingly, the reaction mixture always appeared clear and transparent state and no white suspension appeared during 60 min sonication at 35°C.

Generally, the number and size of cavitation bubbles increased with increasing bulk temperature.[46, 47] Similarly to the effects of ultrasonic frequency and power, the increasing number of microbubbles generated at 20°C resulted in smaller SSNs and lower yields. This is consistent with that the nucleation rate increased with increasing temperature.[27, 48] The number of cavitation bubbles increased with increasing temperature, resulting in better dispersion of TEOS and ammonia and

47

the decreasing concentration at nucleation sites, thereby dropping the yield of SSNs. Upon further increasing the temperature to 25°C and 35°C, the increasing number of bubbles decreased the concentration of TEOS and ammonia to a greater extent at nucleation sites, thereby limiting SSN formation with a lower initial ratio of NH$_4$OH/TEOS (0.84).
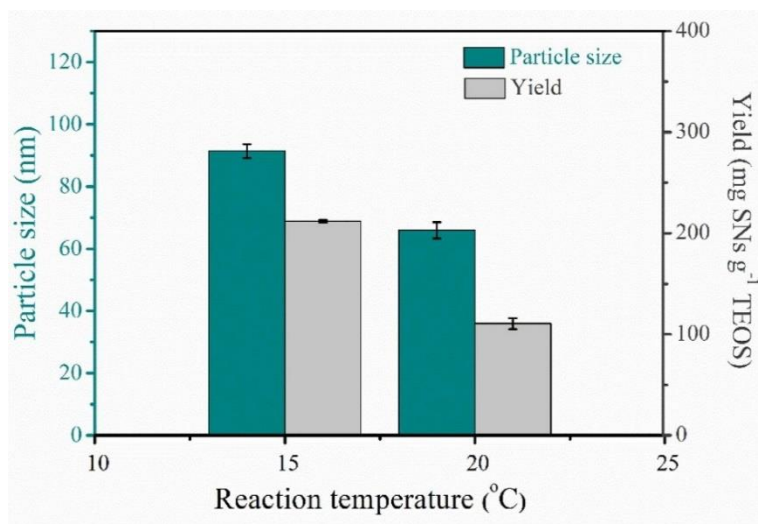

Fig. 2.6 Dependence of SSN size (QELS) and the yield on the reaction temperature.

Conditions: ca. 50 mL of the mixture (99.8% ethanol: 30.00 mL; 8.1% NH$_4$OH: 2.00 mL;

98.0% TEOS: 1.25 mL; H$_2$O: 15.00 mL) was sonicated at 500 kHz, 207 W for 60 min in a 3

L water bath.

2.3.5 Influence of sonication time on SSN size and yield

Generally, the deposition thickness on the SSNs increases by unceasing hydrolysis and condensation with the sonication time.[24] As can be seen in Fig. 2.7, the SSN size increased, while the yields slightly fluctuated, with longer sonication at 500 kHz and 207 W at 20°C.
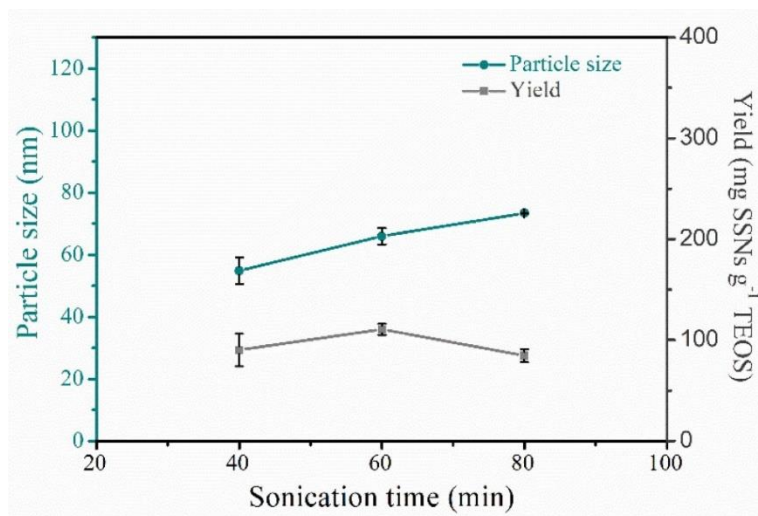
Fig. 2.7 Influence of sonication time on SSN size (QELS) and yield. Conditions: ca. 50 mL

of the mixture (99.8% ethanol: 30.00 mL; 8.1% NH$_4$OH: 2.00 mL; 98.0% TEOS: 1.25 mL;

H$_2$O: 15.00 mL) was sonicated at 500 kHz, 207 W at 20°C in a 3 L water bath.

2.3.6 Further sonochemical mechanism dominating SSN size

To further probe the physicochemical effect of ammonia and ethanol on SSN formation, the amount of ammonia was reduced from 0.40 mL to 0.30 mL, and the amount of ethanol was decreased from 6.00 mL to 4.50 mL in the Stöber reaction system in separate experiments. Table 2.2 shows that no SSNs are obtained with the decreased levels of ammonia and ethanol in ca. 10 mL of the mixture under sonication at 500 kHz, 207 W for 20 min at 20°C. This indicates that the proportions of both ammonia and ethanol are critical factors for SSN formation even under sonication and that the active radicals generated during sonication may not be the driving factor of the process. To ascertain the role of these radicals, 10 μL of hydrophobic n-butanol was added into ca. 10 mL of the reaction mixture to scavenge the radicals generated in-situ during sonication at 500 kHz, 207 W for 20 min at 20°C.[49] As shown in Table 2.2, the influence of n-butanol on SSN size (59 nm) and yield (172 mg SSNs/g TEOS) was negligible.

Table 2.2 Effect of reducing ethanol and NH₄OH amount and adding n-butanol. Other conditions: ca. 10 mL of the mixture, containing 3.00 mL of H_2O and 0.25 mL of TEOS, sonicated at 500 kHz and 207 W for 20 min at 20°C in 3 L of water bath.

	Ethanol (mL)	8.1% NH₄OH (mL)	n-butanol (μL)	Particle size (nm)	Yield (mg SSNs/g TEOS)
0	6.00	0.40	0	63±3	155±25
1	6.00	0.30	0	-	-
2	4.50	0.40	0	-	-
3	3.00	0.40	0	-	-
4	6.00	0.40	10	59±2	172±14

Note: The symbol "-" indicates that no SSNs formation was observed.

The very high temperatures and pressures of collapsing gas bubbles lead to the thermal dissociation of water vapor into OH radicals and H atoms during the sonication. Both the formation of OH radicals and the role in the degradation of organics in aqueous solutions under sonication with various frequencies have been extensively demonstrated in previous works.[30, 44, 50, 51] In 1996, Hoffmann et al. found that the degradation of TNT is more efficient at 500 kHz than at 20 kHz. The enhanced efficiency of irradiation at 500 kHz may be due to a higher rate of OH radicals production.[50] In 1997, Petrier and Francony reported the sonochemical degradation of phenol with different frequencies, 20, 200, 500, and 800 kHz. It was found that the reaction rates involving OH radicals (H_2O_2 formation and phenol degradation) have maximal values at 200 kHz, which was attributed to the better availability of OH radicals outside of the bubble of cavitation.[44, 52] Electron paramagnetic resonance (EPR) is a highly sensitive method for measuring radicals and is a valuable tool for identifying the effect of OH radicals on the synthesis of SSNs. Fortunately, the dependence of OH radicals production detected by EPR on the sonication conditions, such as ultrasonic frequency and power, system temperature, dissolved gas, radical scavenger, as well as the configuration of ultrasonic reactors, has been very well known.[53-57] In 2001 and 2002, Topaz et al. reported the gradual increase of the DMPO–OH adduct signal with increasing sonication intensity at 20 kHz and 40 kHz at 20°C.[53, 54] Similar results were also demonstrated by Režek Jambrak et al. recently.[57] Furthermore, Kubo et al. found that the concentration of DMPO–OH increases with the ultrasound power intensity (0.25–3 W/cm^3) at 50 kHz for 90 min at 20°C, but it decreases with the reaction

temperature (20–40°C) with the ultrasonic power intensity of 1 W/cm^3 at 50 kHz for 90 min.[55] In 2015, Zhang et al. comprehensively studied the effect of ultrasound frequency, power, temperature, etc., on the intensity of DMPO/1–hydroxylethyl free radical spin adducts in model wine. It demonstrated that the intensity of DMPO/1–hydroxylethyl free radical spin adducts increases with the increasing frequencies (45, 80, and 100 kHz) at 300 W and the increasing power (120, 180, 240, and 300 W) at 100 kHz for 5 min at 20°C. Also, the intensity of free radical spin adducts in model wine increases with the increase of the system temperature from 20 to 50°C at 100 kHz and 120 W for 5 min, then followed by a decrease at 60°C.[58] Consequently, OH radicals can be formed in aqueous solution under the sonication, while more OH radicals yields with medium–high frequency sonication.

It can be speculated that rich OH radicals were produced at 500 kHz and 207 W at 20°C in this study, however, the formed OH radicals should be immediately scavenged by ethanol in the reaction system. In 1983, Makino et al. found that alcohol, including methanol, ethanol, and butanol, in the aqueous solutions can effectively trap the radicals formed by the sonication (50 kHz and 60 mW/cm^2) by measuring the signal intensities of the spin adduct OH–DMPO.[59] It may be the reason that radicals do not play a role in the sonochemical synthesis of SSNs with medium–high frequencies. On the other hand, it is known that n-butanol is an efficient OH radical scavenger in aqueous sonolysis, and adding n-butanol can confirm the OH radical-mediated reaction mechanism at the interface of the cavitation bubbles.[60-62] If the radicals play the role to a contain extent in the sonochemical synthesis of SSNs, the size and yield of SSNs should be strongly influenced in the presence of n-butanol due to the free radical scavenging effect. As listed in Table 2.2, the dominance of the radical mechanism was not observed in the sonochemical synthesis of SSNs.

2.3.7 Characterization of SSNs

2.3.7.1 FESEM image and SSN size

Fig. 2.8 shows the FESEM images and size distributions of SSNs obtained under optimal sonication conditions with different ultrasonic frequencies.
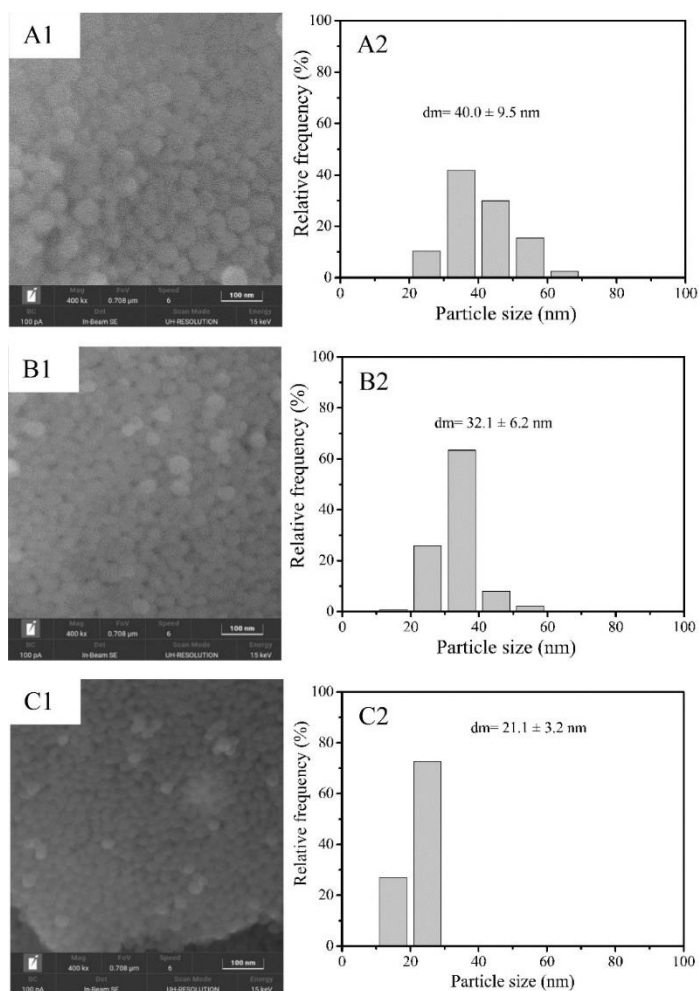
Fig. 2.8 FESEM images of the smallest SSNs obtained with sonication at (A1) 80 kHz, 63 W; (B1) 120 kHz, 78 W; and (C1) 500 kHz 207 W, and the particles size distribution of SSNs obtained with sonication at (A2) 80 kHz, 63 W; (B2) 120 kHz, 78 W; and (C2) 500 kHz, 207 W. Other conditions: ca. 10 mL of the mixture (99.8% ethanol: 6.00 mL, 8.1% NH₄OH: 0.40 mL, 98.0% TEOS: 0.25 mL, H₂O: 3.00 mL) was sonicated for 20 min at 20°C in 3 L of water bath.

As shown in Fig. 2.8, all the SSNs obtained under the medium–high frequency sonication exhibited spherical form and uniform distribution. The smallest average SSNs reached 40, 32, and 21 nm under the optimal sonication conditions with 80, 120, and 500 kHz, respectively, and there the corresponding highest ultrasonic powers (63, 78, 207 W) were applied with various ultrasonic reactors.

It is noteworthy that the SSNs are directly dispersed in water after centrifugation without drying for the QELS analysis, whereas the SSNs are dried and dehydrated for the FESEM measurement. The rich Si–OH groups on the silica surface adsorb water molecules during the QELS measurement, leading to larger hydrodynamic diameters. In contrast, the SSN size decreases during the drying process. Therefore, SSN size detected with FESEM is smaller than the one detected with QELS.

2.3.7.2 FT–IR spectra of SSNs

FT–IR spectrum of the smallest SSNs obtained by sonication at 80 kHz, 120 kHz, and 500 kHz were shown in Fig. 2.9.
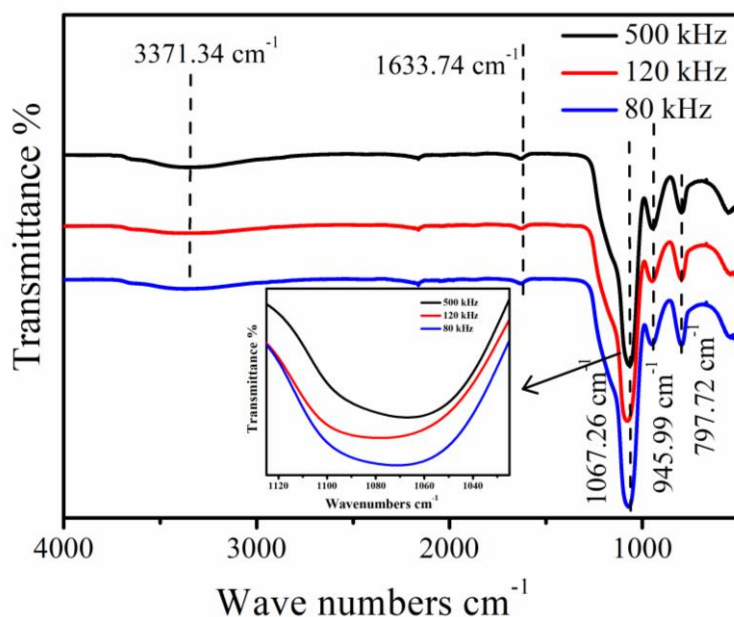
Fig. 2.9 FT–IR spectrum of the smallest SSNs obtained by sonication at 80 kHz, 120 kHz, and 500 kHz. Sonication conditions: ca. 10 mL of the mixture (99.8% ethanol: 6.00 mL, 8.1% NH₄OH: 0.40 mL, 98.0% TEOS: 0.25 mL, H₂O: 3.00 mL) was sonicated for 20 min at 20°C in 3 L of water bath.

The absorption band at 3371 cm^{-1} could be attributed to the stretching vibrations of the Si–OH groups in the SSNs structure.[63] The strong and broadband at 1067 cm^{-1} was assigned to Si–O–Si asymmetric stretching vibration and the absorption band at 798 cm^{-1} could be classified as Si–O–Si symmetric stretching vibration, therefore, the SSNs network structure was formed with condensation reaction.[63, 64] In addition, 946 cm^{-1} can be attributed to the silanol group.[63, 64] The band position of the silica sample at 1634 cm^{-1} was attributed to the bending vibration of the H_2O 0.81 molecule in the Si–OH group.[65] The band position at 1067 cm^{-1} was slightly shifted to a lower wavenumber, due to the decreasing SSN size.[66]

2.3.7.3 XRD pattern of SSNs

To demonstrate the physical structure nature of SSNs, the sample synthesized by 500 kHz sonication was chosen for XRD analysis. Fig. 2.10 shows the XRD pattern of SSNs, which exhibits a broad and strong peak at 2θ = 23.43° without impurity peaks, indicating the amorphous nature of SSNs.
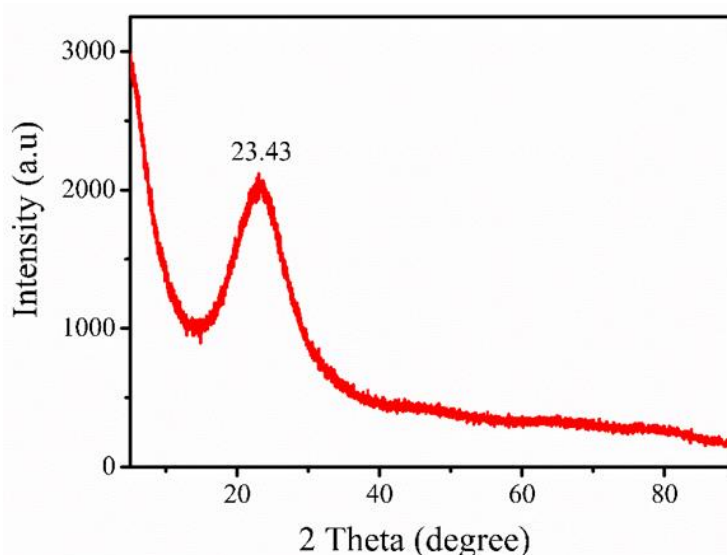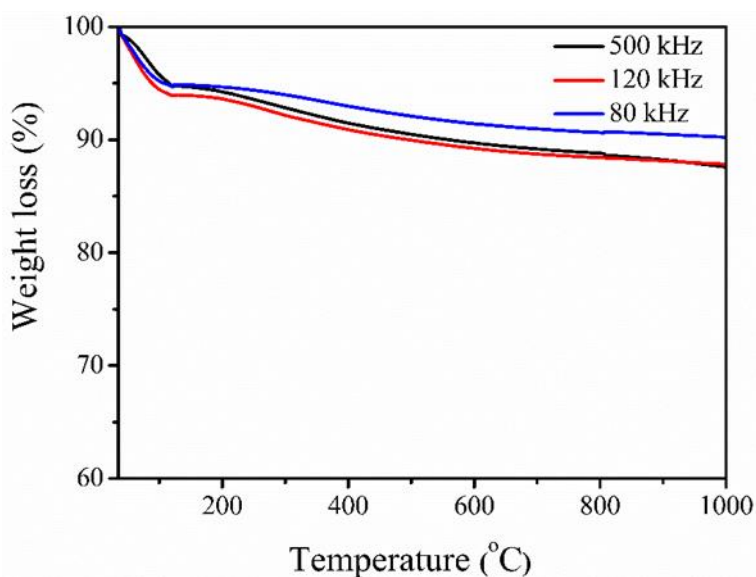

Fig. 2.10 XRD pattern of SSNs. Sonication conditions: ca.10 mL of mixture (99.8% ethanol: 6.00 mL, 8.1% NH₄OH: 0.40 mL, 98.0% TEOS: 0.25 mL, H₂O: 3.00 mL) was sonicated at 500 kHz and 207 W for 20 min at 20°C in 3 L of water bath.

2.3.7.4 TGA of SSNs

Fig. 2.11 shows the TGA profiles of the smallest SSNs obtained by sonication at 80 kHz, 120 kHz, and 500 kHz. It can be seen that the weights of SSNs were lost by about 5.3 wt% (500 kHz), 6.1 wt% (120 kHz), and 5.2 wt% (80 kHz) at low temperatures (<120°C) owing to the removal of absorbed water on SSNs surface. From 120 to 1000°C, about 7.4 wt% (500 kHz), 6.1 wt% (120 kHz), and 4.6 wt% (80 kHz) weight loss of SSNs were attributed to Si–OH dehydration of SSNs. Furthermore, more weight of smaller SSNs was lost than that of larger SSNs due to the difference in silanols of SSNs.

Fig. 2.11 **TGA curves of the smallest SSNs obtained by sonication at 80 kHz, 120 kHz, and 500 kHz. Sonication conditions: ca. 10 mL of the mixture (99.8% ethanol: 6.00 mL, 8.1% NH₄OH: 0.40 mL, 98.0% TEOS: 0.25 mL, H₂O: 3.00 mL) was sonicated for 20 min at 20°C in 3 L of water bath.**

2.4 Conclusions

In summary, the size of synthesized SSNs can be controlled by medium–high frequency sonication. Ultrasonic frequency, power, and temperature significantly affect SSN size and yield. SSN size decreased with increasing ultrasonic power at various frequencies (80, 120, and 500 kHz). Hydrodynamic diameters of 63–117 nm of SSNs were obtained under sonication with 80, 120, and 500 kHz. Moreover, the SSNs obtained were smaller at 120 kHz than at 80 kHz in a multi–frequencies ultrasonic reactor, and the SSN size decreased with increasing ultrasonic power at 20°C. With another 500 kHz ultrasonic bath, the optimal system temperature for producing smaller SSNs was proven to be 20°C. Also, the SSN size decreased with increasing ultrasonic power. The smallest SSNs (63 nm, hydrodynamic diameter by QELS, or 21 nm by FESEM) were obtained by sonication at 207 W for 20 min at 20°C.

The number of active sites or microbubbles increased with the increasing ultrasonic frequency and power, thus TEOS and ammonia were more evenly distributed around the active site, resulting in smaller SSNs. SSN–synthesis scale–up is feasible in the same ultrasonic reactor, while the synthesis efficiency slightly fluctuates over the 50–200 mL range. Similarly, the larger number of microbubbles were generated with increasing temperature from 15 to 20°C resulted in smaller SSNs and lower yields. Particle size increased with the sonication time due to the increasing deposition thickness on the SSNs by unceasing hydrolysis and condensation with time. Moreover, the proportions of both ammonia and ethanol are critical factors for SSN formation even under sonication, and that the active radicals generated during sonication may not be involved in the process. Compared with the traditional Stöber or low–frequency–sonication methods, medium–high frequency sonication can significantly reduce reaction time and reagent amounts with a low molar ratio of $NH_4OH/TEOS$ (0.84).

References

[1] F. Torney, B.G. Trewyn, V.S.-Y. Lin, K. Wang, Mesoporous silica nanoparticles deliver DNA and chemicals into plants, Nature Nanotechnology, 2 (2007) 295-300.

[2] M. Alqasaimeh, L.Y. Heng, M. Ahmad, A.S. Raj, T.L. Ling, A large response range reflectometric urea biosensor made from silica-gel nanoparticles, Sensors, 14 (2014) 13186-13209.

[3] S.E. Kim, L. Zhang, K. Ma, M. Riegman, F. Chen, I. Ingold, M. Conrad, M.Z. Turker, M. Gao, X. Jiang, Ultrasmall nanoparticles induce ferroptosis in nutrient-deprived cancer cells and suppress tumour growth, Nature Nanotechnology, 11 (2016) 977-985.

[4] W. Stöber, A. Fink, E. Bohn, Controlled growth of monodisperse silica spheres in the micron size range, Journal of Colloid and Interface Science, 26 (1968) 62-69.

[5] G. Bogush, M. Tracy, C. Zukoski Iv, Preparation of monodisperse silica particles: control of size and mass fraction, Journal of Non-crystalline Solids, 104 (1988) 95-106.

[6] I.A. Ibrahim, A. Zikry, M.A. Sharaf, Preparation of spherical silica nanoparticles: Stober silica, Journal of American Science, 6 (2010) 985-989.

[7] X.-D. Wang, Z.-X. Shen, T. Sang, X.-B. Cheng, M.-F. Li, L.-Y. Chen, Z.-S. Wang, Preparation of spherical silica particles by Stöber process with high concentration of tetra-ethyl-orthosilicate, Journal of Colloid and Interface Science, 341 (2010) 23-29.

[8] A. Gedanken, Using sonochemistry for the fabrication of nanomaterials, Ultrasonics Sonochemistry, 11 (2004) 47-55.

[9] N.A. Dhas, K.S. Suslick, Sonochemical preparation of hollow nanospheres and hollow nanocrystals, Journal of the American Chemical Society, 127 (2005) 2368-2369.

[10] H. Xu, B.W. Zeiger, K.S. Suslick, Sonochemical synthesis of nanomaterials, Chemical Society Reviews, 42 (2013) 2555-2567.

[11] X. Liu, Z. Wu, R. Cavalli, G. Cravotto, Sonochemical preparation of inorganic nanoparticles and nanocomposites for drug release–A review, Industrial & Engineering Chemistry Research, 60 (2021) 10011-10032.

[12] K.S. Suslick, Sonochemistry, Science, 247 (1990) 1439-1445.

[13] K.S. Suslick, G.J. Price, Applications of ultrasound to materials chemistry, Annual Review of Materials Science, 29 (1999) 295-326.

[14] S.L. Hem, The effect of ultrasonic vibrations on crystallization processes, Ultrasonics, 5 (1967) 202-207.

[15] X. Zhang, T. Inada, A. Tezuka, Ultrasonic-induced nucleation of ice in water containing air bubbles, Ultrasonics Sonochemistry, 10 (2003) 71-76.

[16] C. Virone, H. Kramer, G. Van Rosmalen, A. Stoop, T. Bakker, Primary nucleation induced by ultrasonic cavitation, Journal of Crystal Growth, 294 (2006) 9-15.

[17] P. Kanthale, M. Ashokkumar, F. Grieser, Sonoluminescence, sonochemistry (H_2O_2 yield) and bubble dynamics: frequency and power effects, Ultrasonics Sonochemistry, 15 (2008) 143-150.

[18] M. Ashokkumar, J. Lee, Y. Iida, K. Yasui, T. Kozuka, T. Tuziuti, A. Towata, Spatial distribution of acoustic cavitation bubbles at different ultrasound frequencies, ChemPhysChem, 11 (2010) 1680-1684.

[19] J. Lee, M. Ashokkumar, S. Kentish, F. Grieser, Determination of the size distribution of sonoluminescence bubbles in a pulsed acoustic field, Journal of the American Chemical Society, 127 (2005) 16810-16811.

[20] A. Brotchie, F. Grieser, M. Ashokkumar, Effect of power and frequency on bubble-size distributions in acoustic cavitation, Physical Review Letters, 102 (2009) 084302.

[21] S. Merouani, O. Hamdaoui, Y. Rezgui, M. Guemini, Effects of ultrasound frequency and acoustic amplitude on the size of sonochemically active bubbles–theoretical study, Ultrasonics Sonochemistry, 20 (2013) 815-819.

[22] A. Inui, A. Honda, S. Yamanaka, T. Ikeno, K. Yamamoto, Effect of ultrasonic frequency and surfactant addition on microcapsule destruction, Ultrasonics Sonochemistry, 70 (2021) 105308.

[23] K. Yasui, Numerical simulations for sonochemistry, Ultrasonics Sonochemistry, 78 (2021) 105728.

[24] N. Enomoto, T. Koyano, Z.-e. Nakagawa, Effect of ultrasound on synthesis of spherical silica, Ultrasonics Sonochemistry, 3 (1996) S105-S109.

[25] Z.-T. Lin, Y.-B. Wu, Y.-G. Bi, Rapid synthesis of SiO_2 by ultrasonic-assisted Stober method as controlled and pH-sensitive drug delivery, Journal of Nanoparticle Research, 20 (2018) 1-13.

[26] R. Kamila, M. Akhir, A. Patriati, A. Insani, Synthesis of silica particles through conventional sol-gel and sonochemistry methods and the effect of catalyst, water concentration and sample environment to the particle size, in: Journal of Physics: Conference Series, IOP Publishing, 2022, pp. 012044.

[27] I. Rahman, P. Vejayakumaran, C. Sipaut, J. Ismail, M.A. Bakar, R. Adnan, C. Chee, An optimized sol–gel synthesis of stable primary equivalent silica particles, Colloids and Surfaces A: Physicochemical and Engineering Aspects, 294 (2007) 102-110.

[28] H. Yao, J.-M. Hong, N. Li, S. Xu, J.-J. Zhu, Homogenous thionine-SiO_2 nanocomposite spheres: sonochemical preparation, characterization, and application in H_2O_2 biosensor, Journal of Nanoscience and Nanotechnology, 9 (2009) 2421-2425.

[29] Q. Guo, D. Huang, X. Kou, W. Cao, L. Li, L. Ge, J. Li, Synthesis of disperse amorphous SiO_2 nanoparticles via sol–gel process, Ceramics International, 43 (2017) 192-196.

[30] Z.L. Wu, J. Lifka, B. Ondruschka, Comparison of energy efficiency of various ultrasonic devices in aquasonochemical reactions, Chemical Engineering & Technology: Industrial Chemistry - Plant Equipment - Process Engineering - Biotechnology, 29 (2006) 610-615.

[31] R.F. Contamine, A. Wilhelm, J. Berlan, H. Delmas, Power measurement in sonochemistry, Ultrasonics Sonochemistry, 2 (1995) S43-S47.

[32] H. Tang, Y. Zhao, J.Z. Zhang, Y. Sha, L.G. Jin, Process research of amorphous SiO_2 for optical fiber preform by sol-gel, in: Advanced Materials Research, Trans Tech Publ, 2011, pp. 368-371.

[33] Z. Wu, B. Ondruschka, Roles of hydrophobicity and volatility of organic substrates on sonolytic kinetics in aqueous solutions, The Journal of Physical Chemistry A, 109 (2005) 6521-6526.

[34] H.-M. Kim, C.-H. Lee, B. Kim, Sonochemical synthesis of silica particles and their size control, Applied Surface Science, 380 (2016) 305-308.

[35] L. Cheng, J. Cai, Y. Ke, Ultrasonic-assisted sol–gel synthesis of core–shell silica particles for high-performance liquid chromatography, Journal of Inorganic and Organometallic Polymers and Materials, 30 (2020) 859-868.

[36] M. Gutierrez, A. Henglein, Chemical action of pulsed ultrasound: observation of an unprecedented intensity effect, Journal of Physical Chemistry, 94 (1990) 3625-3628.

[37] S. Merouani, O. Hamdaoui, The size of active bubbles for the production of hydrogen in sonochemical reaction field, Ultrasonics Sonochemistry, 32 (2016) 320-327.

[38] K. Yasui, Influence of ultrasonic frequency on multibubble sonoluminescence, The Journal of the Acoustical Society of America, 112 (2002) 1405-1413.

[39] F. Burdin, N. Tsochatzidis, P. Guiraud, A. Wilhelm, H. Delmas, Characterisation of the acoustic cavitation cloud by two laser techniques, Ultrasonics Sonochemistry, 6 (1999) 43-51.

[40] M. Ehsani, N. Zhu, H. Doan, A. Lohi, A. Abdelrasoul, In-situ synchrotron X-ray imaging of ultrasound (US)-generated bubbles: Influence of US frequency on microbubble cavitation for membrane fouling remediation, Ultrasonics Sonochemistry, 77 (2021) 105697.

[41] R. Pflieger, A.A. Ndiaye, T. Chave, S.I. Nikitenko, Influence of ultrasonic frequency on Swan band sonoluminescence and sonochemical activity in aqueous tert-butyl alcohol solutions, The Journal of Physical Chemistry B, 119 (2015) 284-290.

[42] S. Merouani, H. Ferkous, O. Hamdaoui, Y. Rezgui, M. Guemini, A method for predicting the number of active bubbles in sonochemical reactors, Ultrasonics Sonochemistry, 22 (2015) 51-58.

[43] A. Dehane, S. Merouani, O. Hamdaoui, Effect of carbon tetrachloride (CCl_4) sonochemistry on the size of active bubbles for the production of reactive oxygen and chlorine species in acoustic cavitation field, Chemical Engineering Journal, 426 (2021) 130251.

[44] C. Pétrier, A. Francony, Ultrasonic waste-water treatment: incidence of ultrasonic frequency on the rate of phenol and carbon tetrachloride degradation, Ultrasonics Sonochemistry, 4 (1997) 295-300.

[45] Y. Jiang, C. Petrier, T.D. Waite, Sonolysis of 4-chlorophenol in aqueous solution: effects of substrate concentration, aqueous temperature and ultrasonic frequency, Ultrasonics Sonochemistry, 13 (2006) 415-422.

[46] S. Merouani, O. Hamdaoui, F. Saoudi, M. Chiha, Influence of experimental parameters on sonochemistry dosimetries: KI oxidation, Fricke reaction and H_2O_2 production, Journal of Hazardous Materials, 178 (2010) 1007-1014.

[47] H. Mulvana, E. Stride, J.V. Hajnal, R.J. Eckersley, Temperature dependent behavior of ultrasound contrast agents, Ultrasound in Medicine & Biology, 36 (2010) 925-934.

[48] S.K. Park, K. Do Kim, H.T. Kim, Preparation of silica nanoparticles: determination of the optimal synthesis conditions for small and uniform particles, Colloids and Surfaces A: Physicochemical and Engineering Aspects, 197 (2002) 7-17.

[49] F. Grieser, R. Hobson, J. Sostaric, P. Mulvaney, Sonochemical reduction processes in aqueous colloidal systems, Ultrasonics, 34 (1996) 547-550.

[50] M.R. Hoffmann, I. Hua, R. Höchemer, Application of ultrasonic irradiation for the degradation of chemical contaminants in water, Ultrasonics Sonochemistry, 3 (1996) S163-S172.

[51] Z. Wu, G. Cravotto, M. Adrians, B. Ondruschka, W. Li, Critical factors in sonochemical degradation of fumaric acid, Ultrasonics Sonochemistry, 27 (2015) 148-152.

[52] C. Petrier, A. Francony, Incidence of wave-frequency on the reaction rates during ultrasonic wastewater treatment, Water Science and Technology, 35 (1997) 175-180.

[53] M. Topaz, M. Motiei, A. Gedanken, D. Meyerstein, N. Meyerstein, EPR analysis of radicals generated in ultrasound-assisted lipoplasty simulated environment, Ultrasound in Medicine & Biology, 27 (2001) 851-859.

[54] M. Topaz, M. Motiei, E. Assia, D. Meyerstein, N. Meyerstein, A. Gedanken, Acoustic cavitation in phacoemulsification: chemical effects, modes of action and cavitation index, Ultrasound in Medicine & Biology, 28 (2002) 775-784.

[55] M. Kubo, K. Sekiguchi, N. Shibasaki-Kitakawa, T. Yonemoto, Kinetic model for formation of DMPO-OH in water under ultrasonic irradiation using EPR spin trapping method, Research on Chemical Intermediates, 38 (2012) 2191-2204.

[56] Z. Wei, F.A. Villamena, L.K. Weavers, Kinetics and mechanism of ultrasonic activation of persulfate: an in situ EPR spin trapping study, Environmental Science & Technology, 51 (2017) 3410-3417.

[57] A. Režek Jambrak, S. Ojha, D. Šeremet, M. Nutrizio, N. Maltar - Strmečki, S. Valić, J. Gajdoš Kljusurić, B. Tiwari, Free radical detection in water after processing by means of high voltage electrical discharges and high power ultrasound, Journal of Food Processing and Preservation, 45 (2021) e15176.

[58] Q.-A. Zhang, Y. Shen, X.-H. Fan, J.F.G. Martín, X. Wang, Y. Song, Free radical generation induced by ultrasound in red wine and model wine: An EPR spin-trapping study, Ultrasonics Sonochemistry, 27 (2015) 96-101.

[59] K. Makino, M.M. Mossoba, P. Riesz, Chemical effects of ultrasound on aqueous solutions. Formation of hydroxyl radicals and hydrogen atoms, The Journal of Physical Chemistry, 87 (1983) 1369-1377.

[60] M.V. Bagal, P.R. Gogate, Sonochemical degradation of alachlor in the presence of process intensifying additives, Separation and Purification Technology, 90 (2012) 92-100.

[61] N.B. Bokhale, S.D. Bomble, R.R. Dalbhanjan, D.D. Mahale, S.P. Hinge, B.S. Banerjee, A.V. Mohod, P.R. Gogate, Sonocatalytic and sonophotocatalytic degradation of rhodamine 6G containing wastewaters, Ultrasonics Sonochemistry, 21 (2014) 1797-1804.

[62] A.M. Lastre-Acosta, G. Cruz-González, L. Nuevas-Paz, U.J. Jáuregui-Haza, A.C.S.C. Teixeira, Ultrasonic degradation of sulfadiazine in aqueous solutions, Environmental Science and Pollution Research, 22 (2015) 918-925.

[63] S. Musić, N. Filipović-Vinceković, L. Sekovanić, Precipitation of amorphous SiO_2 particles and their properties, Brazilian Journal of Chemical Engineering, 28 (2011) 89-94.

[64] J.M. Kim, S.M. Chang, S.M. Kong, K.-S. Kim, J. Kim, W.-S. Kim, Control of hydroxyl group content in silica particle synthesized by the sol-precipitation process, Ceramics International, 35 (2009) 1015-1019.

[65] P. Nayak, A. Datta, Synthesis of SiO_2-nanoparticles from rice husk ash and its comparison with commercial amorphous silica through material characterization, Silicon, 13 (2021) 1209-1214.

[66] L. Singh, S. Agarwal, S. Bhattacharyya, U. Sharma, S. Ahalawat, Preparation of silica nanoparticles and its beneficial role in cementitious materials, Nanomaterials and Nanotechnology, 1 (2011) 9.

Chapter 3: Ultrasonic Preparation of Hollow Mesoporous Silica Nanoparticles for Controlled Release of Voriconazole

Abstract

Hollow mesoporous silica nanoparticles (HMSNs) were synthesized by double-template method with SSNs as the hard template and hexadecyl trimethyl ammonium bromide (CTAB) as the soft template. The mesoporous silica with core-shell structure was prepared by 500 kHz sonication. To reduce the reaction time, ultrasound was used to remove the SSNs core and a microwave was used to remove the soft template of CTAB to obtain HMSNs. The effects of ultrasonic frequency, ultrasonic power, ultrasonic time, ultrasonic volume, and bulk temperature on etching were investigated. The effect of ultrasonic frequency on the etching of silica nano-cores was not significant. At 40kHz, the etching efficiency increased with the increasing of ultrasonic power. At 40 kHz, the SSN cores were completely etched by sonication for 30 min, while it took only 10 min at 19.5 kHz. Ultrasonic temperature, however, had a significant effect on the etching of SSN cores. The optimum etching temperature was 50°C. In addition, the effects of microwave treatment time and temperature on the CTAB removal were studied. The results show that CTAB can be completely removed at 80°C for 5 min. Finally, the drug loading and release characteristics of HMSNs were studied by using the antifungal drug voriconazole (VOR) as a model drug. The loading efficiency (wt%) of VOR on the HMSNs was 9.63%, and the total VOR release amount of VOR-HMSNs material was 65.1% at 36 h. The Korsmeyer-Peppas and Higuchi kinetic model confirmed that the release mechanism of HMSNs nanoparticles followed Fickian diffusion at pH 7.4 and 37°C. At pH 5.8, the cumulative release amount of VOR from the VOR-HMSNs material was similar at pH 7.4. A Korsmeyer-Peppas kinetic model shows that the VOR molecules pass through the pore of the silica shell with Fickian diffusion mechanism at pH 5.8.

3.1   Introduction

Hollow nanostructured materials are widely used as a functional material, due to their unique large cavities, intact shells, and uniform morphologies.[1] Among the abundant materials of the hollow nanostructure, hollow mesoporous silica nanoparticles (HMSNs) have attracted extensive attention due to their excellent

capability for carrying active molecules. Firstly, compared with conventional porous nano-silica, HMSNs establish a significantly high drug loading capacity thanks to the hollow centric cavity.[2, 3] Secondly, HMSNs have controllable particle size and porosity, high chemical stability, and available surface modification.[4, 5] The synthesis of HMSNs is performed using a variety of methods. The most efficient method is a dual-template system, usually using a hard template to create the interior hollow structure and a surfactant to create the mesoporous shell.[6-8] Various hard templates have been used, and their sizes of hollow cavity can be controlled precisely by altering the particle sizes of the templates.[9] However, the removal of hard templates is both time-consuming and uneconomical.[2, 10, 11] Compared with hard templates, soft templates can able to directly construct HMSNs by self-assembly. However, the hollow sizes of HMSNs are not uniform, and serious aggregation of HMSNs occurs.[12]

Generally, HMSNs are prepared with a dual template (a hard template and a soft template). Mesoporous silica shells are generated on hard templates using soft templates as pore precursors.[13] Their hollow structure is formed by removing the hard template with a selective etching method. The soft template is removed by solvent extraction to generate mesoporous channels. The selective etching method is based on the difference in the etching rate of SiO_2 layers due to different structures.[13] Compared to a dense SiO_2 shell, a SiO_2 core is more easily etched. Therefore, in multi-layer SiO_2 materials with different structures, selective etching provides the possibility to form a hollow structure.[14] The surfactant in the channel is extracted by reflux extraction in an organic solvent.[2, 10]

For example, Liu et al. reported that 0.47 g of Na_2CO_3 were added to 20 mL of SiO_2@CTAB-SiO_2 dispersion and stirred at 50°C for 10 h to remove the SiO_2 core.[2] The crude product was suspended in a mixture of methanol/HCl (50 mL/3 mL) and refluxed at 80°C for 24 h. HMSNs were obtained by centrifugation. Similarly, Sun et al. also reported that 1.2 g of Na_2CO_3 were added to the 60 mL of sSiO_2@SiO_2 suspension and stirred at 50°C for 12 h to etch SiO_2 core. HMSNs precursor were collected by centrifugation.[10] Finally, 1.0 g of the product and 5.0 mL of concentrated hydrochloric acid were added to 100 mL of ethanol and followed by reflux for 12 h to remove the surfactant of CTAB. HMSNs were collected by

centrifugation. Apparently, a long time is required to remove the soft and hard templates by using the above convention method to prepare HMSNs.

Voriconazole (VOR) is a second-generation azole antifungal drug with broad-spectrum activity.[15] VOR is commonly used to treat fungal infections, including invasive aspergillosis, esophageal candidiasis, and severe fungal infections.[16] VOR is used in clinical as an oral tablet dosage form and solution for intravenous injection.[16-19] These delivery systems are associated with several side effects such as nausea, vomiting, diarrhea, headache, fever, swelling in hands, ankles, or feet, loss of appetite, tiredness, visual disturbances, elevated hepatic enzyme levels, and abdominal pain.[17-19] Apart from side effects, the drug has poor water solubility and it is prone to high first-pass metabolism.[19] Topical delivery has received enormous attention to overcome these limitations. Therefore, to overcome the limitations of conventional drug delivery, the nanocarrier-based system is an alternative strategy to increase drug permeability through the skin.[17-19]

Ultrasonic-assisted and microwave-assisted methods were used to shorten the time to remove hard and soft templates. Mesoporous silica materials with core-shell structures were prepared by the ultrasonic-assisted method. Then the effects of ultrasonic frequency, ultrasonic power, ultrasonic time, and ultrasonic temperature on etching were explored respectively. In addition, a microwave-assisted method was used to remove the surfactant of CTAB. The effects of microwave treatment time and temperature on the removal of surfactant were studied respectively. Finally, the as-prepared material was used for the loading and release of VOR.

3.2   Material and methods

3.2.1 Materials

Tetraethyl orthosilicate (TEOS, 98.0%, Aldrich), ethanol (≥99.8%, Sigma-Aldrich), NH$_4$OH (30.0%, Carlo Erba), CTAB (＞98.0%, Tokyo Chemical Industry Co., Ltd.), Na$_2$CO$_3$·H$_2$O (≥99.5%, Sigma-Aldrich), HCl (36% w/w, Alfa Aesar) Sodium

hydroxide (97%, Thermo Scientific), VOR (≥98% (HPLC), Sigma), potassium hydrogen phosphate (98%, Alfa Aesar) and Potassium dihydrogen phosphate (98%, Alfa Aesar) were used without additional purification.

3.2.2 Methods

Ultrasonic cup-horn apparatus (home-made, 19.5 kHz); 40, 80, and 120 kHz sonic digital cleaning (MG 200, Weber Ultrasonics, Germany); 500 kHz ultrasonic micro cleaning (UMC-Premium, Weber Ultrasonics, Germany); Magnetic stirrer (AREX VELP Scientifica, Italy). Microwave Reaction System (Multiwave 5000, Anton Paar); Centrifuge (Allegra 64R Benchtop Centrifuge, Beckman Coulter, Italy); Ultraviolet-visible Spectrophotometer (UV, Agilent Technologies Cary 60 UV-Vis, USA). The ultrasonic powers delivered were determined calorimetrically with water as heating media and all ultrasonic power mentioned below refers to the power measured calorimetrically.[20]

3.2.2.1 Synthesis of SSNs

SSNs were synthesized using previously reported methods.[21] A high-frequency device (500 kHz) consists of an ultrasonic cleaning generator (maximum electrical output power: 250 W) and a 5.6-L ultrasonic bath (28 cm×20 cm×10 cm) with cooling water serpentine at 1 cm from the bottom (UMC, Weber Ultrasonics, Germany) were used to synthesize SSNs.

In a 5.6-L ultrasonic bath, 3 L of water was used as the ultrasonic medium. First, degassing was performed for 20 min with sonication, and cooling water was used to keep the temperature of the ultrasonic bath at 20 ± 0.3°C. 60.0 mL of 99.8% ethanol, 30.0 mL H_2O, and 2.5 mL of TEOS were added to a 1000-mL volumetric flask reactor in turn. Subsequently, 4.0 mL of 8.1% NH_4OH as a catalyst was added to the above mixture (molar ratio: 99.8% ethanol/8.1% NH_4OH/TEOS/H_2O = 92.92/0.84/1.00/150.89). Then, the mixture solution was sonicated with 500 kHz and 207 W for 60 min at 20°C. A centrifuge was used to collect the prepared SSNs from reaction systems and washing liquids. The SSNs were collected with the centrifuge (20,000 rpm, 15 min) and washed twice with ethanol and then washed once with distilled water.

3.2.2.2   Synthesis of SSN@mesoporous silica (SSN@mSiO₂)

The dispersion solution of SSNs (ca. 0.1 g) in water (40 mL) was added to a mixture solution of CTAB (0.15 g) in ethanol (60 mL) and water (60 mL), and then 0.1 mL of ammonia solution was added. Subsequently, the above-mixed solution was sonicated with 500 kHz and 207 W at $20 \pm 0.3°C$. After 10 min, 0.28 mL of TEOS was added, and continued to sonicate for 60 min. The prepared $SSNs@mSiO_2$ was collected by centrifugation at 15,000 rpm for 20 min, and then washed twice with ethanol and once with water. The obtained $SSNs@mSiO_2$ were dispersed in an aqueous solution (40 mL) for further processing.

3.2.2.3   Removing the SSNs core

0.744 g of $Na_2CO_3·H_2O$ were dissolved in $SSNs@mSiO_2$ dispersion solution and sonicated with different frequencies, powers, times, and temperatures. The prepared HMSNs were collected by centrifugation at 15,000 rpm for 20 min, and then washed twice with ethanol and once with water. The obtained HMSNs were dispersed in ethanol (10 mL) for further processing.

3.2.2.4   Removing the CTAB

To remove the surfactant, 1 mL of HCl was added to the above 10 mL of HMSNs dispersion and treated with microwave radiation at 80, 120, 160, and 190°C. The prepared HMSNs were collected by centrifugation at 15,000 rpm for 20 min, and then washed twice with ethanol and once with water. The obtained HMSNs were dried with freeze-drying.

3.2.3 Characterization

Field emission scanning electron microscope (FESEM) measurements were performed on a Tescan S9000G FESEM 3010 microscope (30 KeV) equipped with a high-brightness Schottky emitter. For analysis, the powder samples were deposited on a stub coated with a conducting adhesive and inserted in the chamber by a fully motorized procedure. The Fourier-transform infrared spectroscopy (FT-IR) spectra (Spectrum Two, PerkinElmer, USA) were measured by a spectrometer from 500 to 4000 cm^{-1} at 2 cm^{-1} resolution with 64 scans.

3.2.4 Adsorption of rhodamine 6G by mesoporous silica nanoparticles (MSNs) and HMSNs

Rhodamine 6G was used as an adsorbent to study the removal effect of the SSN core. 0.1 mM rhodamine 6G solution was obtained with 4.79 g of rhodamine 6G dissolved in 100 mL of distilled water. 4 mg of prepared HMSNs were dispersed in 4 mL of 0.1 mM Rhodamine 6G solution. After 24 h, the above dispersion was centrifuged and then 1 mL of supernatant was pipetted from the centrifuge tube to dilute 4-fold. The absorbance of the solution was measured at 526 nm by using UV. The adsorption capacity of the HMSNs was calculated with equation 3-1.

$$\text{Adsorption capacity} = \frac{(A_i - A_t) \times 0.0479}{A_i} \times 1000 \qquad \text{(3-1)}$$

where A_i is initial absorbance of rhodamine 6G, A_t is termination absorbance of rhodamine 6G.

3.2.5 Drug loading

The standard curve was prepared with distilled water. 10 mg of VOR were added into a 100 mL volumetric flask and distilled water as solvent was diluted to the mark to obtain 100 µg/mL stock solution. 1.5, 2.0, 2.5, 3.0, and 4.0 mL of the above VOR stock solution were placed in 10 mL volumetric flasks, respectively. Distilled water was used to make up the volume. Therefore, 15, 20, 25, 30, and 40 µg/mL of the test solution were obtained. Using distilled water as a blank control, the absorbance A of VOR was measured at a wavelength of 256 nm.

The drug loading of VOR was studied using distilled water as the loading solvent. 20 mg of VOR were dispersed in 50 mL of distilled water by sonication. Then 100 mg of HMSNs was dispersed in the above dispersions with stirring at 200 rpm. After 24 h agitation, the VOR-loaded HMSNs (VOR-HMSNs) were centrifuged at 15,000 rpm for 10 min, and then the precipitate was washed once with distilled water to remove VOR on the surface of VOR-HMSNs. The supernatant was collected and measured by UV spectroscopy. The loading amount of HMSNs to VOR was

calculated by the obtained standard curve. Calculate the loading efficiency (wt%) of the HMSNs using the following equation:[22, 23]

$$\text{Loading efficiency } (\%) = \frac{\text{Mass of drugs in the HMSNs}}{\text{Mass of the drug loaded HMSNs}} \times 100\% \qquad (3\text{-}2)$$

3.2.6 Drug release

The standard curve was prepared with phosphate buffer (PB) solutions. According to the aforementioned method, 10 mg of VOR was solved in (PB) and placed into a 100 mL volumetric flask. A concentration of 100 μg/mL stock solution was obtained with PB injected into the volumetric flask to a constant volume. 1.0, 1.5, 2.0, 2.5, and 3.0 mL of VOR stock solutions were pipetted to 10 mL volumetric flasks. Then, with PB solution to the mark of 10 mL volumetric flasks, 10, 15, 20, 25, and 30 μg/mL of the solution of the test substance were prepared. Using PB solution as the blank control solution, the absorbance A values of the test substances were measured at the maximum absorption wavelength, respectively.

20 mg of VOR-HMSNs were dispersed in 20 mL of PB solution and then the solution was stirred with a constant temperature magnetic stirrer at a speed of 200 r/min. 3 mL of sample was taken out at 5, 10, 20, 30, 45, 60, 120, 180, 240, 480, 1440, and 2160 min respectively, and 3 mL of the fresh PB buffer medium was added immediately after taking out. The take-out samples were used to measure the absorbance A value and then the drug concentration was calculated according to the standard curve of VOR in PB to obtain the cumulative release amount of the VOR.

3.3 Results and discussion

According to previous research, ultrasound (500 kHz, 207 W) was used to prepare mesoporous silica with a core-shell structure.[21] To reduce the reaction time, ultrasound was used to remove the hard template (SSNs core) and a microwave was used to remove the soft template of CTAB to obtain HMSNs. The as-prepared HMSNs were characterized by FESEM. As shown in Fig. 3.1, the HMSNs

obtained under high-frequency sonication (500 kHz and 207 W) exhibited spherical form. The average particle size of HMSNs was about 45.6 nm.
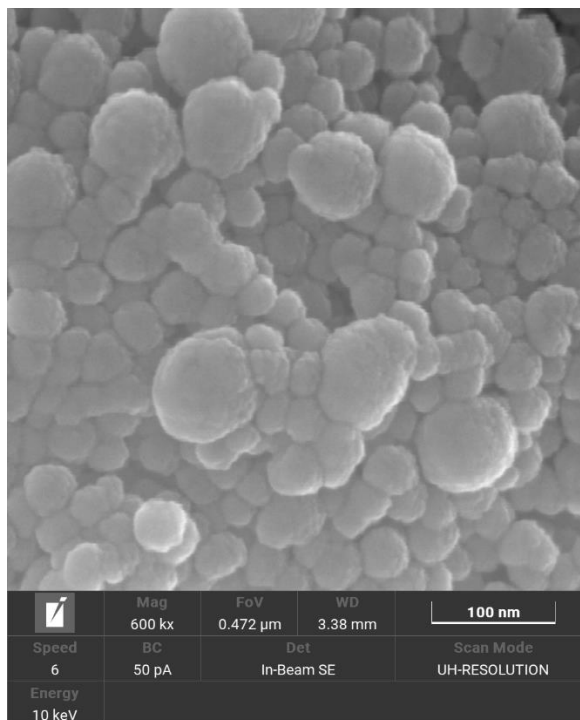

Fig. 3.1 FESEM images of the HMSNs obtained with sonication at 500 kHz and 207 W.

Firstly, the effects of ultrasonic frequency, ultrasonic power, ultrasonic time, ultrasonic volume, and bulk temperature on etching were investigated. During these processes, the optimal microwave heating (80°C, 5 min) was selected for CTAB removal. The adsorption capacity of rhodamine 6G on HMSNs was used to indicate the removal efficiency of SSNs core.

3.3.1 Effect of sonication time

Firstly, the effect of sonication time on the etching of the SSNs core was investigated. Fig. 3.2 shows the rhodamine 6G adsorption capacity on the prepared HMSNs. In Fig. 3.2, the adsorption capacity on HMSNs was significantly higher than that MSNs (mesoporous silica with a core-shell structure). With the ultrasonic

frequency of 19.5 kHz and power of 15.8 W, the rhodamine 6G adsorption on HMSNs increased with ultrasonic time extended from 5 min to 20 min (Fig. 3.3). Similarly, under 40 kHz and 54 W, the adsorption capacity on HMSNs increased with ultrasonic time (Fig. 3.4). Thus, the more SSNs cores were etched with the increase of sonication time. However, compared to 20 min, the adsorption capacity did not change significantly at 19.5 kHz and 40 kHz for 30 min. Therefore, the SSNs cores had been completely removed for 20 min sonication.
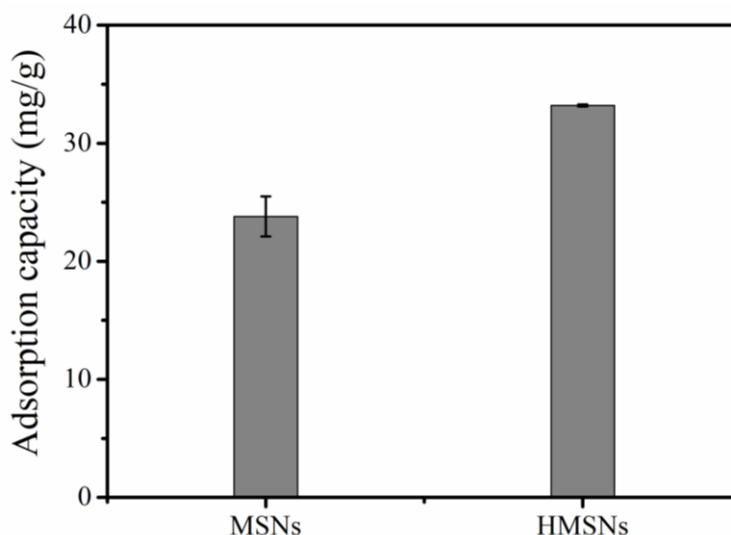
Fig. 3.2 The rhodamine 6G adsorption capacity on the prepared MSNs and HMSNs.
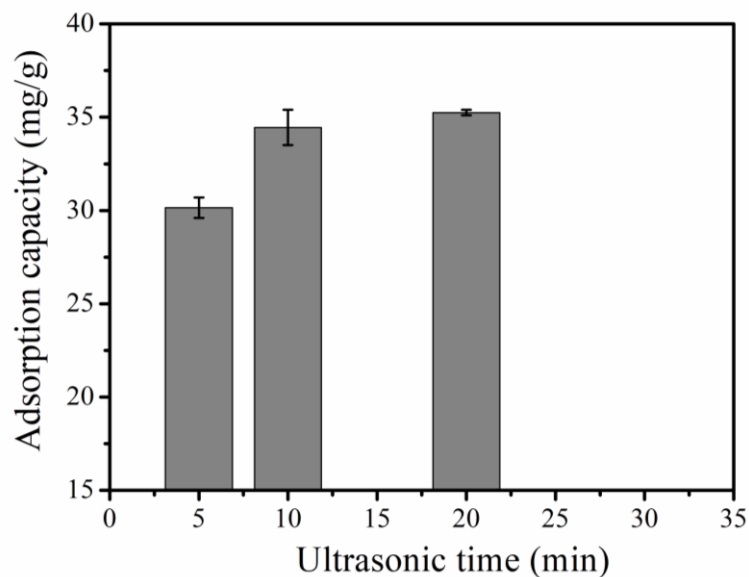
Fig. 3.3 The rhodamine 6G adsorption capacity on the HMSNs at different sonication times under 19.5 kHz, 15.8 W.
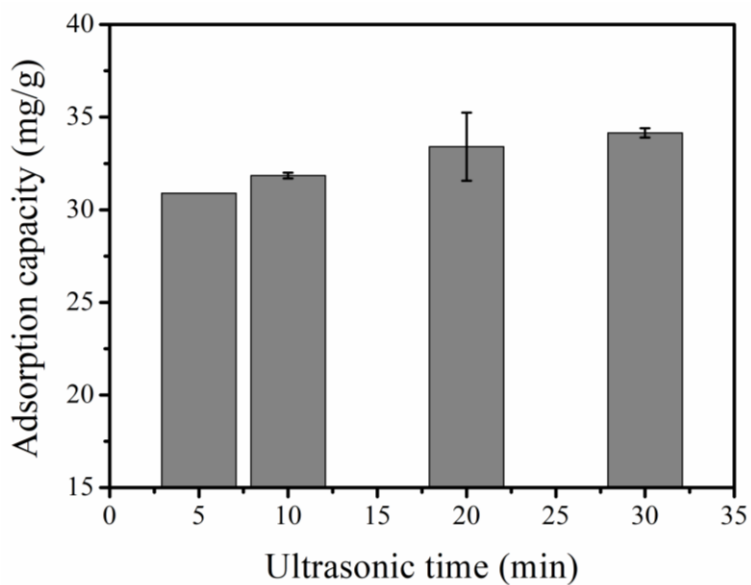
Fig. 3.4 The rhodamine 6G adsorption capacity on the HMSNs at different sonication times under 40 kHz, 54 W.

3.3.2 Effect of ultrasonic frequency

The effect of ultrasonic frequency of 40, 80, and 120 kHz on the etching of the SSNs core was studied under sonication at 54 W for 20 min. In Fig. 3.5, the adsorption capacities on HMSNs are 33.2%, 30.1%, and 31.3% under ultrasonic frequency at 40, 80, and 120 kHz. Consequently, ultrasonic frequencies had no significant effect on the etching of SSNs core.
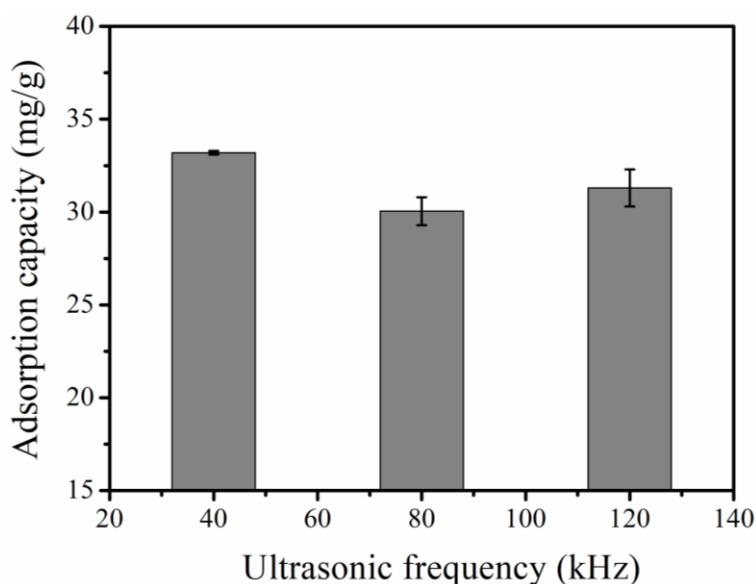
Fig. 3.5 Influence of ultrasonic frequency on the etching of the SSNs core at ca. 54 W for 20 min.

3.3.3 Effect of ultrasonic power

The effect of ultrasonic power on etching was investigated. As can be seen in Fig. 3.6A, the adsorption capacity on HMSNs did not change significantly with the ultrasonic powers from 15.8 to 33.9 W at 19.5 kHz for 20 min. Therefore, the power of 15.8 W is enough to completely etch the SSNs.
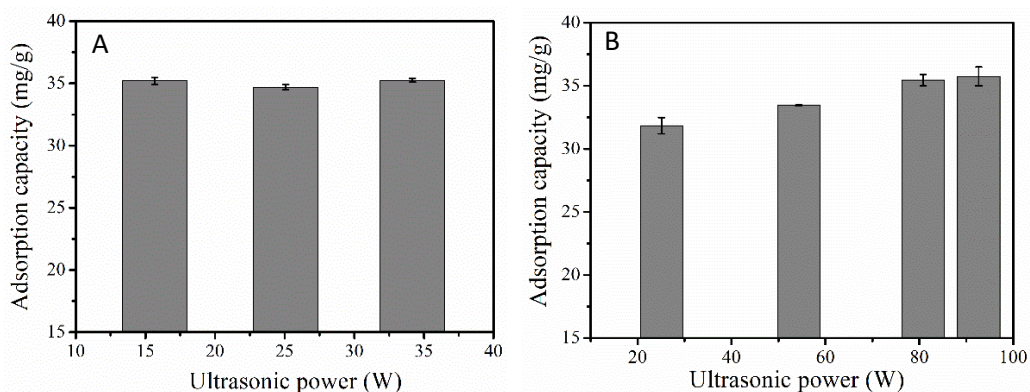
Fig. 3.6 Effects of ultrasonic power on the etching of the SSNs core at 19.5 kHz (A) and 40 kHz (B).

In Fig. 3.6B, the adsorption capacity on HMSNs increased with ultrasonic power from 25.1 to 80.8 W at 40 kHz for 20 min. The more SSNs cores were etched with increasing ultrasonic power. However, the adsorption capacity on HMSNs did not change with the ultrasonic power increasing from 80.8 to 92.7 W. Thus, the SSNs core had been completely removed at 80.8 W for 20 min.

3.3.4 Effect of bulk temperature

At 40 kHz, the effect of bulk temperature on etching was studied at 40, 45, and 50°C, respectively. In Fig. 3.7, the adsorption capacity on HMSNs increased as the bulk temperature increased. The bulk temperature was important to etch SSNs core, and etching must be carried out in a hot alkaline solution. Since OH^- ions can etch the amorphous silica framework by coordinating with Si atoms and subsequently breaking Si-O-Si bonds. Etching in hot alkaline media involves breaking Si-O-Si bonds to form oligomers of silica species, however, chemical reversal can be performed by bond formation between different preformed silicate oligomers.
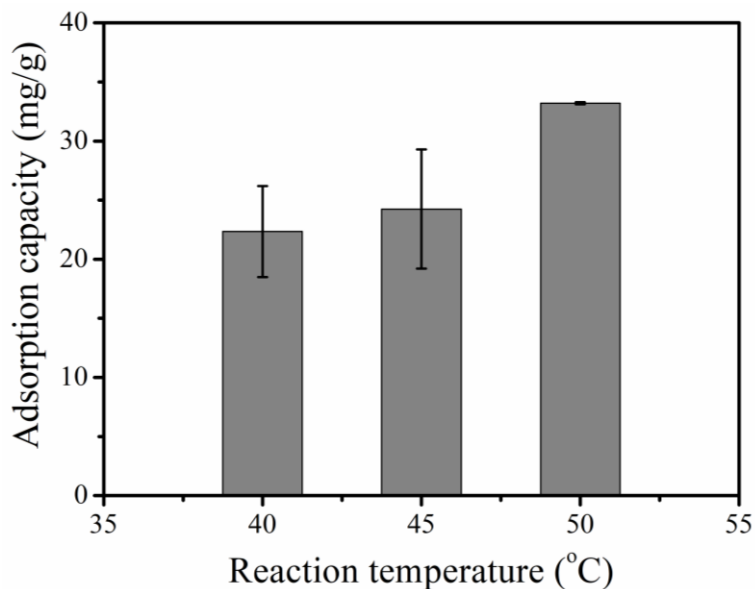
Fig. 3.7 Dependence of the etching of the SSNs core on the reaction temperature under sonication at 40 kHz, 54 W.

3.3.5 Influence of the temperature and time on the CTAB removal by microwave heating

Microwave as a new method for surfactant removal was investigated. The treatment temperature and time of microwave respectively were studied. The FT-IR spectra of CTAB, and HMSNs before and after CTAB extraction were shown in Fig. 3.8. The characteristic peaks of CTAB are found at 2925 cm^{-1} and 2853 cm^{-1}, corresponding to the asymmetric and symmetric stretching vibrations of the $-CH_2-$ group from the CTAB.[24] Similar peaks were observed in the HMSNs before CTAB removal, indicating that CTAB remained in the HMSNs. The characteristic peaks of CTAB at 2925 cm^{-1} and 2853 cm^{-1} disappear after the surfactant extraction by microwave treatment at 190°C for 5, 20, 10, and 30 min. The effect of different microwave heating temperatures (80, 120, and 160°C) on the removal of CTAB was further studied. The results show that the CTAB was removed by microwave treatment at 80°C for 5 min.
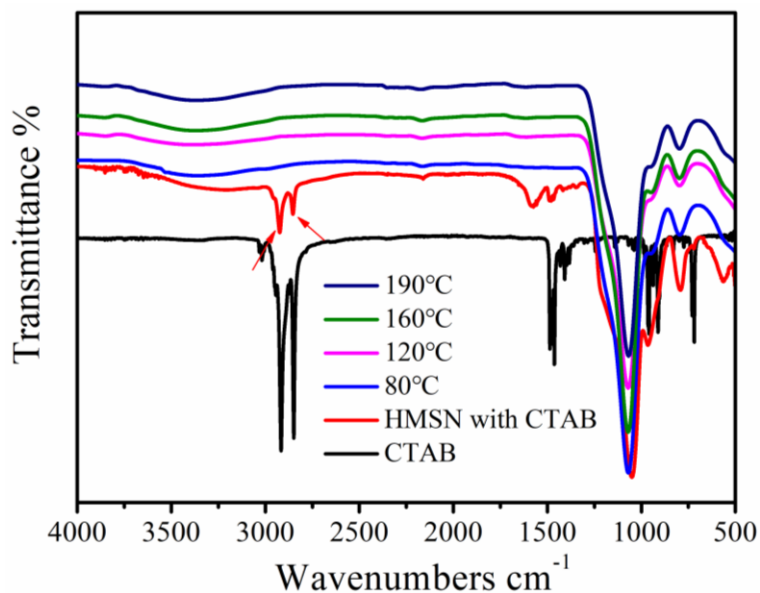
Fig. 3.8 **FT–IR spectrum of the HMSNs obtained by microwave heating at 80, 120, 160, and 190℃ for 5 min.**

3.3.6 Drug loading

Using distilled water as a blank control, the absorbance A of VOR was measured at a wavelength of 256 nm. The absorbance corresponding to the concentration of VOR was listed in Table 3.1. The UV absorption spectrum and standard curve of VOR were shown in Fig. 3.9. It can be seen from Fig. 3.9 that the fit of the standard curve is very well. The standard curve equation was obtained by the linear regression analysis on the concentration C value with the A value (equation (3-3)). The R^2 value is 0.99987, which meets the experimental requirements.

$$y = 0.05373 + 0.02447x \tag{3-3}$$

where y is the absorbance at 256 nm and x is the concentration of VOR expressed in μg/g.

By measuring the absorbance of the supernatant of the remaining solution, the amount of remaining VOR was calculated by using the standard curve equation.

The drug loading of HMSNs (ca. 9.63%) was calculated using equation (3-2) and equation (3-3).

Table 3.1 The absorbance corresponding to the concentration of VOR.

Concentration of VOR (µg/mL)	Absorbance 1	Absorbance 2	Average absorbance	error
15	0.422	0.419	0.421	0.001
20	0.558	0.542	0.547	0.008
25	0.669	0.662	0.666	0.004
30	0.797	0.781	0.789	0.008
40	1.039	1.019	1.029	0.010
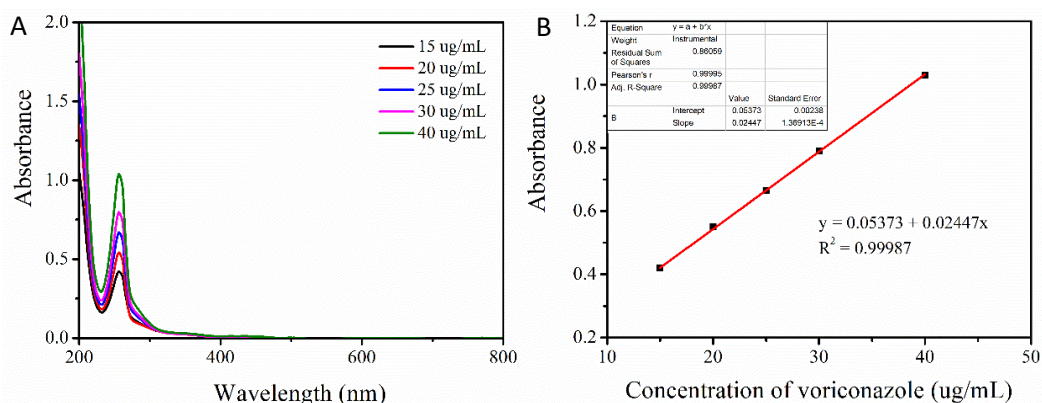
Fig. 3.9 The UV absorption spectrum (A) and standard curve of VOR (B).

Fig. 3.10A was the infrared spectrum of pure VOR. The aromatic C-C stretching peak appeared at 1622, 1596, and 1462 cm^{-1}.[25, 26] Aromatic C=C stretching vibrations were observed at 1518 and 1503 cm^{-1}.[25-27] The band at 1410 cm^{-1} represented the methylene C–H in-plane bending vibration.[27] Compared with the infrared spectrum of pure VOR, these characteristic peaks appeared at the same positions in the infrared spectrum of VOR-HMSNs after drug loading (Fig. 3.10B). Therefore, it was shown that the VOR drug was successfully loaded into the HMSNs material.
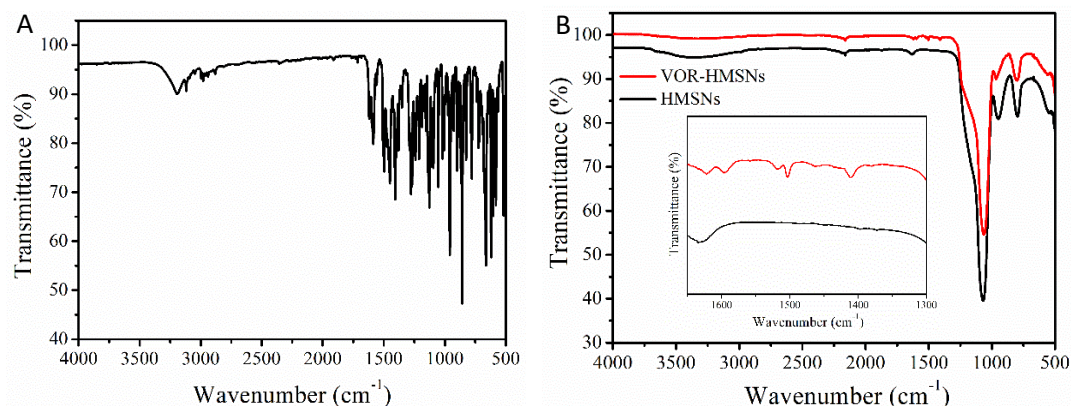
Fig. 3.10 The FT–IR spectrum of the pure VOR (A) and VOR-HMSNs (B).

3.3.7 Drug release

Using PB solution as the blank control solution, the absorbance A values of the test substances were measured at the maximum absorption wavelength, respectively. A suitable standard curve equation was obtained by performing linear regression analysis on the absorbance value A with concentration C. The absorbance corresponding to the concentration of VOR was listed in Table 3.2. The UV absorption spectrum and standard curve of VOR were shown in Fig. 3.11. The standard curve equation was obtained by the linear regression analysis on the concentration C value with the A value (equation (3-4)). The R^2 value is 0.99951, which meets the experimental requirements.

$$y = 0.08234 + 0.02282x \quad R^2 = 0.99951 \tag{3-4}$$

where y is the absorbance at 256 nm and x is the concentration of VOR expressed in µg/g.

Table 3.2 The absorbance corresponding to the concentration of VOR.

Concentration of VOR (μg/mL)	Absorbance 1	Absorbance 2	Average absorbance	error
10	0.324	0.306	0.315	0.009
15	0.433	0.421	0.427	0.007
20	0.539	0.535	0.537	0.002
25	0.657	0.653	0.655	0.002
30	0.763	0.768	0.766	0.002

The values of absorbance were measured with the taking-out samples at 5, 10, 20, 30, 45, 60, 120, 180, 240, 480, 1440, and 2160 min, respectively. The drug concentration was calculated according to the standard curve of VOR in PB to obtain the cumulative release amount of the VOR (Fig. 3.12).
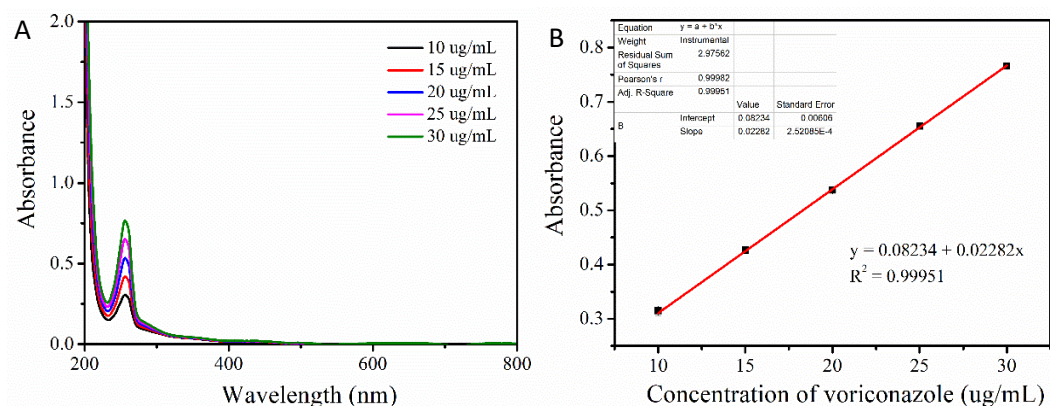
Fig. 3.11 The UV absorption spectrum (A) and standard curve of VOR (B).
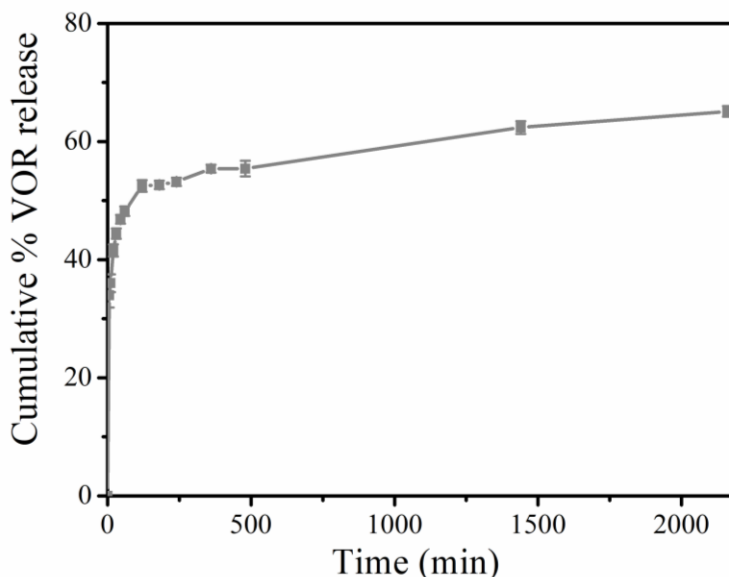
Fig. 3.12 The cumulative release amount of the VOR from VOR-HMSNs material in PB.

3.3.7.1 Kinetic studies of drug release

Kinetic release data were analysed by using the zero-order, first-order, Higuchi, and Korsmeyer-Peppas models.[28-30] A zero-order model describes a system in which the rate of drug release is independent of its concentration and is represented by the following equation:

$$Q_t = Q_0 + k_0 \times t \qquad (3\text{-}5)$$

where Q_t is the amount of drug released in time t, Q_0 is the initial amount of drug in the solution (in these studies, $Q_0 = 0$), and k_0 is the zero-order rate constant. The k_0 value is obtained from the slope of a linear curve of percent cumulative drug release versus time. Fig. 3.13A shows the release profile of VOR versus time. As can be seen the release of VOR increased rapidly with time in the first 60 min, then proceeded at a slower rate, and reached the equilibrium point after 720 min. The maximum release of VOR by HMSNs was 65.1%.

A first-order kinetic model describes the release of a system in which the release rate is concentration-dependent and can be expressed as follows:

$$\log C_t = \log C_0 - k_1 \frac{t}{2.303} \qquad \text{(3-6)}$$

where C_t is the concentration of drug released within time t, C_0 is the initial concentration of drug present in the HMSNs, and k_1 is the first-order rate constant. The value of k_1 was calculated from the slope of the linear curve of $\log cumulative\%$ percent drug residue over time (Fig. 3.13B).

The Higuchi model describes drug release from an insoluble matrix as the square root of a time-dependent process based on Fickian diffusion. In general, the Higuchi model can be expressed as:

$$Q_t = k_H \times t^{0.5} \qquad \text{(3-7)}$$

where k_H is the Higuchi constant. The value of k_H was taken from the slope of the linear curve of the cumulative% percent drug release versus the square root of time (Fig. 3.13C).

Korsmeyer derived a simple relation describing drug release from polymeric systems. The logarithmic form of the Korsmeyer-Peppas model is represented by the following equation:

$$\log Q_t = \log k + n \times \log t \qquad \text{(3-8)}$$

where k is the kinetic constant and n is the diffusion index, a measure of the primary mechanism of drug release. The values of n and k were calculated from the slope and intercept of the linear plot of $\log cumulative\%$ percent drug release versus $\log time$ (Fig. 3.13D). In the Korsmeyer-Peppas model, the n value is used to characterize the different release mechanisms of the drug. In the case, of cylindrical-shaped matrices, n ≤ 0.45 corresponds to a Fickian diffusion mechanism, 0.45 < n < 0.89 to anomalous (non-Fickian) diffusion, n = 0.89 to case II (relaxational) transport, and n > 0.89 to super case II transport.[31]
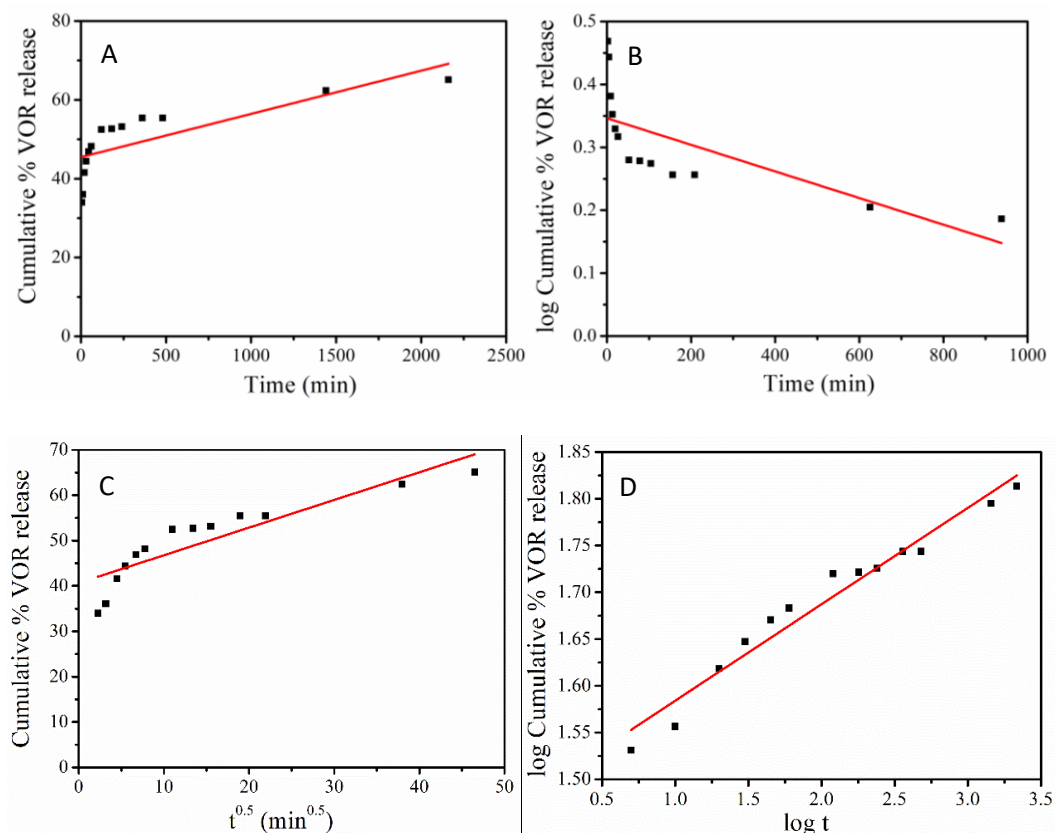
Fig. 3.13 **Kinetic release study presenting (A) cumulative percentage release of VOR from VOR-HMSNs versus time (zero-order model plot) and linear plot of: (B) log cumulative percentage remaining of VOR from VOR-HMSNs versus time (first-order model plot) (C) cumulative percentage release of VOR from VOR-HMSNs versus square root of time (Higuchi model plot) and (D) log cumulative percentage release of VOR from VOR-HMSNs versus log time (Korsmeyer–Peppas model plot).**

Table 3.3 presents the kinetic constants determined by the zero-order model, first-order model, Higuchi model, and Korsmeyer-Peppas model, and the corresponding correlation coefficients R^2 obtained from linear regression. The correlation coefficient R^2 of the Higuchi model was greater than that of the zero-order and one-order models. Therefore, clearly the VOR was released from the HMSNs material through a diffusion process.

Table 3.3 Correlation coefficients and kinetic constants of different kinetic models for release of VOR from VOR-HMSNs.

Zero-order model		First-order model		Higuchi model		Korsmeyer–Peppas model		
k_0	R^2	k_1	R^2	k_H	R^2	k	n	R^2
0.011	0.603	2.115	0.465	0.610	0.803	30.262	0.103	0.962

3.3.7.2 Effect of temperature

Generally, the temperature of the lesioned part of the human body is higher than the normal temperature (37°C). Therefore, 42°C was chosen to study the drug-release properties of HMSNs materials. Fig. 3.14 shows the release profile of VOR versus desorption time at two temperatures of 37°C and 42°C.
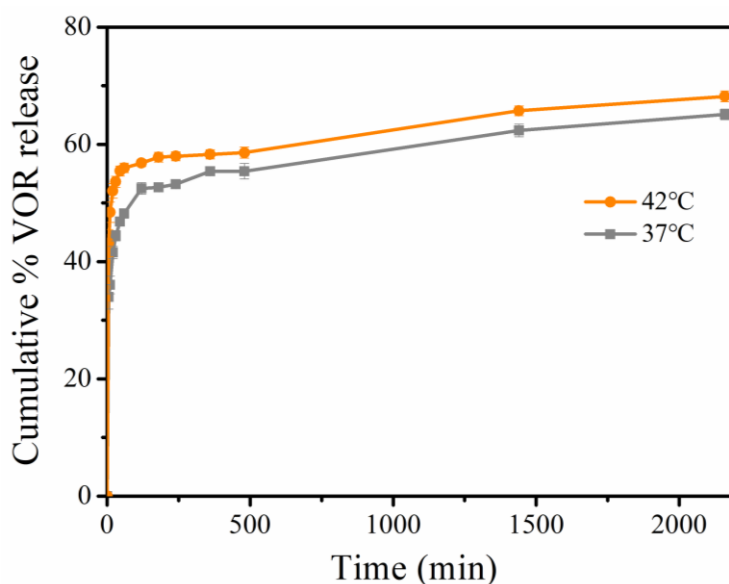
Fig. 3.14 The release profile of VOR-HMSNs versus desorption time at two temperatures of 37°C and 42°C.

The release of VOR at two temperatures increased rapidly with time in the first 60 min, then it proceeded at a slower rate and finally attained an equilibrium point after 36 h for 37°C and 42°C. The maximum release of VOR by HMSNs was 65.1% and 68.2% at 37°C and 42°C, respectively. The temperature effect can be attributed to the higher molecular mobility in the solution during the diffusion of VOR.[30, 32]

3.3.7.3 Effect of pH

Likewise, lesioned part of the human body has a pH lower than the normal one (pH 7.4). Therefore, pH 5.8 was chosen to study the drug-release properties of HMSNs materials. Fig. 3.15 shows the cumulative VOR release of VOR-HMSNs materials at different pH (7.4 and 5.8). The cumulative drug release at pH 5.8 in the initial stage was lower than that at pH 7.4. After 180 min, however, the cumulative drug release at pH 5.8 was higher than that at pH 7.4. Eventually, the cumulative drug release at pH 5.8 and pH 7.4 was the same at 36 h. As shown in Fig. 3.16, the release amount at all two pH values was well-fitted to the Higuchi model and Korsmeyer–Peppas model. The n values of the Korsmeyer–Peppas model obtained from Fig. 3.16 were 0.103 and 0.124 for pH 7.4 and pH 5.8, respectively. Thus, showing the VOR molecules pass through the pore of the silica shell with Fickian diffusion mechanism.
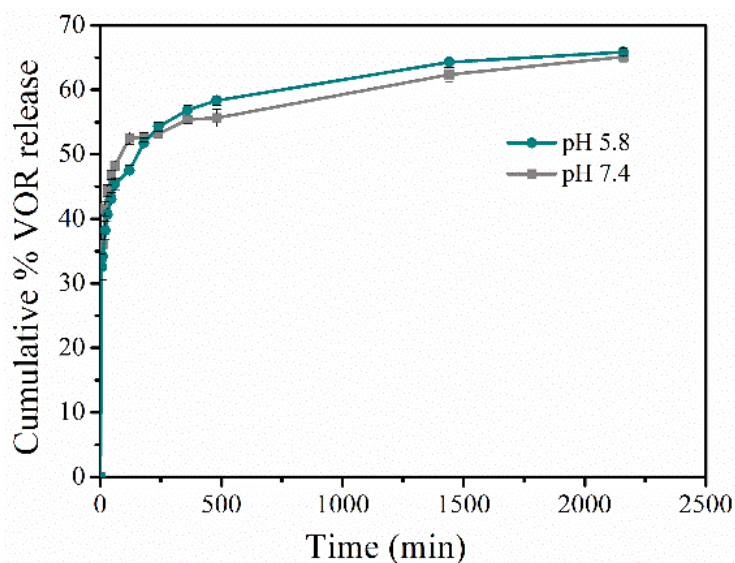

Fig. 3.15 The cumulative VOR release of VOR-HMSNs materials at different pH (7.4 and 5.8).
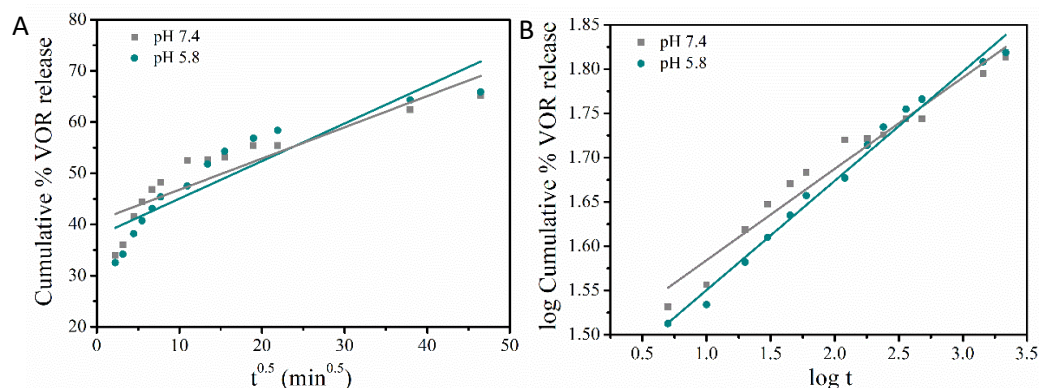
Fig. 3.16 Kinetic release study presenting (A) cumulative percentage release of VOR from VOR-HMSNs versus square root of time (Higuchi model plot) and (B) log cumulative percentage release of VOR from VOR-HMSNs versus log time (Korsmeyer–Peppas model plot) at pH 7.4 and pH 5.8.

3.4　Conclusions

HMSNs were prepared using the ultrasonic-assisted method. The effects of ultrasonic frequency, ultrasonic power, ultrasonic time, ultrasonic volume, and bulk temperature on etching were discussed. Ultrasonic frequency and ultrasonic power were a slight effect on the etching of SSNs core. However, etching was significantly affected by ultrasonic time and bulk temperature. In addition, a microwave-assisted method was used to remove the surfactant of CTAB. The effects of microwave treatment time and temperature on the removal efficiency of surfactant were studied respectively. The results show that the surfactant was completely removed by microwave heating at 80°C for 5 min. Finally, the drug loading and release characteristics of HMSNs materials were studied by using the antifungal drug VOR as a model drug. The release kinetics of HMSNs materials were studied. The effects of temperature and pH on drug release were investigated respectively. The maximum VOR release of VOR-HMSNs was 65.1% and 68.2% at 37°C and 42°C, respectively. At pH 5.8, the amount of VOR released from the VOR-HMSNs material was similar at pH 7.4.

References

[1] X.W. Lou, L.A. Archer, Z. Yang, Hollow micro‐/nanostructures: synthesis and applications, Advanced Materials, 20 (2008) 3987-4019.

[2] J. Liu, Z. Luo, J. Zhang, T. Luo, J. Zhou, X. Zhao, K. Cai, Hollow mesoporous silica nanoparticles facilitated drug delivery via cascade pH stimuli in tumor microenvironment for tumor therapy, Biomaterials, 83 (2016) 51-65.

[3] T.T.H. Thi, T.N.Q. Nguyen, D.T. Hoang, D.H. Nguyen, Functionalized mesoporous silica nanoparticles and biomedical applications, Materials Science and Engineering: C, 99 (2019) 631-656.

[4] B.Q. Bao, N.H. Le, D.H.T. Nguyen, T.V. Tran, L.P.T. Pham, L.G. Bach, H.M. Ho, T.H. Nguyen, D.H. Nguyen, Evolution and present scenario of multifunctionalized mesoporous nanosilica platform: A mini review, Materials Science and Engineering: C, 91 (2018) 912-928.

[5] Z.U. Rahman, N. Wei, Z. Li, W. Sun, D. Wang, Preparation of hollow mesoporous silica nanospheres: controllable template synthesis and their application in drug delivery, New Journal of Chemistry, 41 (2017) 14122-14129.

[6] J. Dou, H.C. Zeng, Targeted synthesis of silicomolybdic acid (keggin acid) inside mesoporous silica hollow spheres for Friedel–Crafts alkylation, Journal of the American Chemical Society, 134 (2012) 16235-16246.

[7] X. Du, J. He, Spherical silica micro/nanomaterials with hierarchical structures: Synthesis and applications, Nanoscale, 3 (2011) 3984-4002.

[8] X. Fang, X. Zhao, W. Fang, C. Chen, N. Zheng, Self-templating synthesis of hollow mesoporous silica and their applications in catalysis and drug delivery, Nanoscale, 5 (2013) 2205-2218.

[9] S.-H. Wu, C.-Y. Mou, H.-P. Lin, Synthesis of mesoporous silica nanoparticles, Chemical Society Reviews, 42 (2013) 3862-3875.

[10] S. Sun, X. Zhao, M. Cheng, Y. Wang, C. Li, S. Hu, Facile preparation of redox-responsive hollow mesoporous silica spheres for the encapsulation and controlled release of corrosion inhibitors, Progress in Organic Coatings, 136 (2019) 105302.

[11] T. Yan, J. He, R. Liu, Z. Liu, J. Cheng, Chitosan capped pH-responsive hollow mesoporous silica nanoparticles for targeted chemo-photo combination therapy, Carbohydrate Polymers, 231 (2020) 115706.

[12] Y. Li, B.P. Bastakoti, M. Imura, J. Tang, A. Aldalbahi, N.L. Torad, Y. Yamauchi, Dual soft‐template system based on colloidal chemistry for the synthesis of hollow mesoporous silica nanoparticles, Chemistry–A European Journal, 21 (2015) 6375-6380.

[13] P. Gao, C. Yu, L. Du, H. Luo, Y. Li, C. Wei, Preparation and research progress of hollow mesoporous silica microsphere, New Chemical Materials, 47 (2019) 31-34.

[14] D.A. Loy, K.J. Shea, Bridged polysilsesquioxanes. Highly porous hybrid organic-inorganic materials, Chemical Reviews, 95 (1995) 1431-1442.

[15] R. Kumar, V. Sinha, Preparation and optimization of voriconazole microemulsion for ocular delivery, Colloids and Surfaces B: Biointerfaces, 117 (2014) 82-88.

[16] P. Srinivas, K. Sreeja, Formulation and evaluation of voriconazole loaded nanosponges for oral and topical delivery, International Journal of Drug Development & Research, 5 (2013) 55-69.

[17] W. Faisal, G.M. Soliman, A.M. Hamdan, Enhanced skin deposition and delivery of voriconazole using ethosomal preparations, Journal of Liposome Research, 28 (2018) 14-21.

[18] C.K. Song, P. Balakrishnan, C.-K. Shim, S.-J. Chung, S. Chong, D.-D. Kim, A novel vesicular carrier, transethosome, for enhanced skin delivery of voriconazole: characterization and in vitro/in vivo evaluation, Colloids and Surfaces B: Biointerfaces, 92 (2012) 299-304.

[19] T. Waghule, V.K. Rapalli, G. Singhvi, P. Manchanda, N. Hans, S.K. Dubey, M.S. Hasnain, A.K. Nayak, Voriconazole loaded nanostructured lipid carriers based topical delivery system: QbD based designing, characterization, in-vitro and ex-vivo evaluation, Journal of Drug Delivery Science and Technology, 52 (2019) 303-315.

[20] R.F. Contamine, A. Wilhelm, J. Berlan, H. Delmas, Power measurement in sonochemistry, Ultrasonics Sonochemistry, 2 (1995) S43-S47.

[21] X. Liu, Z. Wu, M. Manzoli, L. Jicsinszky, R. Cavalli, L. Battaglia, G. Cravotto, Medium-high frequency sonication dominates spherical-SiO_2 nanoparticle size, Ultrasonics Sonochemistry, 90 (2022) 106181.

[22] A. Chen, Y. Li, Y. Yu, Y. Li, K. Xia, Y. Wang, S. Li, L. Zhang, Synthesis of hollow mesoporous carbon spheres via "dissolution-capture" method for effective phenol adsorption, Carbon, 103 (2016) 157-162.

[23] Y. Teng, Y. Du, J. Shi, P.W. Pong, Magnetic iron oxide nanoparticle-hollow mesoporous silica spheres: fabrication and potential application in drug delivery, Current Applied Physics, 20 (2020) 320-325.

[24] M. Zargar, Y. Hartanto, B. Jin, S. Dai, Hollow mesoporous silica nanoparticles: A peculiar structure for thin film nanocomposite membranes, Journal of Membrane Science, 519 (2016) 1-10.

[25] N.Ü. Okur, V. Yozgatlı, M.E. Okur, A. Yoltaş, P.I. Siafaka, Improving therapeutic efficacy of voriconazole against fungal keratitis: Thermo-sensitive in situ gels as ophthalmic drug carriers, Journal of Drug Delivery Science and Technology, 49 (2019) 323-333.

[26] S. Lankalapalli, V.D. Vemuri, V.V.K. Tenneti, P.R. Guntaka, Bioavailability enhancement of voriconazole using liposomal pastilles: Formulation and experimental design investigation, Journal of Liposome Research, 32 (2022) 293-307.

[27] Y.-M. Zhao, G.-M. Tang, Y.-T. Wang, Y.-Z. Cui, Synthesis, spectroscopic studies, antimicrobial activity, and crystal structure of a Zn (II) complex based on voriconazole, Journal of Coordination Chemistry, 70 (2017) 189-200.

[28] S. Kakar, R. Singh, A. Semwal, Drug release characteristics of dosage forms: a review, Journal of Coastal Life Medicine, 2 (2014) 332-336.

[29] J.P. Raval, D.R. Naik, K.A. Amin, P.S. Patel, Controlled-release and antibacterial studies of doxycycline-loaded poly (ε-caprolactone) microspheres, Journal of Saudi Chemical Society, 18 (2014) 566-573.

[30] E. Mijowska, K. Cendrowski, M. Barylak, W. Konicki, Sandwich-like mesoporous silica flakes for anticancer drug transport-synthesis, characterization and kinetics release study, Colloids and Surfaces B: Biointerfaces, 136 (2015) 119-125.

[31] G. Singhvi, M. Singh, In-vitro drug release characterization models, International Journal of Pharmaceutical Studies and Research, 2 (2011) 77-84.

[32] J. Liu, S. Lin, L. Li, E. Liu, Release of theophylline from polymer blend hydrogels, International Journal of Pharmaceutics, 298 (2005) 117-125.

Chapter 4: Ultrasonic Preparation of Calcium Carbonate Nanoparticles

Abstract

$CaCl_2$ and Na_2CO_3 solutions were used as reactants to prepare calcium carbonate ($CaCO_3$) particles under the action of low-frequency ultrasonic. The effects of reactant concentration, ultrasonic time, ultrasonic power, and reactant volume on the particle size of the prepared $CaCO_3$ were investigated. Compared to stirring, small $CaCO_3$ particles were obtained with low-frequency ultrasonic. Then the characterization methods of Field Emission Scanning Electron Microscope (FESEM), X-ray diffraction (XRD) and Fourier-transform infrared (FT-IR) were used to characterize the morphology and crystallization of the prepared $CaCO_3$ samples. The characterization of FESEM showed that the flakes of $CaCO_3$ were obtained under the action of ultrasound, although under stirring, they were in the shape of squares. The prepared $CaCO_3$ was calcite through XRD and FT-IR characterization. The mechanism of preparing $CaCO_3$ under the action of ultrasound is discussed. The nucleation rate of $CaCO_3$ by cavitation bubbles and the inhibition of crystal growth by hydroxyl radicals are discussed respectively. The surface of the cavitation bubble provided active sites for $CaCO_3$ nucleation resulting in the nucleation rate increasing. In addition, the generated hydroxyl radicals by sonication interacted with Ca^{2+} ions to inhibit the growth of crystals.

4.1 Introduction

$CaCO_3$ nanoparticles (nano-$CaCO_3$) are widely used in rubber, paper, coatings, and so forth.[1] For the preparation of hollow nanomaterials, nano-$CaCO_3$ has been used as a template for preparing hollow nanomaterials due to its low toxicity and easy removal.[2, 3] Various methods are available for the synthesis of $CaCO_3$ particles, including Ca^{2+}–CO_3^{2-} system, solid–liquid–gas carbonation, water-in-oil reverse emulsion, and biomimetic $CaCO_3$ formation.[4] To date, 20-50 nm of nano-$CaCO_3$ particles can be obtained with $Ca(OH)_2$ suspension and CO_2 flow rate by using sonochemical carbonization, ultrasonic spraying, or sono-atomization.[1, 5, 6] However, the reactions are affected by many factors, such as the mass fraction of $Ca(OH)_2$ suspension, CO_2 gas flow rate, the carbonization temperature, the amount/size of spray droplets, etc., leading to difficult and complicated control. In

addition, the investment and maintenance costs of ultrasonic-assisted carbonization and spraying methods are relatively high.

The simplest and most effective strategy for the synthesis of $CaCO_3$ particles is used in the Ca^{2+}–CO_3^{2-} reaction system, which contains usually calcium salts ($CaCl_2$ or $Ca(NO_3)_2$) and carbonate salts (Na_2CO_3, $NaHCO_3$, K_2CO_3 or $(NH_4)_2CO_3$) for the precipitation/crystallization process.[4] However, the larger particle size of obtained $CaCO_3$ with the Ca^{2+}-CO_3^{2-} reaction system limited its application. To reduce the particle size, sonication was attempted in the Ca^{2+}-CO_3^{2-} system. It has been widely reported that sonication can reduce particle size by controlling the nucleation rate and growth rate of crystals.[1, 5, 7, 8] In 2010, Kojima et al. studied the effect of the ultrasonic amplitude and frequency on the particle size of $CaCO_3$ in the sonication system containing $CaCl_2$ and $(NH_4)_2CO_3$ solutions.[9] They found that the particle size of $CaCO_3$ formed under 20 kHz sonication was about 2 μm, which was much smaller than that obtained with stirring (20 μm), and the ultrasonic amplitude did not almost affect the particle size at 20 kHz. However, the particle size of $CaCO_3$ decreased with the increasing ultrasonic amplitude at 40 kHz. In 2014, Njegić Džakula et al. studied the effect of sonication on $CaCO_3$ precipitation with $CaCl_2$ and Na_2CO_3 solutions.[8] Compared with stirring, the particle sizes were reduced by sonication from 4–22 μm to 1–18 μm at 25°C and from 14–17 μm to 2–7 μm at 80°C, respectively. Particle size of spherical $CaCO_3$ from 4–8 μm to 1–6 μm under sonication at higher supersaturation and from 10–22 μm to 8–18 μm at lower supersaturation, respectively. It was believed that the increasing nucleation rate under sonication led to the reduction of the particle size. Meanwhile, Kirboga et al. reported that adding carboxymethyl inulin to the reaction system of $CaCl_2$ and Na_2CO_3 solutions can reduce the particle size from 3.91–7.50 μm to 0.91 μm under sonication.[7] In 2017, Juhasz-Bortuzzo et al. obtained 354±99 nm of spherical $CaCO_3$ particles with 1 M $NaHCO_3$ and $Ca(CH_3CO_2)_2$ H_2O solutions using 1 min pulse sonication (1 s on and 0.2 s off) at the highest ultrasonic amplitude.[10] To date, there were few reports for the preparation of $CaCO_3$ nanoparticles by sonication in the Ca^{2+}-CO_3^{2-} system, although the particle size of $CaCO_3$ was significantly reduced by sonication.

Ultrasound was used to prepare $CaCO_3$ nanoparticles. The effects of ultrasonic power, sonication time, and reaction volume on the synthesis of $CaCO_3$ nanoparticles were studied. The mechanism of preparing $CaCO_3$ under the action

of ultrasound is discussed. The nucleation rate of $CaCO_3$ by cavitation bubbles and the inhibition of crystal growth by hydroxyl radicals are also discussed respectively. The surface of the cavitation bubble provided active sites for $CaCO_3$ nucleation resulting in the nucleation rate increasing. In addition, the generated hydroxyl radicals by sonication interacted with Ca^{2+} ions to inhibit the growth of crystals.

4.2 Experimental

4.2.1 Reagents and apparatus

Calcium chloride ($CaCl_2$, 93%, Alfa Aesar), sodium carbonate monohydrate ($Na_2CO_3 \cdot H_2O$, ≥99.5%, Sigma-Aldrich), sodium hexametaphosphate (($NaPO_3)_6$, Alfa Aesar) were used without additional purification.

An ultrasonic cup (home-made, 19.5 kHz) was used to prepare nano-$CaCO_3$ and HMSNs, as shown in Fig. 4.1.

① Ultrasonic generator
② Fan cooling
③ Ultrasonic transducers
④ Cup reactor
⑤ Cooling water inlet
⑥ Cooling water outlet
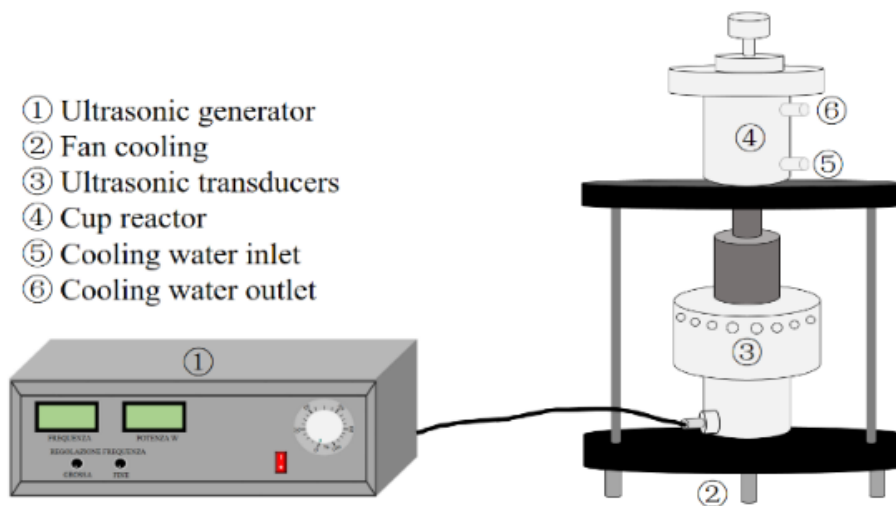
**Fig. 4.1 Ultrasonic cup-horn apparatus (home-made, 19.5 kHz).**

An ultrasonic generator was used to regulate ultrasonic power, which can be adjusted up to 300 W (electric input power). The ultrasonic transducers consist of high-efficiency pre-stressed piezoelectric (PZT) rings (planar PZT Morgan Electronics, diameter 50 mm) compressed between two erga discs. The maximum capacity of

the cup reactor is 80 mL, which is cooled with cooling water. The ultrasonic powers delivered were determined calorimetrically with water as heating media and all ultrasonic power mentioned below refers to the power measured calorimetrically.[11]

In comparison, a magnetic stirrer (AREX VELP Scientifica, Italy) was also used to prepare $CaCO_3$. The obtained $CaCO_3$ and HMSNs were collected by centrifugation with a centrifuge (Allegra 64R Benchtop Centrifuge, Beckman Coulter, Italy). The hydraulic diameters of the obtained $CaCO_3$ and HMSNs were analyzed by Quasi Elastic Light Scattering (QELS) (Brookhaven Instruments Corporation; 90 plus).

4.2.2 Typical preparation of $CaCO_3$ particles

In general, the reaction between Na_2CO_3 and $CaCl_2$ to form $CaCO_3$ is given by reaction equation (4-1).[12]

$$Na_2CO_3 \text{ (aq)} + CaCl_2 \text{ (aq)} = CaCO_3\downarrow + 2NaCl \text{ (aq)} \tag{4-1}$$
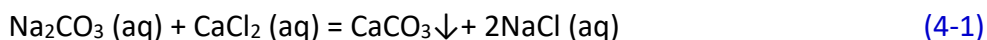
With agitation: 15 mL of 0.5 M $CaCl_2$ solution was added into a 100 mL beaker. 15 mL of Na_2CO_3 (0.5 M) solution was then rapidly added into 15 mL of the above $CaCl_2$ solution with stirring. After 30 min stirring (600 rpm), the $CaCO_3$ precipitate was collected by centrifuge and washed 3 times with distilled water.

With sonication: 15 mL of 0.5 M $CaCl_2$ solution was added to the ultrasonic cup reactor. The ultrasonic cup was turned on (19.5 kHz; 17.6 W) and then 15 mL of 0.5 M Na_2CO_3 solution was added into the $CaCl_2$ solution rapidly. After 30 min sonication, the $CaCO_3$ precipitate was collected by centrifuge and washed 3 times with distilled water. The effects of single factors such as reactants concentration ($CaCl_2$ (0.0125-0.5 M) and Na_2CO_3 (0.0125-0.5 M)), sonication time (3-30 min), ultrasonic power (12.2-26.7 W), and solutions volume (10-50 mL) on the particles size of $CaCO_3$ were studied.

4.2.3 Characterization

The $CaCO_3$ nanoparticles were dispersed in a solution for nanoparticle size measurement using QELS. Optimal conditions for particle size measurement:

0.1200 g CaCO$_3$ was added in 10 mL dispersant solution (0.1% sodium pyrophosphate) with sonication at 35 kHz and 35 W for 1 min. ca 3 mL of dispersant solution was extracted and added in the cuvette. Suspension in the cuvette was sonicated at 35 kHz and 35 W for 6 min, and particle size detection was immediate.

Ultra-high resolution field emission scanning electron microscope (FESEM) measurements were performed on a Tescan S9000G FESEM 3010 microscope (30 KeV) equipped with a high-brightness Schottky emitter. For analysis, the powder samples were deposited on a stub coated with a conducting adhesive and inserted in the chamber by a fully motorized procedure. The Fourier-transform infrared spectroscopy (FT-IR, Spectrum Two, PerkinElmer, USA) was measured by a spectrometer from 500 to 4000 cm^{-1} at 2 cm^{-1} resolution with 64 scans. Powder X-ray diffraction (XRD) patterns were collected with a PW3050/60 X'Pert PRO MPD diffractometer from PANalytical working in Bragg–Brentano geometry, using as a source the high-powered ceramic tube PW3373/10 LFF with a Cu anode (Cu Kα1 radiation λ = 1.5406 Å) equipped with a Ni filter to attenuate K$_\beta$. Scattered photons were collected by a real-time multiple strip (RTMS) X'celerator detector. Data were gathered in the 5°≤2θ≤90° angular range, with 0.02° 2θ steps. The powdered sample was examined in its as-received form and posed in a spinning sample holder to minimize the preferred orientations of crystallites.

4.3   Results and discussion

4.3.1 Comparison of CaCO$_3$ crystalline structures obtained by agitation and sonication

The formation process of CaCO$_3$ particles includes nucleation and crystal growth. The cavitation bubbles induced by sonication provide the nucleation sites for CaCO$_3$ crystallization, reducing the size of CaCO$_3$ particles.[5] The FESEM images of CaCO$_3$ particles obtained under agitation and sonication were compared in Fig. 4.2.
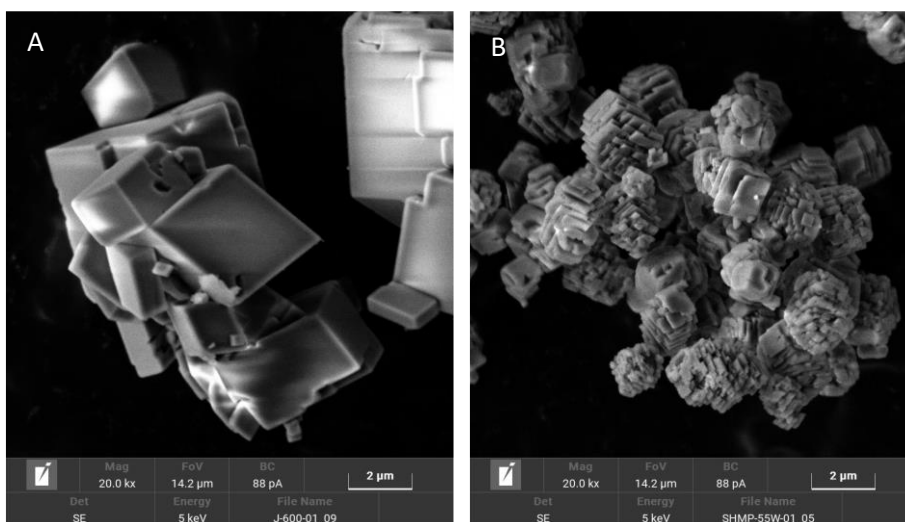
Fig. 4.2 **FESEM images of CaCO₃ particles obtained with agitation (A) and sonication (B). Conditions: 15 mL of 0.5 M Na₂CO₃ solution was added to 15 mL of 0.5 M CaCl₂ solution and stirred (600 rpm) or sonicated at 17.6 W for 30 min.**

The particle size of $CaCO_3$ obtained by sonication was significantly smaller than that by agitation. The particles obtained by agitation show complete cubes, while the particles obtained sonochemically show regular cube-shaped aggregates composed of thin slices and the distribution of particle sizes is relatively uniform. This finding of crystal size reduction and narrowing of the crystal size distribution by sonication is consistent with previous studies.[13, 14] It has been suggested that the nucleation rate increased due to the cavitation effects such as shockwaves, microturbulence, and microjet, which also determined the subsequent growth of these nucleated crystal nuclei.[13] In comparison, the nucleation rate was influenced more significantly. Namely, the crystal nucleation sites are provided by the cavitation bubbles' surface, resulting in an increased rate of crystal nucleation.[15, 16] Therefore, the decreasing of crystal size and the narrowing of the crystal size distribution under sonication is caused by the number of cavitation bubbles formed in the ultrasonic system. Moreover, XRD and FT-IR spectra analysis of prepared $CaCO_3$ particles can help to identify $CaCO_3$ polymorphs (calcite, aragonite or vaterite), as shown in Fig. 4.3 and Fig. 4.4.
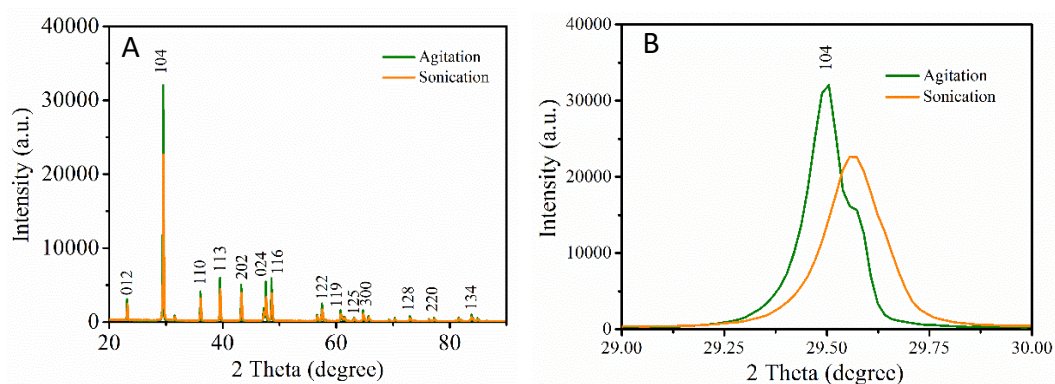
Fig. 4.3 Comparison of XRD spectrum of obtained CaCO$_3$ particles with agitation and sonication (A), and a zoomed-in version of crystalline peaks of 104 (B). Conditions: 15 mL of 0.5 M Na$_2$CO$_3$ solution was added to 15 mL of 0.5 M CaCl$_2$ solution with agitation at 600 rpm or sonicated at 17.6 W and 19.5 kHz for 30 min.
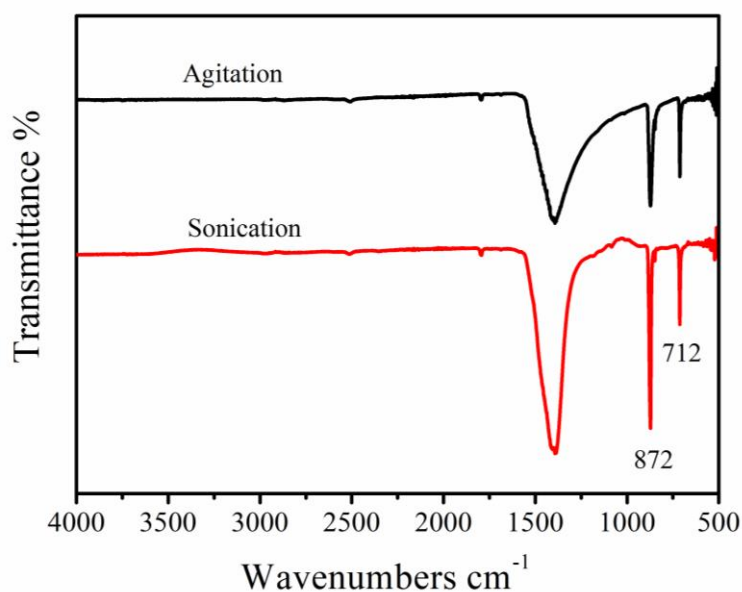

Fig. 4.4 FT-IR spectrum of obtained CaCO$_3$ particles with agitation and sonication. Conditions: 15 mL of 0.5 M Na$_2$CO$_3$ solution were added to 15 mL of 0.5 M CaCl$_2$ solution with agitation (600 rpm) or sonicated (17.6 W) for 30 min.

As shown in Fig. 4.3A, the main characteristic peaks of aragonite, vaterite, and calcite at 2θ of 26.2°, 26.9° and 29.4° correspond to 111, 112 and 104 crystal planes, respectively.[17, 18] Clearly, the 104 peak of calcite appeared at 29.5°. The peaks of aragonite (111) and vaterite (112) planes were not observed at 26.2° and 26.9°. Therefore, the obtained $CaCO_3$ particles belong to calcite. It confirms the enhancement of sonication on the nucleation rate since the high nucleation rate favors the formation of calcite.[19] As shown in Fig. 4.3B, the peak intensity of 104 crystal planes decreases under sonication. It may be caused by the crystal size reduction due to the interaction between Ca^{2+} ions and hydroxyl radicals generated by sonication to inhibit crystal growth.[20-23] In addition, the angle shift of the 104 crystal peak of nano-$CaCO_3$ particles obtained by sonication occurs compared to the sample prepared with stirring. It is attributed to the transformation from the calcite-I phase to the calcite–II phase. Probably, the shock waves can induce a crystal phase transition of nano-$CaCO_3$ particles.[24]

Based on the FT-IR spectra of calcite (Fig. 4.4), aragonite and vaterite, the peak positions of the external plane bending vibration of CO_3^{2-} and the internal plane bending vibration of O–C–O were different. Calcite, aragonite and vaterite have CO_3^{2-} peaks at 876, 853 and 870 cm^{-1}, respectively.[25] The peak positions of the O–C–O internal plane bending vibrations of calcite, aragonite and vaterite were 714, 700 and 745 cm^{-1}, respectively.[25] As shown in Fig. 4.4, the prepared $CaCO_3$ particles only have peaks at 872 and 712 cm^{-1}. It is further proved that the prepared $CaCO_3$ particles are calcite.

4.3.2 Effects of critical factors on the particle size of $CaCO_3$

4.3.2.1 *Effect of ultrasonic power*

Fig. 4.5 shows that the hydrodynamic diameter size (HDS, the average diameter of $CaCO_3$ was measured in a dispersant solution by using QELS.) of nano-$CaCO_3$ changed with ultrasonic power in 20 and 30 mL of reaction solutions, respectively.
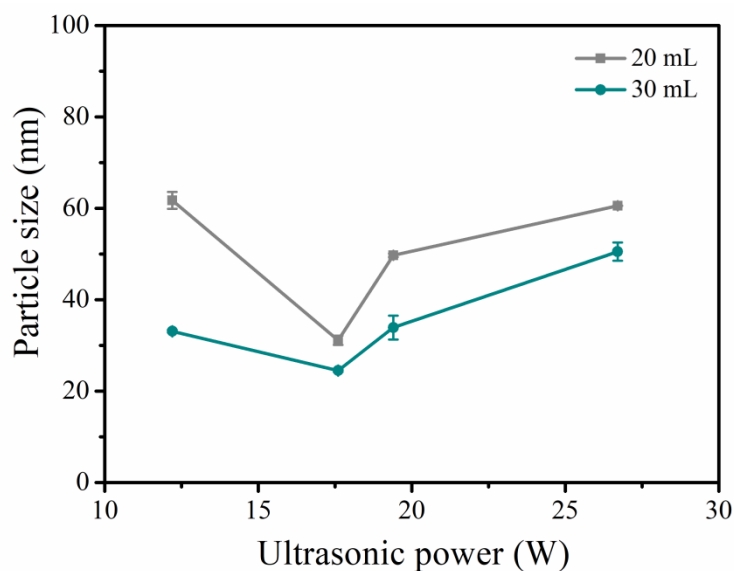
Fig. 4.5 Dependence of HDS of nano-CaCO₃ particles determined by QELS on ultrasonic power. Conditions: 10 or 15 mL of 0.5 M Na₂CO₃ and 10 mL or 15 mL of 0.5 M CaCl₂ were sonicated at 19.5 kHz for 3 min.

As shown in Fig. 4.5, the particle size of nano-CaCO₃ decreased with the increasing ultrasonic power in the range from 12.2 W to 17.6 W. As mentioned above, the cavitation bubbles' surface may provide the ideal nucleation sites, and the number of crystal nuclei should be correlated with the number of cavitation bubbles, which increase with increasing ultrasonic power.[26] Namely, the more cavitation bubbles cause increasing crystal nuclei and their dispersion, resulting in decreasing crystal size.[13] However, the nano-CaCO₃ particle size increased with the increasing ultrasonic power as the ultrasonic power continued to increase from 17.6 W to 26.7 W. It may be attributed to the increasing size of cavitation bubbles, namely, increase of ineffective cavitation bubbles resulted in the reduction of effective nucleation sites and decrease of hydroxyl radicals generated in situ.[26] The weaker interaction between OH radicals and Ca^{2+} ions is favorable to the growth of crystals and the increase of particle size.[20]

Fig. 4.6 shows that XRD patterns of CaCO₃ particles obtained with different ultrasonic powers. As shown in Fig. 4.6, the peak intensity of the 104 crystal plane decreased at 17.6 W compared with 12.2 W, since the amount of produced OH radicals increased with the increasing of ultrasonic power. However, the peak

intensity of the 104 crystal plane increased at 26.7 W, since the yield of OH radicals reduced due to the decreasing number of effective cavitation bubbles at 26.7 W. It further illustrates that OH radicals generated sonochemically can inhibit the growth of crystals. In addition, the 104 crystal peak of calcite obtained by sonication is angle shifted. It may be caused by the shockwave generated by sonication, resulting in the transformation of the calcite crystal phase.[24]
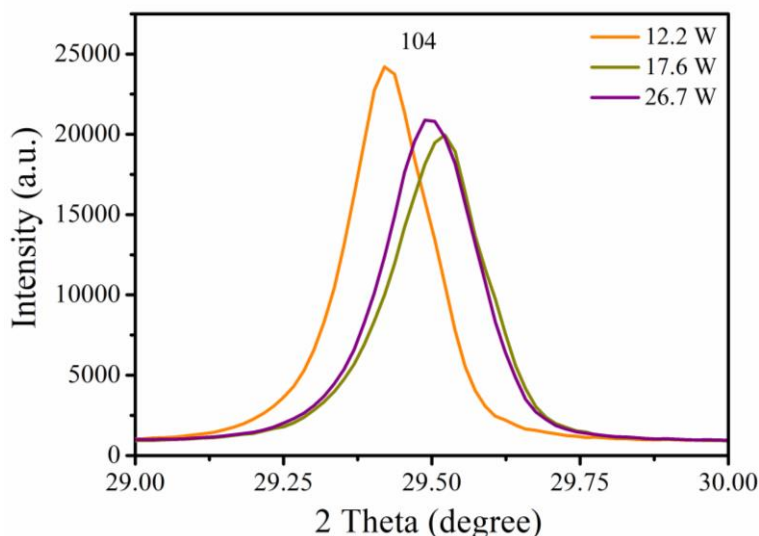

Fig. 4.6 XRD spectrum of CaCO₃ particles obtained under sonication at different ultrasonic powers. Conditions: 10 mL of 0.5 M Na₂CO₃ and 10 mL of 0.5 M CaCl₂ were sonicated at 19.5 kHz for 3 min.

Similar results were observed with the FESEM analysis (Fig. 4.7). As shown in Fig. 4.7, the particle size of CaCO₃ decreased with increasing ultrasonic power from 12.2 W to 17.6 W, and then the particle size of CaCO₃ increased 26.7 W. However, the nano-CaCO₃ sizes detected using FESEM are different from that measured using QELS analysis. The nano-CaCO₃ particles were dispersed in a dispersant solution without drying for QELS analysis, whereas the nano-CaCO₃ particles were dried for the FESEM measurement. Thus, the dried nano-CaCO₃ particles tended to agglomerate, resulting in the large diameter detected by FESEM.
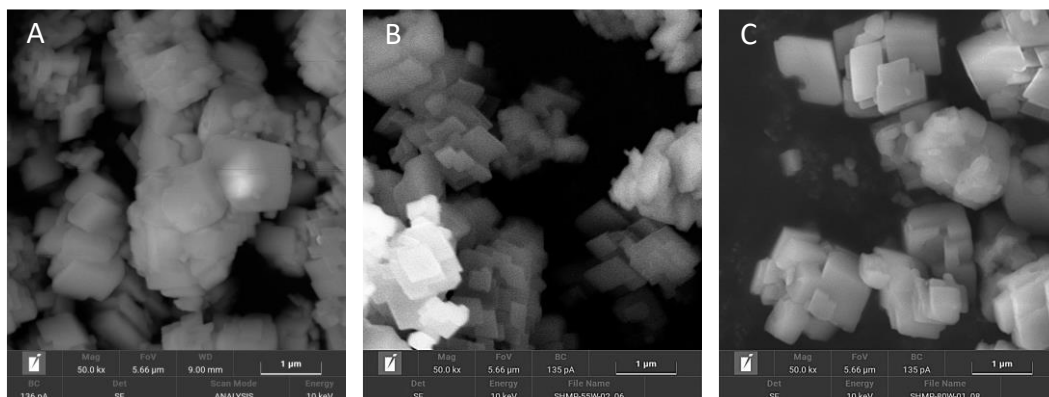
Fig. 4.7 FESEM images of CaCO₃ particles obtained by sonication at 12.2 W (A), 17.6 W (B) and 26.7 W (C). Conditions: 10 mL of 0.5 M Na₂CO₃ and 10 mL of 0.5 M CaCl₂ were sonicated at 19.5 kHz for 3 min.

4.3.2.2 *Influence of sonication time*

The particle size of nano-$CaCO_3$ obtained at a reaction volume of 30 mL is smaller than that at a reaction volume of 20 mL. If the 30 mL of reaction volume is chosen, changing the reaction conditions will have no significant impact nor change in the particle size. Since the particle size obtained under the condition of 30 mL is relatively small. To avoid this effect, a 20 mL reaction volume was selected for further research, so that the effect of changing the reaction conditions on the particle size is more significant.

Fig. 4.8 shows the change in particle size of nano-$CaCO_3$ as a function of sonication time at 17.6 W (19.5 kHz). As shown in Fig. 4.8, the particle size of nano-$CaCO_3$ increased slightly with the sonication time, indicating that the formation of nano-$CaCO_3$ particles occurs instantaneously. Sonication provides numerous cavitation bubbles as crystalline nuclei at the initial stage to control the crystal formation, growth, and the particle size, while the mechanical crushing of sonication on the large particles slightly affected the reduction of the particle size at the later stage.
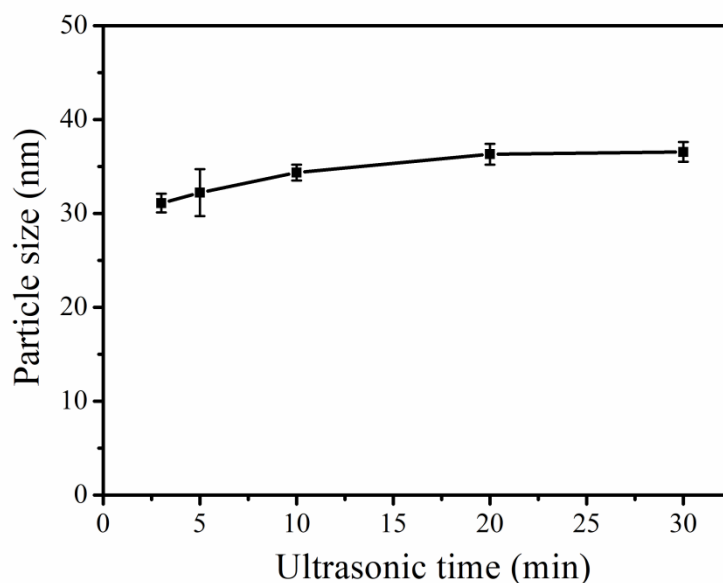
Fig. 4.8 Influence of sonication time on HDS of nano-CaCO$_3$ particles determined by QELS. Conditions: 10 mL of 0.5 M Na$_2$CO$_3$ and 10 mL of 0.5 M CaCl$_2$ were sonicated at 19.5 kHz and 17.6 W.

Fig. 4.9 shows the FESEM images of CaCO$_3$ particles prepared by sonication for 3 min and 30 min, respectively. The size of CaCO$_3$ particles obtained by sonication for 30 min was relatively larger than that obtained by sonication for 3 min. It further demonstrates that the size reduction of CaCO$_3$ particles was not caused by ultrasonic pulverization. In contrast, the dissolution-redeposition near the surface causes the larger particles and the higher peak intensity of the 104 crystal plane in the XRD patterns of CaCO$_3$ particles with the sonication time, as shown in Fig. 4.10.[27, 28]
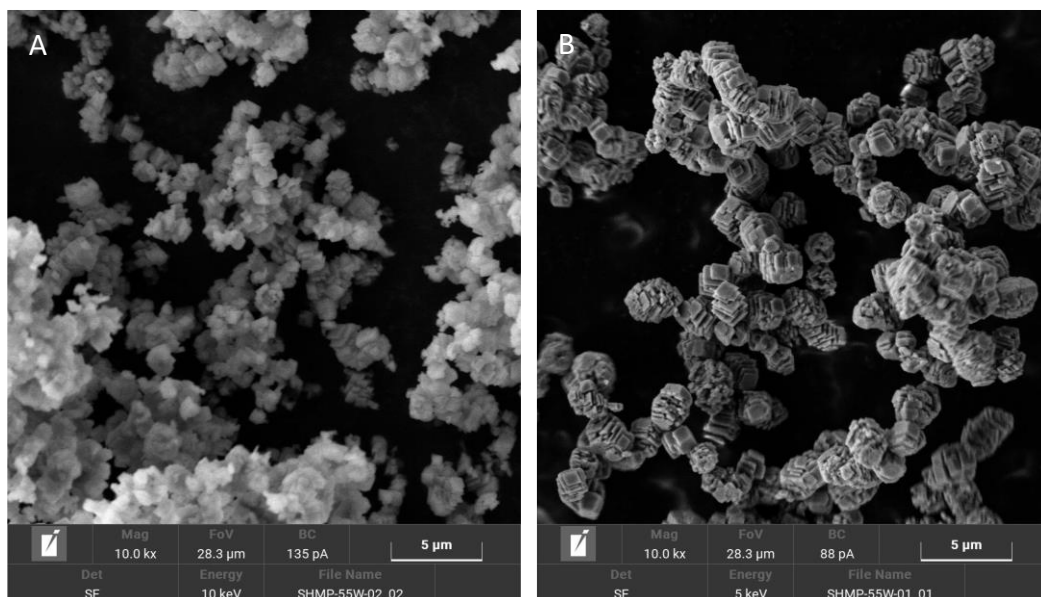
Fig. 4.9 FESEM images of CaCO₃ particles prepared by sonication for 3 min (A) and 30 min (B). Conditions: 10 mL of 0.5 M Na₂CO₃ and 10 mL of 0.5 M CaCl₂ were sonicated at 19.5 kHz and 17.6 W.
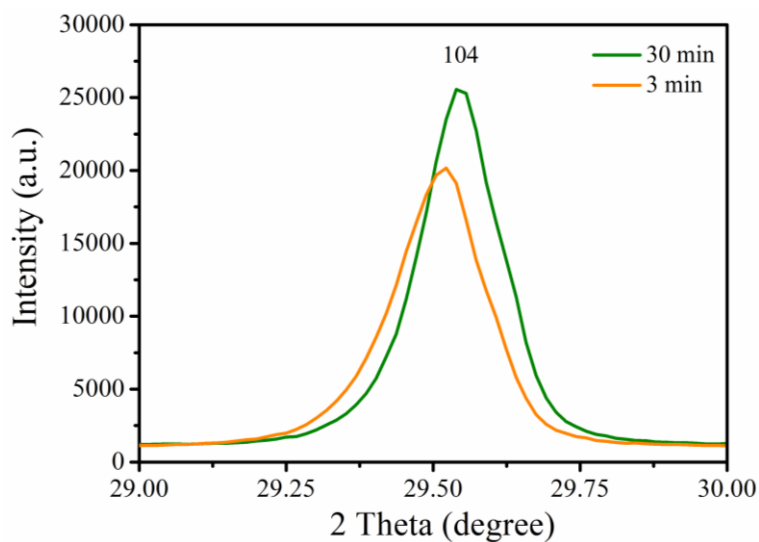

Fig. 4.10 XRD spectrum of CaCO₃ particles prepared under sonication for 3 min and 30 min. Conditions: 10 mL of 0.5 M Na₂CO₃ and 10 mL of 0.5 M CaCl₂ were sonicated at 19.5 kHz and 17.6 W.

4.3.2.3 Role of initial concentration of Na₂CO₃ and CaCl₂

Fig. 4.11 shows the dependence of CaCO₃ particle size with reactants concentration. Under the same ultrasonic conditions (19.5 kHz, 17.6 W, 3 min), the particle size of CaCO₃ decreased with the increasing of reactants concentration. Below 0.125 M of the reactant's concentration, the particle size of CaCO₃ decreased obviously with the increasing of the reactant concentration. However, over 0.125 M of the reactant concentration, the particle size of CaCO₃ decreased gently with the increasing of the reactant concentration.
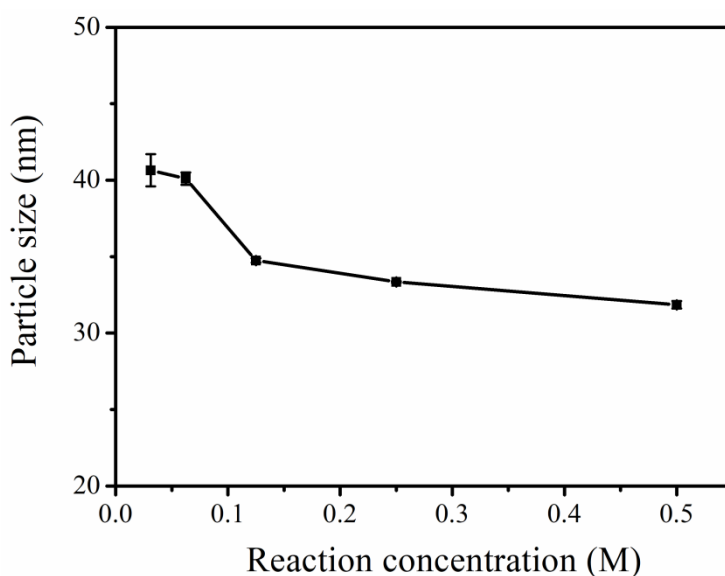

Fig. 4.11 Dependence of CaCO₃ HDS measured by QELS on reactant concentration. Conditions: 10 mL of Na₂CO₃ solutions and 10 mL of CaCl₂ solutions were sonicated at 19.5 kHz and 17.6 W for 3 min.

4.3.2.4 Effect of reaction volume

Fig. 4.12 shows that the CaCO₃ particle size decreased as the reaction volume ranged from 10 mL to 50 mL. As shown in Fig. 4.12, the smallest CaCO₃ particles (24.5 nm) were obtained with a reaction volume of 30 mL. Over 30 mL of the reaction volume, the particle size of CaCO₃ increased with increasing reaction volume. The smallest particle size of CaCO₃ can be explained by the optimal cavitation efficiency, namely, optimum ratio of ultrasonic power to liquid

volume.[29, 30] Under the optimal reaction volume, the number of cavitation bubbles generated by sonication is greater, therefore, the increasing number of nucleation sites provided by cavitation bubbles increases the nucleation rate and reduce the particle size of $CaCO_3$. The same results were observed in the FESEM (Fig. 4.13), namely, the $CaCO_3$ particles obtained at the reaction volume of 30 mL were smaller than those obtained at 20 mL. Fig. 4.14 shows the XRD patterns of $CaCO_3$ particles prepared by sonication in different reaction volumes (20 mL and 30 mL). The peak intensity of the 104 crystal plane decreased as the reaction volume increased from 20 mL to 30 mL. This was because the amount of hydroxyl radicals produced increased owing to the increasing cavitation efficiency in 30 mL, and therefore, the growth inhibitory of crystals was enhanced.[20-23]
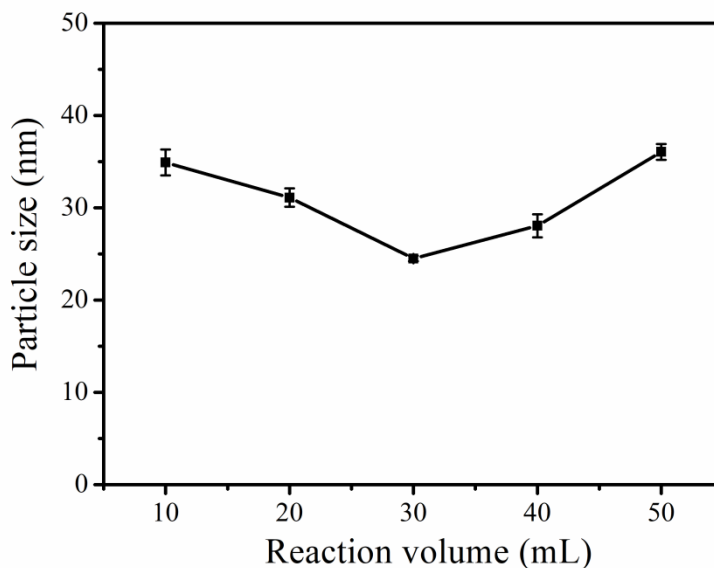

Fig. 4.12 Dependence of CaCO₃ HDS measured by QELS on reaction volumes. Conditions: 0.5 M Na₂CO₃ solutions and 0.5 M CaCl₂ solutions were sonicated at 19.5 kHz and 17.6 W for 3 min.
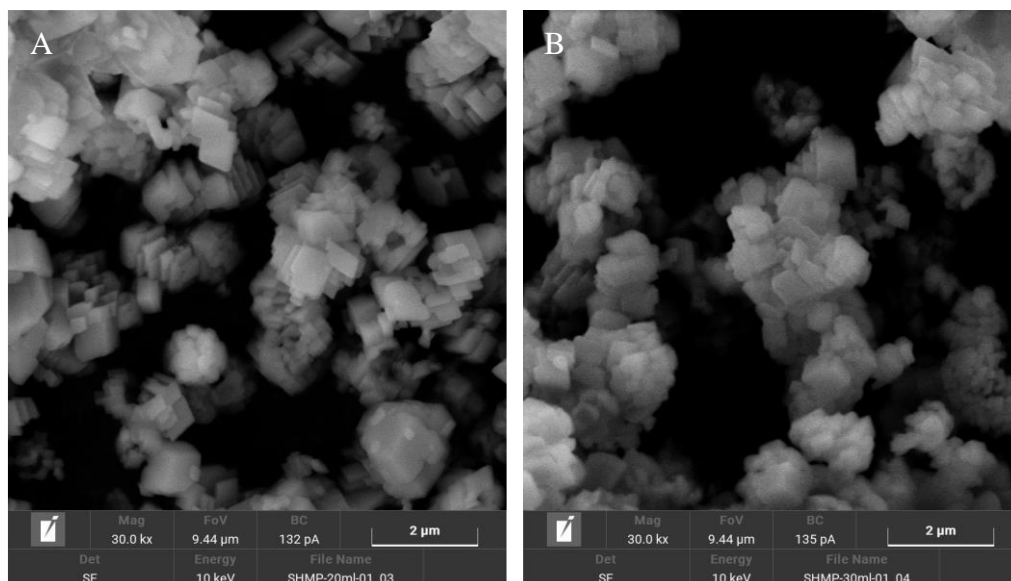
Fig. 4.13 FESEM images of CaCO₃ particles by sonication in the reaction volume of 20 mL (A) and 30 mL (B). Conditions: 0.5 M Na₂CO₃ and 0.5 M CaCl₂ were sonicated at 19.5 kHz and 17.6 W for 3 min.

Fig. 4.14 XRD spectrum of CaCO₃ particles by sonication in the reaction volume of 20 mL (A) and 30 mL (B). Conditions: 0.5 M Na₂CO₃ and 0.5 M CaCl₂ were sonicated at 19.5 kHz and 17.6 W for 3 min.
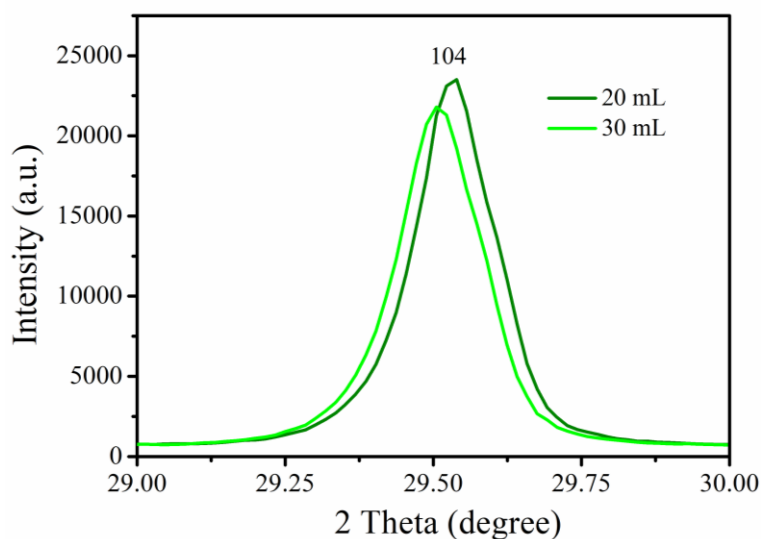
4.4 Conclusions

$CaCO_3$ particles were prepared under the action of low-frequency ultrasound. The effects of reactant concentration, ultrasonic time, ultrasonic power and reactant volume on the particle size of the prepared $CaCO_3$ were investigated. Compared to stirring, small $CaCO_3$ particles were obtained with low-frequency ultrasonic. It had no significant effect of ultrasonic time on $CaCO_3$ particle size. They had optimal ultrasonic power and optimal reaction volume under sonication. The mechanism of preparing $CaCO_3$ under the action of ultrasound was discussed. The nucleation rate of $CaCO_3$ by cavitation bubbles and the inhibition of crystal growth by hydroxyl radicals were discussed respectively. The surface of the cavitation bubble provided active sites for $CaCO_3$ nucleation resulting in the nucleation rate increasing. In addition, the generated hydroxyl radicals by sonication interacted with Ca^{2+} ions to inhibit the growth of crystals.

References

[1] S. Sonawane, S. Shirsath, P. Khanna, S. Pawar, C. Mahajan, V. Paithankar, V. Shinde, C. Kapadnis, An innovative method for effective micro-mixing of CO_2 gas during synthesis of nano-calcite crystal using sonochemical carbonization, Chemical Engineering Journal, 143 (2008) 308-313.

[2] M. Fuji, T. Shin, H. Watanabe, T. Takei, Shape-controlled hollow silica nanoparticles synthesized by an inorganic particle template method, Advanced Powder Technology, 23 (2012) 562-565.

[3] Y. Nakashima, C. Takai, H. Razavi-Khosroshahi, W. Suthabanditpong, M. Fuji, Synthesis of ultra-small hollow silica nanoparticles using the prepared amorphous calcium carbonate in one-pot process, Advanced Powder Technology, 29 (2018) 904-908.

[4] Y.-Q. Niu, J.-H. Liu, C. Aymonier, S. Fermani, D. Kralj, G. Falini, C.-H. Zhou, Calcium carbonate: controlled synthesis, surface functionalization, and nanostructured materials, Chemical Society Reviews, 51 (2022) 7883-7943.

[5] M. He, E. Forssberg, Y. Wang, Y. Han, Ultrasonication-assisted synthesis of calcium carbonate nanoparticles, Chemical Engineering Communications, 192 (2005) 1468-1481.

[6] Y. Kojima, M. Kanai, N. Nishimiya, Synthesis of novel amorphous calcium carbonate by sono atomization for reactive mixing, Ultrasonics Sonochemistry, 19 (2012) 325-329.

[7] S. Kirboga, M. Oner, E. Akyol, The effect of ultrasonication on calcium carbonate crystallization in the presence of biopolymer, Journal of Crystal Growth, 401 (2014) 266-270.

[8] B. Njegić Džakula, J. Kontrec, M. Ukrainczyk, S. Sviben, D. Kralj, Polymorphic composition and morphology of calcium carbonate as a function of ultrasonic irradiation, Crystal Research and Technology, 49 (2014) 244-256.

[9] Y. Kojima, K. Yamaguchi, N. Nishimiya, Effect of amplitude and frequency of ultrasonic irradiation on morphological characteristics control of calcium carbonate, Ultrasonics Sonochemistry, 17 (2010) 617-620.

[10] J.A. Juhasz-Bortuzzo, B. Myszka, R. Silva, A.R. Boccaccini, Sonosynthesis of vaterite-type calcium carbonate, Crystal Growth & Design, 17 (2017) 2351-2356.

[11] R.F. Contamine, A. Wilhelm, J. Berlan, H. Delmas, Power measurement in sonochemistry, Ultrasonics Sonochemistry, 2 (1995) S43-S47.

[12] A. Ghadami Jadval Ghadam, M. Idrees, Characterization of $CaCO_3$ nanoparticles synthesized by reverse microemulsion technique in different concentrations of surfactants, Iranian Journal of Chemistry and Chemical Engineering, 32 (2013) 27-35.

[13] V.S. Nalajala, V.S. Moholkar, Investigations in the physical mechanism of sonocrystallization, Ultrasonics Sonochemistry, 18 (2011) 345-355.

[14] J. Lee, M. Ashokkumar, S.E. Kentish, Influence of mixing and ultrasound frequency on antisolvent crystallisation of sodium chloride, Ultrasonics Sonochemistry, 21 (2014) 60-68.

[15] S.L. Hem, The effect of ultrasonic vibrations on crystallization processes, Ultrasonics, 5 (1967) 202-207.

[16] K. Ohsaka, E.H. Trinh, Dynamic nucleation of ice induced by a single stable cavitation bubble, Applied Physics Letters, 73 (1998) 129-131.

[17] S. Gopi, V. Subramanian, K. Palanisamy, Aragonite–calcite–vaterite: A temperature influenced sequential polymorphic transformation of $CaCO_3$ in the presence of DTPA, Materials Research Bulletin, 48 (2013) 1906-1912.

[18] M.E.-S.I. Saraya, H. Rokbaa, Preparation of vaterite calcium carbonate in the form of spherical nano-size particles with the aid of polycarboxylate superplasticizer as a capping agent, American Journal of Nanomaterials, 4 (2016) 44-51.

[19] A.T. Nagaraja, S. Pradhan, M.J. McShane, Poly (vinylsulfonic acid) assisted synthesis of aqueous solution stable vaterite calcium carbonate nanoparticles, Journal of Colloid and Interface Science, 418 (2014) 366-372.

[20] C.-L. Yao, W.-H. Xu, A.-M. Ding, J.-M. Zhu, Sucrose/bovine serum albumin mediated biomimetic crystallization of calcium carbonate, Journal of Chemical Sciences, 121 (2009) 89-93.

[21] D.J. Cooke, R.J. Gray, K.K. Sand, S.L.S. Stipp, J. Elliott, Interaction of ethanol and water with the {1014} surface of calcite, Langmuir, 26 (2010) 14520-14529.

[22] K. Sand, M. Yang, E. Makovicky, D.J. Cooke, T. Hassenkam, K. Bechgaard, S. Stipp, Binding of ethanol on calcite: The role of the OH bond and its relevance to biomineralization, Langmuir, 26 (2010) 15239-15247.

[23] J. Nielsen, K. Sand, C. Pedersen, L. Lakshtanov, J. Winther, M. Willemoës, S. Stipp, Polysaccharide effects on calcite growth: the influence of composition and branching, Crystal Growth & Design, 12 (2012) 4906-4910.

[24] A. Sivakumar, P. Shailaja, M. Nandhini, S.S.J. Dhas, R.S. Kumar, A.I. Almansour, N. Arumugam, S. Chakraborty, S.M.B. Dhas, Ternary switchable phase transition of $CaCO_3$ by shock waves, Ceramics International, 48 (2022) 8457-8465.

[25] M.E. Hoque, M. Shehryar, K.N. Islam, Processing and characterization of cockle shell calcium carbonate ($CaCO_3$) bioceramic for potential application in bone tissue engineering, Material Science & Engineering, 2 (2013) 132.

[26] X. Liu, Z. Wu, M. Manzoli, L. Jicsinszky, R. Cavalli, L. Battaglia, G. Cravotto, Medium-high frequency sonication dominates spherical-SiO_2 nanoparticle size, Ultrasonics Sonochemistry, 90 (2022) 106181.

[27] M. Takasaki, Y. Kimura, T. Yamazaki, Y. Oaki, H. Imai, 1D oriented attachment of calcite nanocrystals: formation of single-crystalline rods through collision, RSC Advances, 6 (2016) 61346-61350.

[28] X. Song, L. Zhang, Y. Cao, J. Zhu, X. Luo, Effect of pH and temperatures on the fast precipitation vaterite particle size and polymorph stability without additives by steamed ammonia liquid waste, Powder Technology, 374 (2020) 263-273.

[29] T. Mason, J. Lorimer, D. Bates, Quantifying sonochemistry: casting some light on a 'black art', Ultrasonics, 30 (1992) 40-42.

[30] M. Lim, M. Ashokkumar, Y. Son, The effects of liquid height/volume, initial concentration of reactant and acoustic power on sonochemical oxidation, Ultrasonics Sonochemistry, 21 (2014) 1988-1993.

Chapter 5: Using Calcium Carbonate Nanoparticles as a Template, Ultrasonic Preparation of Hollow Mesoporous Silica Nanoparticles for Loading and Release of Voriconazole.

Abstract

CaCO$_3$ nanoparticles (nano-CaCO$_3$) were prepared as nano-templates with CaCl$_2$ and Na$_2$CO$_3$ solutions by 19.5 kHz sonication. Hollow mesoporous silica nanoparticles (HMSNs) were synthesized by double-template method with nano-CaCO$_3$ as the hard template and hexadecyl trimethyl ammonium bromide (CTAB) as the soft template. Transmission Electron Microscopy (TEM) showed that the prepared HMSNs possessed hollow structures and the particle size of the obtained HMSNs nanoparticles was between 110-120 nm. The nitrogen adsorption isotherm showed that the HMSNs have a high surface area (401.57 m^2/g), pore volume (0.11 cm^3/g), and uniform pore size (2.22 nm) that facilitated the effective encapsulation of antifungal drug voriconazole (VOR) within HMSNs. The loading efficiency (wt%) of VOR on the HMSNs was 7.96%, and the total VOR release amount of VOR-HMSNs material was 71.40% at 480 min. The Korsmeyer-Peppas and Higuchi kinetic model confirmed that the release mechanism of HMSNs nanoparticles followed Fickian diffusion at pH 7.4 and 37°C. Moreover, the cumulative VOR release at 42°C (86.05%) was higher than that at 37°C (71.40%). The cumulative release amount of VOR from the VOR-HMSNs material was 92.37% at pH 5.8. A Korsmeyer-Peppas kinetic model shows that the VOR molecules pass through the pore of the silica shell with Fickian diffusion mechanism at pH 5.8.

5.1   Introduction

Hollow mesoporous silica nanomaterials (HMSNs) have received extensive attention due to their potentially important applications in catalysis, encapsulation of biomolecules, sustained drug release, and gene delivery.[1-3] Especially in the pharmaceutical field, as the drug carriers HMSNs improve the efficacy of drug therapy.[2, 3] Drugs can be loaded in the hollow structure of silica to perform slow and sustained drug release. At present, the template method, emulsion method, and spray drying methods are commonly used to synthesize HMSNs.[4-6] Compared with the template method, the synthesis conditions of the emulsion method are difficult to control, and the particle sizes of samples prepared by the spray drying method are larger.[7] Therefore, the template method is the main method for

preparing HMSMs, such as emulsion templates, vesicle templates, polymer latex templates, SiO_2 spheres templates, and carbon spheres templates, etc.[8, 9] Compared with organic templates, inorganic materials are more suitable for the template of HMSNs due to the uniform particle size and less toxicity. $CaCO_3$ nanoparticles have shown great promise as the template for the synthesis of HMSNs since nano-$CaCO_3$ particles can be easily removed by acid treatment.[10, 11]

In the past decades, hollow silica has been prepared with ultrasound-generated bubbles as templates since a long reaction time (2-24 h) was required for preparation with stirring.[12-15] Rana et al. used ultrasound-mediated supramolecular template technology to prepare hollow mesoporous silica.[12] Surfactants and silicate species cooperatively assembled near the air-water interface of cavitation bubbles to form foam-like morphological templates, resulting in hollow mesoporous silica with a diameter of 50–500 nm. In 2006, 0.2-5.0 μm hollow silica microspheres were prepared with $NaSO_4C_{12}H_{25}$ and $(CH_3CH_2CH_2)_4N(Br)$ in solutions by sonication.[13] In 2018, 3.5 ~ 5 μm hollow silica was synthesized with templates of cavitation bubbles, a structure-directing agent of pluronic F127 ($EO_{106}PO_{70}EO_{106}$), a silicon source of orthoethyl silicate (TEOS), and an expansion agent of 1,3,5-trimethylbenzene.[14] In 2019, Jiang et al. synthesized 200 nm hollow mesoporous silica spheres by using an ultrasound-assisted selective etching method.[15] Importantly, the hydrolysis time of TEOS under sonication was greatly shortened.[12, 14] Nevertheless, the hollow silica obtained by sonication mostly belongs to submicron and micron and the particle size distribution is not uniform. In terms of particle size and distribution, the benefits of sonication are not fully exploited.[16]

Nano-$CaCO_3$ templates were prepared by sonication with $CaCl_2$ and Na_2CO_3 solutions using a 19.5 kHz ultrasonic cup. Using the same ultrasonic device, subsequently, mesoporous silica with core-shell structure was prepared with the nano-$CaCO_3$ templates obtained previously and Hexadecyl trimethyl ammonium bromide (CTAB) as a mesoscopic structure-directing agent at alkaline condition. Structurally complete HMSNs were obtained by removing the hard template of nano-$CaCO_3$ by acid treatment. The antifungal drug voriconazole (VOR) was selected as a model drug to investigate the drug loading and sustained release from VOR-loaded HMSNs. The effects of temperature and pH on drug release kinetics were

investigated.

5.2 Materials and methods

5.2.1 Materials

Calcium chloride (CaCl$_2$, 93%, Alfa Aesar), sodium carbonate monohydrate (Na$_2$CO$_3 \cdot$H$_2$O, ≥99.5%, Sigma-Aldrich), sodium hexametaphosphate ((NaPO$_3$)$_6$, Alfa Aesar), tetraethyl orthosilicate (TEOS, 98.0%, Aldrich), ethanol (EtOH, ≥99.8%, Sigma-Aldrich), ammonium hydroxide (NH$_4$OH, 30.0%, Carlo Erba), CTAB (＞98.0%, Tokyo Chemical Industry Co., Ltd.), hydrochloric acid (HCl, 36% w/w, Alfa Aesar), VOR (≥98% (HPLC), Sigma), sodium hydroxide (NaOH, 97%, Thermo Scientific), potassium hydrogen phosphate (K$_2$HPO$_4$, 98%, Alfa Aesar) and potassium dihydrogen phosphate (KH$_2$PO$_4$, 98%, Alfa Aesar) were used without additional purification.

5.2.2 Methods

Ultrasonic cup-horn apparatus (home-made, 19.5 kHz) was used to prepare nano-CaCO$_3$ and HMSNs. Muffle furnace (Nabertherm, Germany) was used to remove CTAB. Centrifuge (Allegra 64R Benchtop Centrifuge, Beckman Coulter, Italy) was used to collect nanoparticles Ultraviolet-visible Spectrophotometer (UV, Agilent Technologies Cary 60 UV-Vis, USA) was used to measure the absorbance of VOR. The ultrasonic powers delivered were determined calorimetrically with water as heating media and all ultrasonic power mentioned below refers to the power measured calorimetrically.[17]

5.2.2.1   Synthesis of CaCO$_3$ Nanoparticles

15 mL of 0.5 M CaCl$_2$ solution were added into ultrasonic cup-horn. The ultrasonic cup-horn was turned on (19.5 kHz; 55 W) and the 15 mL of 0.5 M Na$_2$CO$_3$ solution were added into the CaCl$_2$ solution. 3 min later the ultrasonic cup-horn was turned off and the CaCO$_3$ precipitate was collected (centrifuge 5000 rpm; wash 3 times with distilled water). The obtained CaCO$_3$ nanoparticles were dried by freeze-

drying.

5.2.2.2 Synthesis of HMSNs

The obtained nano-$CaCO_3$ was used as the template to prepare HMSNs. 30 mL of distilled water was added into the ultrasonic cup and the ultrasonic reactor (19.5 kHz, 17.6 W) was turned on. 0.4 g of $CaCO_3$ was added into the ultrasonic cup. After 3 min, 0.03 g of $(NaPO_3)_6$ was added as dispersant into the ultrasonic cup to disperse the formed $CaCO_3$ particles. 2 min later, 22.5 mL of EtOH was injected into the above $CaCO_3$ dispersion and then the power of ultrasonic cup was regulated to 33.9 W for 2 min sonication. 0.2 g of CTAB as the pore-directing agent was added with sonication for 5 min. The catalyst of NH_4OH (0.45 mL) was added to the reaction solution. After a 2 min sonication, 0.25 mL of TEOS were added into the reaction solution, which was continued to be sonicated for 40 min. Finally, the sample of $CaCO_3$@mesoporous silica ($CaCO_3$@$mSiO_2$) was collected by centrifuge and washed 3 times with EtOH, and then washed 3 times with distilled water. The sample of $CaCO_3$@$mSiO_2$ was dried by freeze-drying. To remove the CTAB, $CaCO_3$@$mSiO_2$ was calcined at 550°C for 6 h in air. The hard template of nano-$CaCO_3$ was removed to obtain HMSNs by using 100 mL HCl (1 mol/L) at room temperature overnight with stirring. The obtained HMSNs were washed with distilled water 3 times and dried with freeze-drying.

5.2.3 Characterization

Field emission scanning electron microscope (FESEM) measurements were performed on a Tescan S9000G FESEM 3010 microscope (30 KeV) equipped with a high-brightness Schottky emitter. Powder samples were deposited on a stub coated with a conducting adhesive and inserted in the chamber by a fully motorized procedure for analysis. Transmission Electron Microscopy (TEM) was employed on FEI FEI talosf200s to characterize the detailed core-shell structure. The TEM sample was prepared by dipping a Cu grid coated with carbon films in sample suspension with ethanol as solvent. Porosity properties were evaluated based on the N_2 adsorption/desorption isotherms at -196°C by means of an ASAP 2460 instrument (Micromeritics), in order to determine the total specific surface area using the Brunauer-Emmett-Teller (BET) method, porous volume and average pore size were

calculated using the Barrett-Joyner-Halenda (BJH) model. The samples were either in the form of a powder or granule (ca. 0.0254 g). The Fourier transform infrared spectrometer (FT-IR) spectra (Spectrum Two, PerkinElmer, USA) were measured by a spectrometer from 500 to 4000 cm^{-1} at 2 cm^{-1} resolution with 64 scans.

5.2.4 Drug loading

The standard curve was prepared with distilled water. 10 mg of VOR were added into a 100 mL volumetric flask and distilled water as solvent was diluted to the mark to obtain 100 µg/mL stock solution. 1.5, 2.0, 2.5, 3.0, and 4.0 mL of the above VOR stock solution were placed in 10 mL volumetric flasks, respectively. Distilled water was used to make up the volume. Therefore, 15, 20, 25, 30, and 40 µg/mL of the standard solutions were obtained. The absorbance of VOR was measured at a wavelength of 256 nm.

The drug loading of VOR was performed with distilled water as the loading solvent. 20 mg of VOR were dispersed in 50 mL of distilled water by sonication. Then 100 mg of HMSNs was dispersed in the above dispersions with stirring at 200 rpm. After 24 h agitation, the VOR-loaded HMSNs (VOR-HMSNs) were centrifuged at 15,000 rpm for 10 min, and then the precipitate was washed once with distilled water to remove VOR on the surface of VOR-HMSNs. The supernatants were collected and measured by UV-Vis spectroscopy. To determine drug loading content, the amount of VOR in the HMSNs carrier was calculated by subtracting the mass of VOR in the supernatant from the total mass of the drug's initial amount by analysis with UV-Vis at 256 nm. The loading efficiency of the HMSNs using the equation (3-2):[18, 19]

5.2.5 Drug release

The standard curve was prepared with phosphate buffer (PB) solutions. According to the aforementioned method, 10 mg of VOR were solved in PB solutions and placed into a 100 mL volumetric flask. A concentration of 100 µg/mL stock solution was obtained with PB solution injected into the volumetric flask to a constant volume. 1.0, 1.5, 2.0, 2.5, and 3.0 mL of VOR stock solution were pipetted

to 10 mL volumetric flasks and PB solutions were filled to the mark of 10 mL, correspondingly, 10, 15, 20, 25, and 30 µg/mL of test solutions were obtained. The absorbances of the test solutions were measured at the maximum absorption wavelength, respectively, and the PB solution served as the blank control solution.

20 mg of VOR-HMSNs was dispersed in 20 mL of PB solution and then the solution was stirred with a magnetic stirrer at 37°C and 200 rpm. 3 mL of sample was periodically extracted during 480 min agitation and 3 mL of the fresh PB medium was added immediately after sampling. The VOR concentration in the solution was measured by UV-Vis spectroscopy and calculated according to the pre-established calibration curve, and then the cumulative release amounts and the cumulative release rate (CR) were calculated according to the equations (5-1) and (5-2):

$$m_n = (C_1 + C_2 + C_{n-1}) \times 3 + C_n \times 20 \qquad (5\text{-}1)$$

$$CR = \frac{m_n}{m_0} \times 100\% \qquad (5\text{-}2)$$

C_n is the mass concentration (mg/mL) of VOR in the nth sampling, m_n is the cumulative release mass (mg) of the nth sampling VOR, and m_0 is the total mass (mg) of the loaded drug. Drug release curves were drawn according to CR.

5.3   Results and discussion

Fig. 5.1 shows the FESEM image and particle size distribution of the synthesized nano-CaCO$_3$. Fig. 5.1A shows that nano-CaCO$_3$ particles were obtained. Unfortunately, these CaCO$_3$ nanoparticles agglomerated very strongly. Particle size distribution of CaCO$_3$ nanoparticles (Fig. 5.1B) indicated that the particle size of CaCO$_3$ nanoparticles was between 20 and 40 nm. The particle size of CaCO$_3$ nanoparticles was measured after sonication dispersion in the presence of a dispersant. Therefore, the agglomerated CaCO$_3$ nanoparticles were redispersed with sonication in the presence of a dispersant. Thus, using the CaCO$_3$ nanoparticles as a hard template to prepare HMSNs, it was necessary to redisperse the agglomerated CaCO$_3$ nanoparticles in the presence of a dispersant and then coated them.
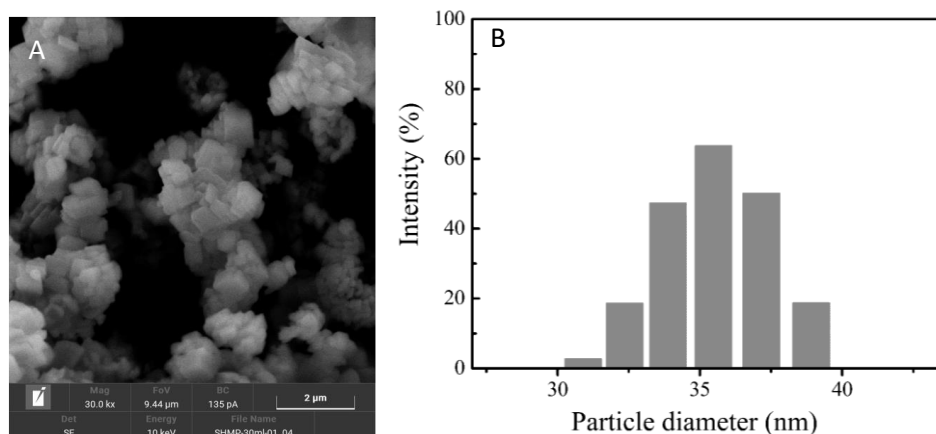
Fig. 5.1 The FESEM (A) image and particle size distribution (B) of the synthesized nano-CaCO$_3$.

The FESEM and TEM images of the prepared HMSNs were shown in Fig. 5.2. As shown in Fig. 5.2A, the prepared HMSNs have good dispersion. The particle size of the obtained HMSNs nanoparticles was between 110-120 nm. A relatively complete HMSNs structure can be seen in Fig. 5.2B, which was a hollow structure and the inner color of HMSNs was lighter. The darker color of the outer was a silica shell structure. Therefore, HMSNs were hollow nanoparticles with mesoporous silica as shells, and the empty cages can be loaded with other molecules (such as drug molecules, etc.) through the mesoporous channels (white dots) of the silica shells.
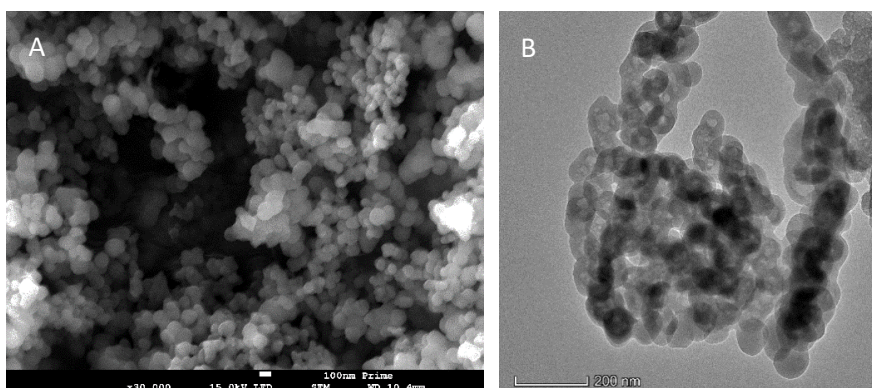

Fig. 5.2 The FESEM (A) and TEM (B) images of the prepared HMSNs. Conditions: ca. 53 mL of mixture (H$_2$O: 30.00 mL; nano-CaCO$_3$: 0.4 g; 99.8% EtOH: 22.50 mL; 30.0% NH$_4$OH: 0.45 mL; 98.0% TEOS: 0.25 mL) was sonicated at 19.5 kHz, 33.9 W for 40 min.

FT-IR spectrum of the $CaCO_3@mSiO_2$ and HMSNs were shown in Fig. 5.3. As can be seen from $CaCO_3@mSiO_2$, the absorption band at 1418, 874 and 713 cm^{-1} could be attributed to the anti-symmetric stretching vibration of C–O, CO_3^{2-} external plane bending vibration and O–C–O internal plane bending vibration.[20] The strong and broadband at 1084 cm^{-1} was assigned to CO_3^{2-} symmetric stretching vibration and Si–O–Si asymmetric stretching vibration.[20, 21] 949 cm^{-1} can be attributed to the silanol group.[21] In addition, the absorption band at 798 cm^{-1} could be classified as symmetric stretching vibration of Si–O–Si.[21] However, at the FT-IR spectrum of the HMSNs, the absorption bands of $CaCO_3$ at 1418, 874 and 713 cm^{-1} disappeared. Therefore, the $CaCO_3$ nano-cores were completely removed.
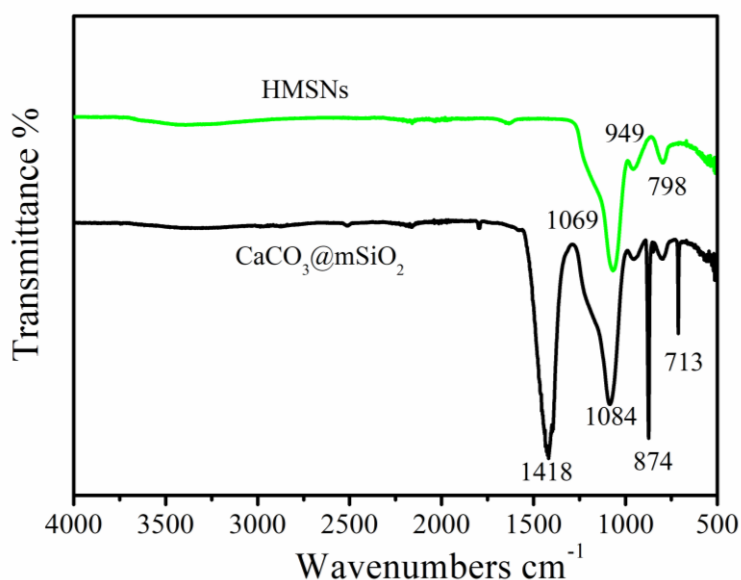

Fig. 5.3 FT–IR spectrum of the $CaCO_3@SiO_2$ and HMSNs.

The nitrogen adsorption-desorption isotherm and Barret–Joyner–Halenda (BJH) pore size distribution of HMSNs were shown in Fig. 5.4. According to the IUPAC classification, on the basis of the hysteresis loop of the isotherm (see Fig. 5.4A) the HMSNs material was a typical type IV N_2 gas adsorption isotherm. The isotherms indicate that the adsorption of N_2 gas on the surface of silica particles was continuously increased at lower relative pressures. At higher relative pressure, the increase of N_2 adsorption was due to the adsorption of gas in the pores and voids. The surface area and pore volume of the HMSNs material were 401.57 m^2/g and

0.11 cm^3/g, respectively. It demonstrated that HMSNs had a larger cavity structure, which was more conducive to drug loading. According to the pore size distribution curve (Fig. 5.4B), it can be concluded that the average pore size distribution of the HMSNs material was 2.22 nm. It was further proved that the HMSNs formed with CTAB had a better pore size to load drug molecules into HMSNs materials.
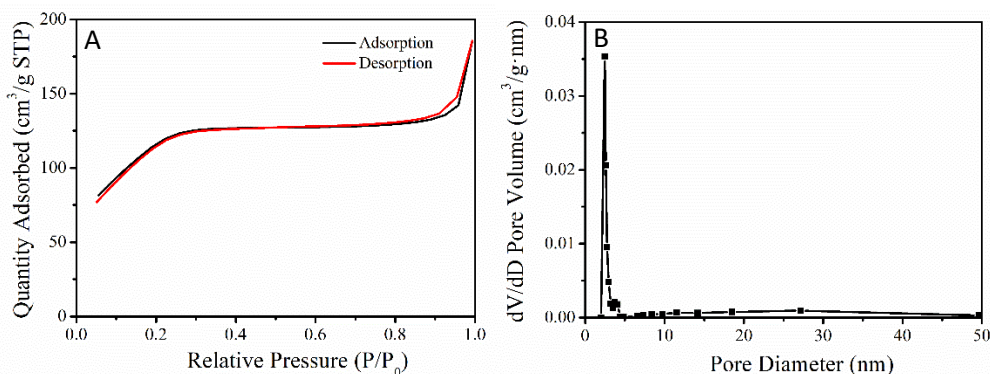

Fig. 5.4 The nitrogen adsorption-desorption isotherm (A) and Barret–Joyner–Halenda (BJH) pore size distribution (B) of HMSNs.

5.3.1 Drug loading

Using distilled water as a blank control, the absorbance A of VOR was measured at a wavelength of 256 nm. The absorbance corresponding to the concentration of VOR was listed in Table 5.1. The UV absorption spectrum and standard curve of VOR were shown in Fig. 5.5. It can be seen from the figure that there was a good fit of the standard curve. The standard curve equation was obtained by the linear regression analysis on the concentration C value with the A value (equation 5-3). The R^2 value is 0.99987, which meets the experimental requirements.

$$Y = 0.05373 + 0.02447X \tag{5-3}$$

where Y is the absorbance at 256 nm and X is the concentration of VOR expressed in µg/g.

By measuring the absorbance of the supernatant of the remaining solution,

the amount of remaining VOR was calculated by using the standard curve equation. The drug loading of HMSNs (7.96%) was calculated using equation 1 and equation 2.

Table 5.1 The absorbance corresponding to the concentration of VOR.

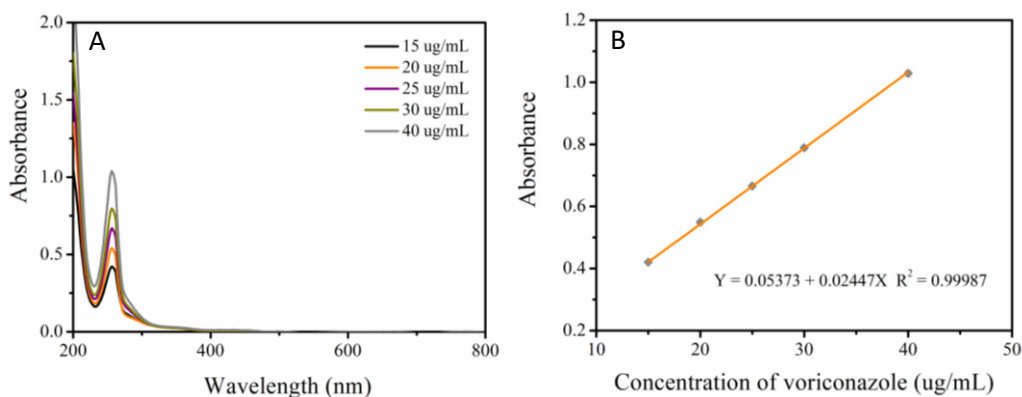| VORconcentration (µg/mL)	Absorbance 1	Absorbance 2	Average absorbance	error
15	0.422	0.419	0.421	0.001
20	0.558	0.542	0.550	0.008
25	0.669	0.662	0.666	0.004
30	0.797	0.781	0.789	0.008
40	1.039	1.019	1.029	0.010

Fig. 5.5 The UV absorption spectrum (A) and standard curve (B) of VOR.

FT-IR was used to further prove that VOR was loaded into HMSNs material. In Fig. 5.6A, the aromatic C=C stretching vibrations and the methylene C–H in-plane bending vibration peak of the drug-loaded VOR-HMSNs material were observed at 1503 cm^{-1} and 1410 cm^{-1}, respectively.[22] These characteristic peaks appear at the same positions in the FT-IR spectrum of pure VOR (Fig. 5.6B). Therefore, VOR was successfully loaded into the HMSNs.
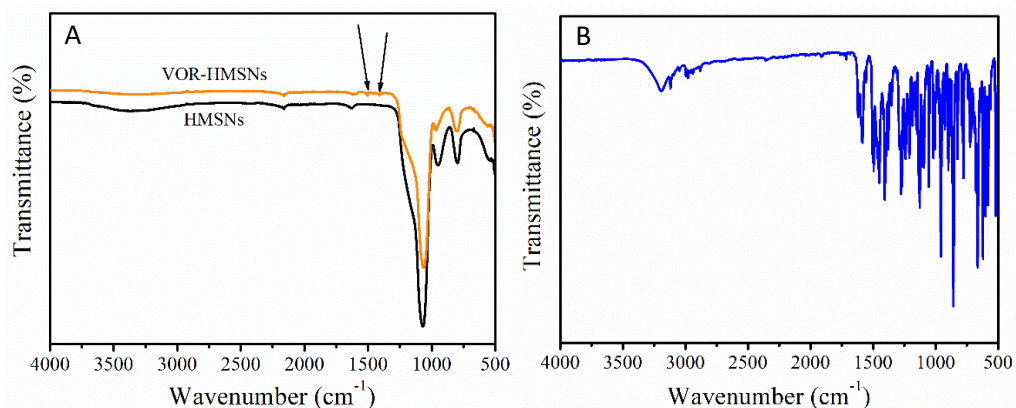
Fig. 5.6 The FT–IR spectrum of the VOR-HMSNs (A) and pure VOR (B).

5.3.2 VOR release from VOR-HMSNs

Using PB solution as the blank control solution, the absorbance A values of the test substances were measured at the maximum absorption wavelength, respectively. A suitable standard curve equation was obtained by performing linear regression analysis on the absorbance value A with concentration C. The absorbance corresponding to the concentration of VOR was listed in Table 5.2. The UV absorption spectrum and standard curve of VOR are shown in Fig. 5.7. The standard curve equation was obtained by the linear regression analysis on the concentration C value with the A value (equation 5-4). The R^2 value is 0.99951, which meets the experimental requirements.

$$y = 0.08234 + 0.02282x \quad R^2 = 0.99951 \tag{5-4}$$

where y is the absorbance at 256 nm and x is the concentration of VOR expressed in μg/g.

The values of absorbance were measured with the take-out samples at 5, 10, 20, 30, 45, 60, 120, 180, 240, and 480 min, respectively. Then the drug concentration was calculated according to the standard curve of VOR in PB to obtain the cumulative release amount of the VOR.

122

Table 5.2 The absorbance corresponding to the concentration of VOR.

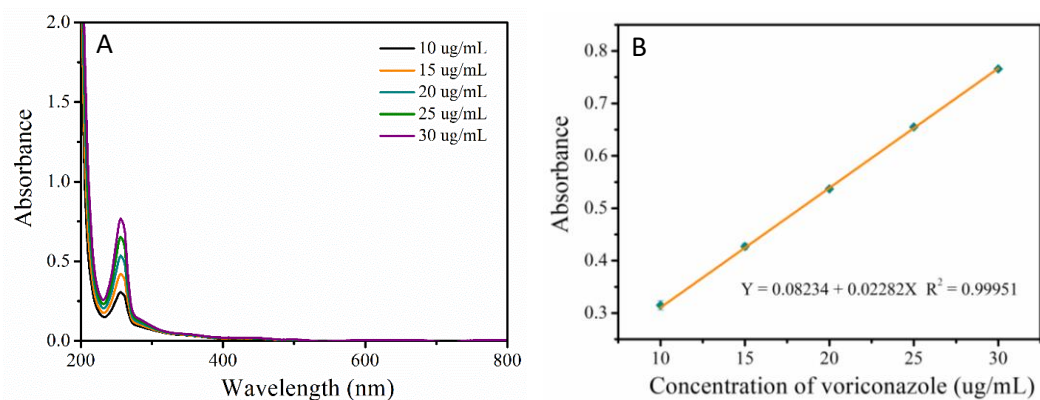| VOR concentration (µg/mL)	Absorbance 1	Absorbance 2	Average absorbance	error
10	0.324	0.306	0.315	0.009
15	0.433	0.421	0.427	0.006
20	0.539	0.535	0.537	0.002
25	0.657	0.653	0.655	0.002
30	0.763	0.768	0.766	0.002

Fig. 5.7 The UV absorption spectrum (A) and standard curve (B) of VOR.

Fig. 5.8 shows the drug release curve of VOR from VOR-HMSNs material under pH 7.4 at 37°C. As shown in Fig. 5.8, the VOR release from VOR-HMSNs material was 51.67% at the first stage (5 min). There was an obvious burst release which was mainly due to the sudden gushing of the VOR from the opening of the mesoporous silica channels at the first point. The release rate decreased after 30 min. The drug total release amount of VOR from VOR-HMSNs material was 71.40% at 480 min.

Fig. 5.8 shows the drug release curve of VOR-HMSNs material under pH 7.4. The drug release of the VOR-HMSNs material was 51.67% when the drug was released at the first point (5 min). There was an obvious burst release phenomenon. The burst release at the first point was mainly due to the sudden gushing of the VOR from the opening of the mesoporous silica channels. VOR-HMSNs material release rate decreased after 30 min. The drug total release amount of VOR-HMSNs material
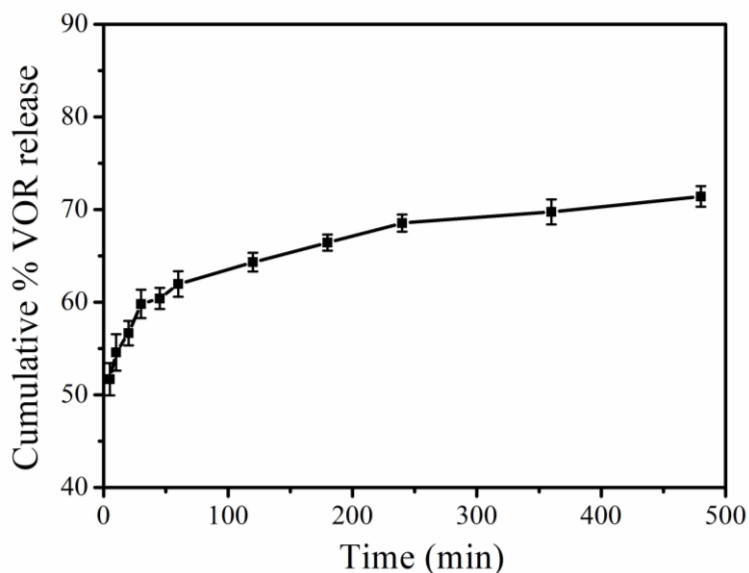
was 71.40% at 480 min.

Fig. 5.8 The drug release curve of VOR-HMSNs material.

5.3.3 Kinetic studies of drug release

The study of drug release kinetics has great significance for understanding the drug release mechanism and predicting the release time of host drugs in vitro and vivo. The release mechanism and kinetic release rate of VOR in HMSNs nanoparticles were studied mathematically by using the zero-order, first-order, Higuchi, and Korsmeyer-Peppas models.[23-25] A zero-order model describes a system in which the rate of drug release is independent of its concentration and is represented by the equation 3-5. Q_t is the amount of drug released in time t, Q_0 is the initial amount of drug in solution (in these studies, $Q_0 = 0$), and k_0 is the zero-order rate constant. The k_0 value is obtained from the slope of a linear curve of percent cumulative drug release versus time.

A first-order kinetic model describes the release of a system in which the release rate is concentration-dependent and can be expressed with equation 3-6. C_t is the concentration of drug released within time t, C_0 is the initial

concentration of drug present in the HMSNs, and k_1 is the first-order rate constant. The value of k_1 was calculated from the slope of the linear curve of $\log cumulative\%$ percent drug residue over time.

The Higuchi model describes drug release from an insoluble matrix as the square root of a time-dependent process based on Fickian diffusion. In general, the Higuchi model can be expressed with equation 3-7. k_H is the Higuchi constant. The value of k_H was taken from the slope of the linear curve of the cumulative percent drug release versus the square root of time.

Korsmeyer derived a simple relation describing drug release from polymeric systems. The logarithmic form of the Korsmeyer-Peppas model is represented by the equation 3-8. k is the kinetic constant and n is the diffusion index, a measure of the primary mechanism of drug release. The values of n and k were calculated from the slope and intercept of the linear plot of $\log cumulative\%$ percent drug release versus $\log time$. In the Korsmeyer-Peppas model, the n value is used to characterize the different release mechanisms of the drug. In the case, of cylindrical shaped matrices, n ≤ 0.45 corresponds to a Fickian diffusion mechanism, 0.45 < n < 0.89 to anomalous (non-Fickian) diffusion, n = 0.89 to case II (relaxational) transport, and n > 0.89 to super case II transport.[26] The nonlinear fitting data of the model are shown in Fig. 5.9, and the parameter values are shown in Table 5.3.

According to the nonlinear fitting data of the models shown in Table 5.3, the correlation coefficient R^2 of the Higuchi and Korsmeyer-Peppas models is greater than that of the zero-order and first-order models. Therefore, the nonlinear fitting of the Korsmeyer-Peppas model was studied. Table 5.3 shows that the corresponding n value of the Korsmeyer-Peppas model is 0.070. According to the n value of the Korsmeyer-Peppas model, the diffusion mechanism corresponds to Fickian diffusion mechanism with the n ≤ 0.45. Therefore, VOR release from HMSNs in the PB solution with pH 7.4 follows the Fickian release mechanism. The Higuchi kinetic model was investigated to determine the Fickian release mechanism of HMSNs at pH 7.4. Results showed that the correlation coefficient (R^2) of the Higuchi model for VOR release from HMSNs nanoparticles at pH 7.4 was higher than that of the zero-order and first-order models. Thus, it was confirmed that the release mechanism of HMSNs nanoparticles at pH 7.4 followed Fickian diffusion. Therefore,

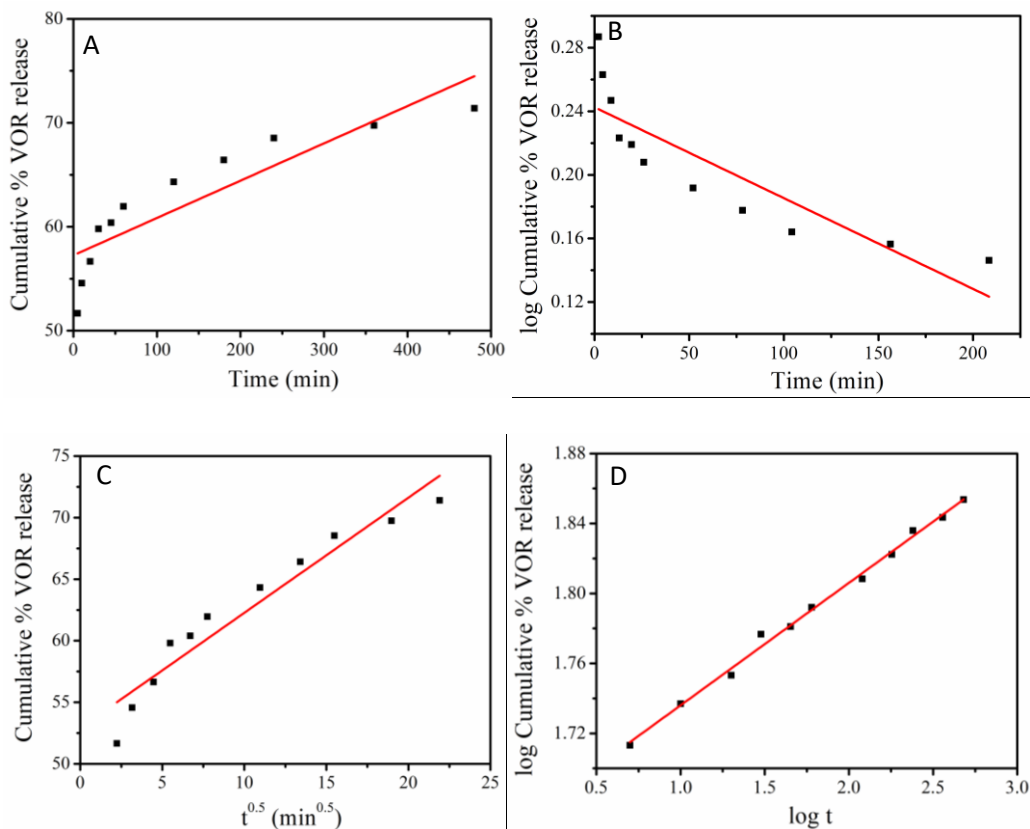the VOR was released from the HMSNs material through a diffusion process.

Fig. 5.9 Kinetic release study presenting (A) cumulative percentage release of VOR from HMSNs versus time (zero-order model plot) and linear plot of: (B) log cumulative percentage remaining of VOR from HMSNs versus time (first-order model plot) (C) cumulative percentage release of VOR from HMSNs versus square root of time (Higuchi model plot) and (D) log cumulative percentage release of VOR from HMSNs versus log time (Korsmeyer–Peppas model plot).

Table 5.3 Correlation coefficients and kinetic constants of different kinetic models for release of VOR from HMSNs.

Zero-order model		First-order model		Higuchi model		Korsmeyer–Peppas model		
k_0	R^2	K_1	R^2	k_H	R^2	k	n	R^2
0.036	0.790	0.001	0.753	0.935	0.929	46.355	0.070	0.995

5.3.4 Effect of temperature on VOR release

Since the temperature of the lesion in the human body is usually higher than normal body temperature, it is necessary to study the drug release at a higher than normal body temperature. Therefore, 42°C was chosen to investigate the release of VOR from VOR-HMSNs materials. The release profile of VOR from VOR-HMSNs material at 37°C and 42°C was shown in Fig. 5.10. In Fig. 5.10, the amount of VOR release from VOR-HMSNs material increased rapidly within the first 45 min under 37°C and 42°C. However, the rate of VOR release from VOR-HMSNs material decreased after 45 min. At 480 min, the maximum release of VOR from VOR-HMSNs was 71.40% and 86.05% at 37°C and 42°C, respectively. The cumulative VOR release at 42°C was higher than that at 37°C due to the higher molecular mobility in the solution at 42°C.[25, 27]
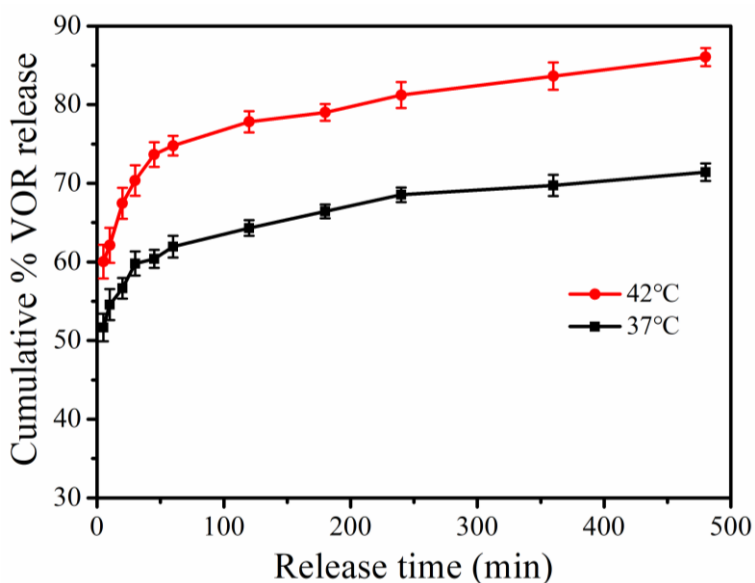

Fig. 5.10 The release of VOR from VOR-HMSN material at 37°C and 42°C.

5.3.5 Effect of pH value on VOR release

The cumulative release of VOR from VOR-HMSNs materials at pH 7.4 and 5.8 are shown in Fig. 5.11. At pH 5.8, the cumulative release amount of VOR from the VOR-HMSNs material was higher than that at pH 7.4. However, a significant VOR released from VOR-HMSNs material at pH 5.8 was 92.37% after 480 min. Results show that the acidic system was favorable for drug release. In Fig. 5.12, the values of release amount at pH 7.4 and 5.8 were well-fitted to the Korsmeyer–Peppas model. The n values of the Korsmeyer–Peppas model obtained from Fig. 5.12 are 0.070 and 0.100 for pH 7.4 and pH 5.8, respectively. Thus, VOR molecules pass through the pore of the silica shell with Fickian diffusion.
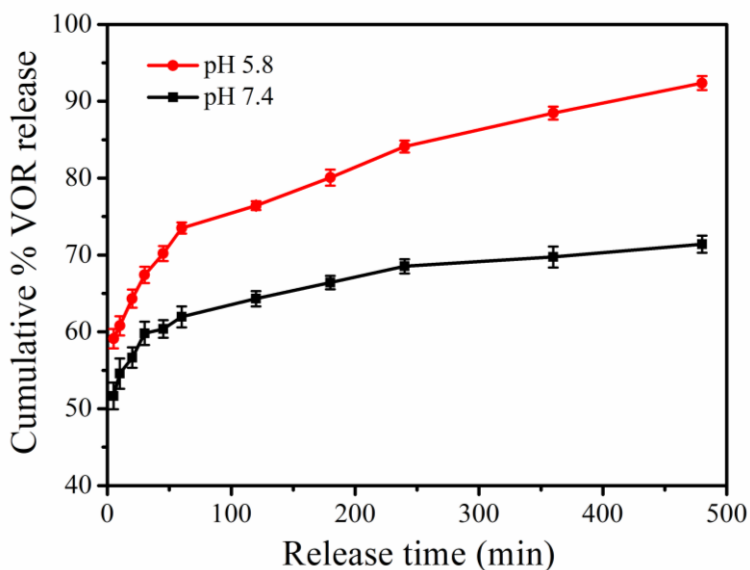

Fig. 5.11 The cumulative release of VOR from VOR-HMSNs materials at pH 7.4 and 5.8.
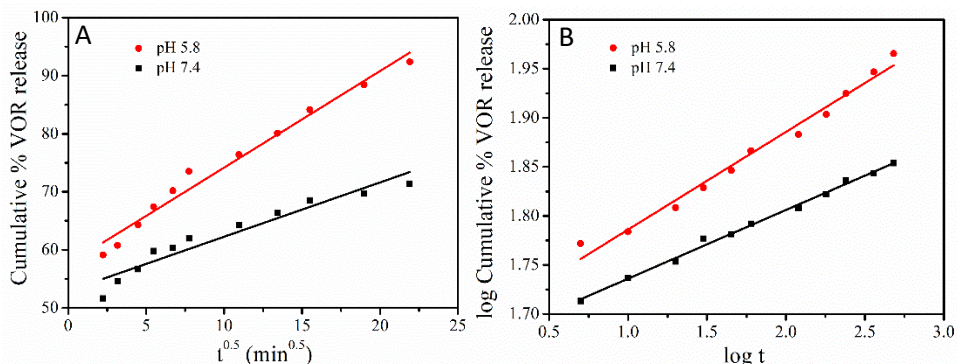
Fig. 5.12 Kinetic release study presenting (A) cumulative percentage release of VOR from VOR-HMSNs versus square root of time (Higuchi model plot) and (B) log cumulative percentage release of VOR from VOR-HMSNs versus log time (Korsmeyer–Peppas model plot) at pH 7.4 and pH 5.8.

5.4   Conclusions

The nano-$CaCO_3$ templates and HMSNs were prepared by sonication at 19.5 kHz. The agglomerated nano-$CaCO_3$ template in the dry samples can be redispersed by sonication, which is beneficial to the coating of mesoporous silica. Under alkalic conditions, a double-template (hard template and soft template) method was used to prepare HMSNs with core-shell structure. The coating time of mesoporous silica was reduced to 40 min and the uniform particles of HMSNs (110-120 nm) were obtained by sonication. Structurally complete HMSNs were obtained by removing the hard template of $CaCO_3$. The obtained HMSNs have a high surface area (401.57 m^2/g), pore volume (0.11 cm^3/g), and uniform pore size (2.22 nm) that facilitated the effective encapsulation of antifungal drug VOR within HMSNs (7.96%). The VOR release kinetics from VOR-HMSNs material at pH 7.4 conforms to Fickian diffusion. The amount of VOR released increased with increasing temperature, since the molecular mobility is temperature-dependent. Furthermore, the amount of VOR released from the VOR-HMSNs material was higher at pH 5.8 than that at pH 7.4. The maximum amount released of VOR from the VOR-HMSNs material was 92.37% at 480 min.

References

[1] J. He, X. Li, D. Evans, X. Duan, C. Li, A new support for the immobilization of penicillin acylase, Journal of Molecular Catalysis B: Enzymatic, 11 (2000) 45-53.

[2] J. Liu, Z. Luo, J. Zhang, T. Luo, J. Zhou, X. Zhao, K. Cai, Hollow mesoporous silica nanoparticles facilitated drug delivery via cascade pH stimuli in tumor microenvironment for tumor therapy, Biomaterials, 83 (2016) 51-65.

[3] M. Wu, Q. Meng, Y. Chen, L. Zhang, M. Li, X. Cai, Y. Li, P. Yu, L. Zhang, J. Shi, Large pore‐sized hollow mesoporous organosilica for redox‐responsive gene delivery and synergistic cancer chemotherapy, Advanced Materials, 28 (2016) 1963-1969.

[4] M. Yang, G. Wang, Z. Yang, Synthesis of hollow spheres with mesoporous silica nanoparticles shell, Materials Chemistry and Physics, 111 (2008) 5-8.

[5] L.P. Singh, S.K. Bhattacharyya, R. Kumar, G. Mishra, U. Sharma, G. Singh, S. Ahalawat, Sol-Gel processing of silica nanoparticles and their applications, Advances in Colloid and Interface Science, 214 (2014) 17-37.

[6] N. Pal, J.-H. Lee, E.-B. Cho, Recent trends in morphology-controlled synthesis and application of mesoporous silica nanoparticles, Nanomaterials, 10 (2020) 2122.

[7] Z. Teng, Y. Han, J. Li, F. Yan, W. Yang, Preparation of hollow mesoporous silica spheres by a sol–gel/emulsion approach, Microporous and Mesoporous Materials, 127 (2010) 67-72.

[8] Y. Li, J. Shi, Hollow‐structured mesoporous materials: chemical synthesis, functionalization and applications, Advanced Materials, 26 (2014) 3176-3205.

[9] H. Zhang, H. Xu, M. Wu, Y. Zhong, D. Wang, Z. Jiao, A soft–hard template approach towards hollow mesoporous silica nanoparticles with rough surfaces for controlled drug delivery and protein adsorption, Journal of Materials Chemistry B, 3 (2015) 6480-6489.

[10] M. Fuji, T. Shin, H. Watanabe, T. Takei, Shape-controlled hollow silica nanoparticles synthesized by an inorganic particle template method, Advanced Powder Technology, 23 (2012) 562-565.

[11] Y. Nakashima, C. Takai, H. Razavi-Khosroshahi, W. Suthabanditpong, M. Fuji, Synthesis of ultra-small hollow silica nanoparticles using the prepared amorphous calcium carbonate in one-pot process, Advanced Powder Technology, 29 (2018) 904-908.

[12] R.K. Rana, Y. Mastai, A. Gedanken, Acoustic cavitation leading to the morphosynthesis of mesoporous silica vesicles, Advanced Materials, 14 (2002) 1414-1418.

[13] W. Fan, L. Gao, Synthesis of silica hollow spheres assisted by ultrasound, Journal of Colloid and Interface Science, 297 (2006) 157-160.

[14] J. Fan, P. Du, X. Wang, P. Zheng, Z. Zhao, A. Duan, C. Xu, J. Li, Ultrasound-assisted synthesis of ordered mesoporous silica FDU-12 with a hollow structure, New Journal of Chemistry, 42 (2018) 2381-2384.

[15] S.-D. Jiang, G. Tang, Z. Bai, Y. Pan, Ultrasonic-assisted synthesis of hollow mesoporous silica as a toxic gases suppressant, Materials Letters, 247 (2019) 139-142.

[16] X. Liu, Z. Wu, R. Cavalli, G. Cravotto, Sonochemical preparation of inorganic nanoparticles and nanocomposites for drug release–A review, Industrial & Engineering Chemistry Research, 60 (2021) 10011-10032.

[17] R.F. Contamine, A. Wilhelm, J. Berlan, H. Delmas, Power measurement in sonochemistry, Ultrasonics Sonochemistry, 2 (1995) S43-S47.

[18] A. Chen, Y. Li, Y. Yu, Y. Li, K. Xia, Y. Wang, S. Li, L. Zhang, Synthesis of hollow mesoporous carbon spheres via "dissolution-capture" method for effective phenol adsorption, Carbon, 103 (2016) 157-162.

[19] Y. Teng, Y. Du, J. Shi, P.W. Pong, Magnetic iron oxide nanoparticle-hollow mesoporous silica spheres: fabrication and potential application in drug delivery, Current Applied Physics, 20 (2020) 320-325.

[20] M.E. Hoque, M. Shehryar, K.N. Islam, Processing and characterization of cockle shell calcium carbonate ($CaCO_3$) bioceramic for potential application in bone tissue engineering, Material Science & Engineering, 2 (2013) 132.

[21] X. Liu, Z. Wu, M. Manzoli, L. Jicsinszky, R. Cavalli, L. Battaglia, G. Cravotto, Medium-high frequency sonication dominates spherical-SiO_2 nanoparticle size, Ultrasonics Sonochemistry, 90 (2022) 106181.

[22] Y.-M. Zhao, G.-M. Tang, Y.-T. Wang, Y.-Z. Cui, Synthesis, spectroscopic studies, antimicrobial activity, and crystal structure of a Zn (II) complex based on voriconazole, Journal of Coordination Chemistry, 70 (2017) 189-200.

[23] S. Kakar, R. Singh, A. Semwal, Drug release characteristics of dosage forms: a review, Journal of Coastal Life Medicine, 2 (2014) 332-336.

[24] J.P. Raval, D.R. Naik, K.A. Amin, P.S. Patel, Controlled-release and antibacterial studies of doxycycline-loaded poly (ε-caprolactone) microspheres, Journal of Saudi Chemical Society, 18 (2014) 566-573.

[25] E. Mijowska, K. Cendrowski, M. Barylak, W. Konicki, Sandwich-like mesoporous silica flakes for anticancer drug transport-synthesis, characterization and kinetics release study, Colloids and Surfaces B: Biointerfaces, 136 (2015) 119-125.

[26] G. Singhvi, M. Singh, In-vitro drug release characterization models, International Journal of Pharmaceutical Studies and Research, 2 (2011) 77-84.

[27] J. Liu, S. Lin, L. Li, E. Liu, Release of theophylline from polymer blend hydrogels, International Journal of Pharmaceutics, 298 (2005) 117-125.

Chapter 6: Conclusions and Perspectives

In summary, the size of synthesized SSNs can be controlled by medium–high frequency sonication. Ultrasonic frequency, power, and temperature significantly affect SSN size and yield. SSN size decreased with increasing ultrasonic power at various frequencies (80, 120, and 500 kHz). The hydrodynamic diameters of 63–117 nm of SSNs were obtained under sonication with 80, 120, and 500 kHz. Moreover, the SSNs obtained were smaller at 120 kHz than at 80 kHz in a multi–frequencies ultrasonic reactor, and the SSN size decreased with increasing ultrasonic power at 20°C. With another 500 kHz ultrasonic bath, the optimal system temperature for producing smaller SSNs was proven to be 20°C. Also, the SSN size decreased with increasing ultrasonic power. The smallest SSNs (63 nm, hydrodynamic diameter by QELS, or 21 nm by FESEM) were obtained by sonication at 207 W for 20 min at 20°C. The number of active sites or microbubbles increased with the increasing ultrasonic frequency and power, thus TEOS and ammonia were more evenly distributed around the active site, resulting in smaller SSNs. SSN–synthesis scale–up is feasible in the same ultrasonic reactor, while the synthesis efficiency slightly fluctuates over the 50–200 mL range. Similarly, the larger number of microbubbles were generated with increasing temperature from 15 to 20°C resulted in smaller SSNs and lower yields. The particle size increased with the sonication time due to the increasing deposition thickness on the SSNs by unceasing hydrolysis and condensation with time. Moreover, the proportions of both ammonia and ethanol are critical factors for SSN formation even under sonication, and the active radicals generated during sonication may not be involved in the process. Compared with the traditional Stöber or low–frequency–sonication methods, medium–high frequency sonication can significantly reduce reaction time and reagent amounts with a low molar ratio of NH_4OH/TEOS (0.84).

Mesoporous silica materials with the core-shell structure were prepared by the ultrasonic-assisted method. The effects of ultrasonic frequency, ultrasonic power, ultrasonic time, ultrasonic volume, and bulk temperature on etching were discussed. There was a slight effect on etching with ultrasonic frequency and ultrasonic power. However, the effects of ultrasonic time and solution temperature on etching were significant. In addition, a microwave-assisted method was used to remove the surfactant of CTAB. The effects of microwave treatment time and temperature on the removal rate of surfactant were studied respectively. The results showed that the surfactant was completely removed by microwave at 80°C

for 5 min. Finally, the drug loading and release characteristics of HMSNs materials were studied by using the antifungal drug VOR as a model drug. The release kinetics of HMSNs materials were studied. The effects of temperature and pH on drug release were investigated respectively. The maximum VOR release of VOR-HMSNs was 65.1% and 68.2% at 37°C and 42°C, respectively. At pH 5.8, the amount of VOR released from the VOR-HMSNs material was similar at pH 7.4. The maximum VOR release of VOR-HMSNs was ca. 65%.

$CaCO_3$ particles were prepared under the action of low-frequency ultrasound. The effects of reactant concentration, ultrasonic time, ultrasonic power, and reactant volume on the particle size of the prepared $CaCO_3$ were investigated. Compared to stirring, small $CaCO_3$ particles were obtained with low-frequency ultrasonic. It had no significant effect of ultrasonic time on $CaCO_3$ particle size. They had optimal ultrasonic power and optimal reaction volume under sonication. The mechanism of preparing $CaCO_3$ under sonication was discussed. The nucleation rate of $CaCO_3$ by cavitation bubbles and the inhibition of crystal growth by hydroxyl radicals were discussed respectively. The surface of the cavitation bubble provided active sites for $CaCO_3$ nucleation resulting in the nucleation rate increasing. In addition, the generated hydroxyl radicals by sonication interacted with Ca^{2+} ions to inhibit the growth of crystals.

The nano-$CaCO_3$ templates and HMSNs were prepared by sonication at 19.5 kHz. Agglomerated nano-$CaCO_3$ template in the dry samples can be redispersed by sonication, which is beneficial to the coating of mesoporous silica. Under alkalic conditions, a double-template (hard template and soft template) method was used to prepare HMSNs with core-shell structure. The coating time of mesoporous silica was reduced to 40 min and the uniform particles of HMSNs (110-120 nm) were obtained by sonication. Structurally complete HMSNs were obtained by removing the hard template of $CaCO_3$. The obtained HMSNs have a high surface area (401.57 m^2/g), pore volume (0.11 cm^3/g), and uniform pore size (2.22 nm) that facilitated the effective encapsulation of antifungal drug VOR within HMSNs (7.96%). The VOR release kinetics from VOR-HMSNs material at pH 7.4 conforms to Fickian diffusion. The amount of VOR released increased with increasing temperature since the molecular mobility is temperature-dependent. The amount of VOR released from the VOR-HMSNs material was higher at pH 5.8 than that at pH 7.4. The maximum amount released of VOR from the VOR-HMSNs material was 92.37% at 480 min.

Appendix

1. Refereed Journal Publications

[1] **X. L. Liu**, Z. L. Wu, R. Cavalli, G. Cravotto*, Sonochemical Preparation of Inorganic Nanoparticles and Nanocomposites for Drug Release–A Review. Industrial & Engineering Chemistry Research, 2021, 60, 10011-10032.

[2] **X. L. Liu**, Z. L. Wu*, M. Manzoli, L. Jicsinszky, R. Cavalli, L. Battaglia, and G. Cravotto*, Medium-high frequency sonication dominates spherical-SiO2 nanoparticle size. Ultrasonics Sonochemistry, 2022, 90, 106181.

[3] S. K. Padhi, **X. L. Liu**, M. C. Valsania, L. Andreo, A. Agostino, A. Alessio, A. Giordana, Z. L. Wu, G. Cravottoa, M. Truccato*, Structure and Physicochemical Properties of MgB_2 Nanosheets Obtained Via Sonochemical Liquid Phase Exfoliation. (NANOSO-D-22-00533).

2. Conferences

Poster Communications

[1] **X. L. Liu**, Z. L. Wu, R. Cavalli, G. Cravotto*, Optimization of sonochemical synthesis of silica nanoparticles using Box-Behnken response surface design. Abstract for ESS-JSS-AOSS 1st Joint Sonochemistry Conference (2021).

[2] **X. L. Liu**, Z. L. Wu, R. Cavalli, and G. Cravottoa*, Sonochemical preparation of nanostructured calcium carbonate in a cup-horn reactor. Abstract for 17th Meeting of the European Society of Sonochemistry (2022).

Xiaolin Liu, Zhilin Wu, Roberta Cavalli and Giancarlo Cravotto. Sonochemical preparation of inorganic nanoparticles and nanocomposites for drug release–A review. Industrial & Engineering Chemistry Research, 60 (2021): 10011-10032.

Sonochemical Preparation of Inorganic Nanoparticles and Nanocomposites for Drug Release—A Review

Xiaolin Liu, Zhilin Wu, Roberta Cavalli, and Giancarlo Cravotto*

Cite This: *Ind. Eng. Chem. Res.* 2021, 60, 10011−10032

Read Online

ACCESS | Metrics & More | Article Recommendations

ABSTRACT: Inorganic nanoparticles (NPs) and nanocomposites (NCs) generally possess versatile properties, that is, good specific surface area (SSA), magnetism, easy functionalization with ligands, etc.; thus, such nanomaterials have rapidly been appearing in drug release and diagnosis. This review presents the sonochemical synthesis of nano-SiO_2, magnetic Fe_3O_4, graphene oxide, metal–organic frameworks, ZnO, $Ca_3(PO_4)_2$, and ZrP_2O_7, and their NCs. The cavitation effects, such as extremely high temperature and pressure, radical reactions, high-speed microjets, shock waves, deagglomeration, and strong hydrodynamic shear-forces at collapsing cavities assist the preparation of inorganic NPs and NCs. As compared to conventional hydrothermal synthesis, the ultrasound (US)-assisted method can shorten preparation time and reduce particle size. Moreover, the prepared NPs are much more uniform in size distribution and form. Most US-assisted prepared NPs and NCs were proven to be appropriate as drug nanocarriers. Also, the drug release mechanisms are briefly presented and discussed. Furthermore, the effects of ultrasonic equipment, power, sonication time, substrate concentration, pH value, and surfactants on the characteristics and morphology of NPs and NCs are summarized.
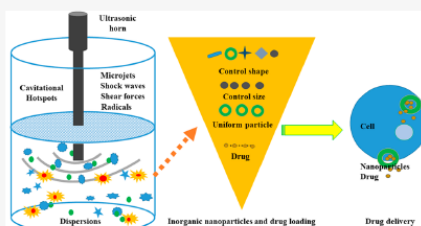
1. INTRODUCTION

Increasing attention has been recently paid to the preparation and application of nanoparticles (NPs) and nanocomposites (NCs).[1] Inorganic NPs are often delimited in the particle sizes of 1−100 nm, thus they can possess unusual physicochemical and biological characteristics.[2−7] Therefore, inorganic NPs and NCs have been widely used in chemical,[8−18] biological,[19−26] electronic sensing,[27−30] and medical fields.[31−43]

1.1. Inorganic Nanomaterials for Drug Release. Recently, nanotechnology has rapidly been emerging as a useful tool for the drug release and diagnosis, since inorganic NPs and NCs generally possess versatile properties, that is, good specific surface area (SSA), magnetism, and easy functionalization with ligands, to enhance the controlled targeted drug delivery. Therefore, inorganic NPs, such as gold,[44] semiconductor nanocrystals,[45] superparamagnetic NPs,[46] zinc oxide NPs,[47] silicon NPs,[48] and their NCs have been frequently applied in controlled drug release. The drug release strategy is usually intended to be stimuli-responsive, which includes internal and external stimuli (Figure 1).[49]

Compared to normal tissues, lesion cells may modify the surrounding environment, such as pH value and enzyme content. Various drug-release systems have been developed to respond to internal stimuli in accordance with the above-mentioned physiological basis. As shown in Figure 1, the internal drug release strategy includes pH-, enzyme-, and

redox-responsiveness.[50−52] So far the pH-responsive effect has been widely studied.[53−57] The pH value might decrease around lesion cells and the acidified environment usually causes the protonation of drugs and weakens electrostatic interactions and hydrogen-bond interactions between the nanocarrier and the drug, etc. After cell internalization, the lower pH can initiate the conjugation and release of the drug on the nanocarriers.[58] By contrast, the drug conjugated nanocarrier is stable at pH 7.4. In addition, the core/shell NCs with pH-sensitive polymer were also used to control the drug release.[59]

External stimuli principally include light, heat, ultrasound (US), and magnetic fields, etc.[60−63] Relevant aspects of the temperature-responsive effect have been extensively reported.[64−67] The drug release dependent on the temperature is attributed to the gel swelling and shrinking.[68] In general, temperature-sensitive polymers can be used to encapsulate the inorganic NPs, in which the phase transition occurs at ca. 306 K. The gel swells when hydrogel incorporates water below
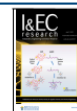
Xiaolin Liu, Zhilin Wu, Maela Manzoli, László Jicsinszky, Roberta Cavalli, Luigi Battaglia, Giancarlo Cravotto. Medium-high frequency sonication dominates spherical-SiO2 nanoparticle size. Ultrasonics Sonochemistry 90 (2022): 106181.

Medium-high frequency sonication dominates spherical-SiO$_2$ nanoparticle size

Xiaolin Liu, Zhilin Wu [*], Maela Manzoli, László Jicsinszky, Roberta Cavalli, Luigi Battaglia, Giancarlo Cravotto [*]

Department of Drug Science and Technology and NIS–Centre for Nanostructured Interfaces and Surfaces, University of Turin, Via Pietro Giuria 9, 10125 Turin, Italy

ARTICLE INFO

ABSTRACT

Spherical SiO$_2$ nanoparticles (SSNs) have been inventively synthesized using the Stöber method with sonication at medium–high frequencies (80, 120, and 500 kHz), aiming to control SSN size and shorten reaction time. Compared to the conventional method, such sonication allowed the Stöber reaction complete in 20–60 min with a low molar ratio of NH$_4$OH/tetraethyl orthosilicate (0.84). The hydrodynamic diameters of 63–117 nm of SSNs were obtained under sonication with 80, 120, and 500 kHz of ultrasonic frequencies. Moreover, the SSNs obtained were smaller at 120 kHz than at 80 kHz in a multi-frequencies ultrasonic reactor, and the SSN size decreased with increasing ultrasonic power at 20 °C, designating the sonochemical unique character, namely, the SSN-size control is associated with the number of microbubbles originated by sonication. With another 500 kHz ultrasonic bath, the optimal system temperature for producing smaller SSNs was proven to be 20 °C. Also, the SSN size decreased with increasing ultrasonic power. The smallest SSNs (63 nm, hydrodynamic diameter by QELS, or 21 nm by FESEM) were obtained by sonication at 207 W for 20 min at 20 °C. Furthermore, the SSN size increased slightly with increasing sonication time and volume, favoring the scale-up of SSNs preparation. The mechanisms of controlling the SSN size were further discussed by the radical's role and effects of ammonia and ethanol concentration.

1. Introduction

Spherical SiO$_2$ nanoparticles (SSNs) are widely applied in biomedical fields including biosensors, DNA transfection, cancer treatment, etc [1–3]. The Stöber process, via the hydrolysis and polycondensation of tetraethyl orthosilicate (TEOS) in alkaline ethanol (Scheme. 1), is a common method for the preparation of monodisperse SSNs [4,5]. In the conventional process, SSN size is modulated by many factors, such as the ethanol/NH$_4$OH/TEOS/H$_2$O ratio, reaction temperature and time, etc.

Ismai *et al.* explored the effects of TEOS (0.2–0.4 mol/L) and ammonia (0.11–0.3 mol/L) concentrations on SSN size [6]. Both the hydrolysis and condensation rates become faster with increasing TEOS and ammonia concentrations, producing fewer nuclei and larger particle size. Under the optimal conditions, 50 nm silica particles were obtained with 0.2 mol/L ammonia and 0.2 mol/L TEOS at ambient temperature for 24 hrs. Wang *et al.* also studied the effect of TEOS (0.22–1.115 mol/L) and ammonia concentrations on silica particle size in the mixture of water and isopropanol [7]. With a constant NH$_4$OH/TEOS molar ratio

(0.81), 30 nm or 860 nm silica particles were obtained with 0.22 mol/L or 1.115 TEOS at 20 °C for 5 hrs, respectively. As a catalyst, higher ammonia accelerates the hydrolysis and condensation and promotes the production of more oligomers to form larger particles. It is conspicuous that smaller SSNs are obtained with the lower NH$_4$OH/TEOS molar ratio, but long reaction times (5–24 hrs) are required, whereas the higher reaction rate with the higher NH$_4$OH/TEOS molar ratio leads to larger particle sizes (ca. 800 nm) [5]. The sonochemical method has long been used in the preparation of nanoparticles and nanocrystals to accelerate the synthesis and reduce nanoparticle size [8–11]. Ultrasonic cavitation is generally regarded as the origin of sonochemistry, namely, the implosion of cavitation microbubbles generates extremely high local temperature and pressure, high-speed microjets, strong shock waves, and shear forces, which contribute to the fabrication of nanostructured materials [12,13]. The number and size of cavitation bubbles are also critical for the fabrication of nanostructured materials. The cavitation bubble surfaces can act as crystal nucleation sites, leading to increasing nucleation rates [14–16]. Therefore, the reduction in crystal size and the

ESS-JSS-AOSS 1st Joint Sonochemistry Conference (ONLINE), 2021

ESS-JSS-AOSS 1st JOINT SONOCHEMISTRY CONFERENCE (ONLINE)

Nov 8-10, 2021

UNIVERSITÀ DEGLI STUDI DI TORINO

Optimization of sonochemical synthesis of silica nanoparticles using Box-Behnken response surface design

University of Turin

PhD Candidate: Xiaolin Liu

Tutor: Prof. Giancarlo Cravotto

Prof. Roberta Cavalli

Co-tutor: Dr. Zhilin Wu

1

ESS-JSS-AOSS 1st Joint Sonochemistry Conference

Optimization of sonochemical synthesis of silica nanoparticles using Box-Behnken response surface design

Xiaolin Liu[a], Zhilin Wu[a], Roberta Cavalli[a], and Giancarlo Cravotto[a,*]
[a] Department of Drug Science and Technology, University of Turin, Italy
*Email: giancarlo.cravotto@unito.it

Ultrasonic strategy for the preparation of inorganic nanoparticles and controlled drug release.

Introduction
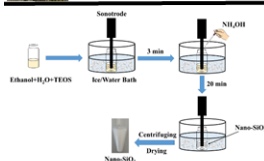
Non-toxic and odourless nanosilica (nanoSiO₂) been widely used in plastics, rubber, fine ceramics, optoelectronic and biomedical materials. The uniform and monodispersed spherical silica nanoparticles were conventionally prepared by catalytical hydrolysis and condensation of tetraethyl orthosilicate (TEOS) with NH_4OH in aqueous ethanol solution. Reactions required several hours. In this study, sonochemical synthesis was used to prepare nanoSiO₂ particles to shorten reaction time at 20 kHz and 70 W. The influences of NH_4OH, TEOS and ethanol concentrations on nanoparticle size of nanoSiO₂ were investigated by using response surface design.

Results and Discussion
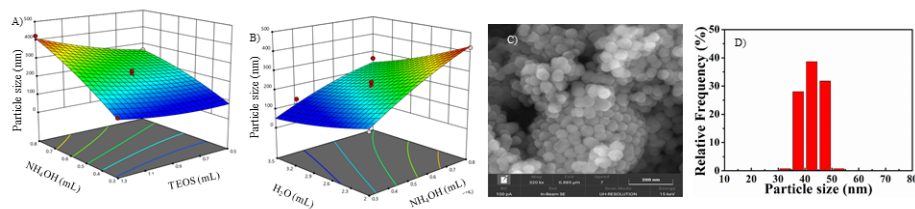
A) The effect of NH_4OH for the particle size of nanoSiO₂. B) The effect of H_2O for the particle size of nanoSiO₂. C) FESEM of nanoSiO₂. D) Particle size of nanoSiO₂.

Conclusion

The particle size of nanoSiO₂ increased obviously with the amount of NH_4OH and TEOS, in contrary, decreased with the increasing amount of H_2O. However, ethanol volume slightly affected the particle size of nanoSiO₂.

17th Meeting of the European Society of Sonochemistry, Jena, Germany, 2022

17th Meeting of the European Society of Sonochemistry

28/08/2022 - 01/09/2022 Friedrich-Schiller-Universität, Jena, Germany

UNIVERSITÀ DI TORINO

Sonochemical preparation of nanostructured calcium carbonate in a cup-horn reactor

Xiaolin Liu, Zhilin Wu, Roberta Cavalli, Maela Manzoli, and Giancarlo Cravotto*

Department of Drug Science and Technology, University of Turin, Italy

*Email: giancarlo.cravotto@unito.it

Introduction

The micro- and nanostructured calcium carbonate has been widely used in pigments, rubber, cosmetics, biomaterials, etc. The microparticles of $CaCO_3$ were conventionally obtained by the reaction of calcium chloride and sodium carbonate with stirring and the particle size of $CaCO_3$ reached in the range of 3-15 µm.[1, 2] Ultrasound has been used in the preparation of a wide range of solid materials, taking advantage of the various effects arising from cavitation.[3-5] The main advantage of sonication is to greatly accelerate the reactions. Both size and shape of particles are probably controlled by varying the sonication conditions.[3] In this study, an ultrasonic cup-horn apparatus (home-made) was used to prepare nanoparticles of $CaCO_3$ by sonication at 19.5 kHz, aiming to reduce the particle size and reaction time.
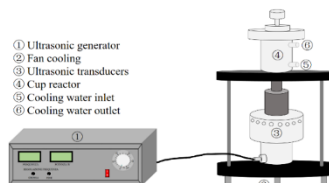
Methods

① Ultrasonic generator
② Fan cooling
③ Ultrasonic transducers
④ Cup reactor
⑤ Cooling water inlet
⑥ Cooling water outlet

Fig. 1. Ultrasonic cup-horn apparatus (home-made, 19.5 kHz).

In typical runs, 0.1 M Na_2CO_3 solution was dropwise added to 0.1 M $CaCl_2$ solution in an ultrasonic cup-horn reactor first, and then sonicated at various powers, reactive volumes, and times under an air atmosphere. The temperature of the ultrasonic reactor was maintained by cooling water.

Characterization: The hydrodynamic particle sizes of $CaCO_3$ were measured in water via the Quasi Elastic Light Scattering (QELS) method at 25℃ using particle sizing Brookhaven Instruments (Holtsville, NY, USA) with the software of 90plus/BI-MASS. The scattering angle and operating wavelength were 90° and 675.0 nm, respectively. Ultra-high resolution Field Emission Scanning Electron Microscope (FESEM) measurements were performed on a Tescan S9000G FESEM 3010 microscope (30 KeV) equipped with a high-brightness Schottky emitter. The morphology of $CaCO_3$ was observed by FESEM.
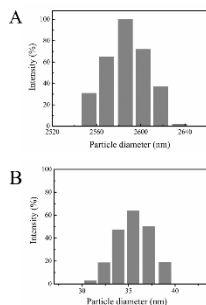
Results

Fig. 2. Hydrodynamic particles size distribution of $CaCO_3$ obtained with stirring (A) and sonicated (B). Conditions: 10 mL of 0.1 M Na_2CO_3 solution was dropwise added to 10 mL. of 0.1 M $CaCl_2$ solution and stirred (450 rpm) or sonicated at 55 W for 3 min.

As shown in Fig. 2, the particle sizes of $CaCO_3$ obtained by sonication were much smaller than those obtained with stirring.
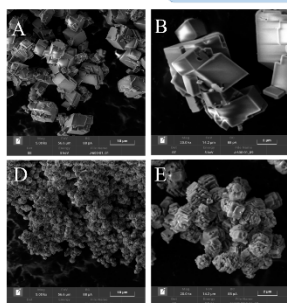
Fig. 3. FESEM images of the $CaCO_3$ obtained with stirring (A and B) and sonicated (D and E). Conditions: 10 mL of 0.1 M Na_2CO_3 solution was dropwise added to 10 mL of 0.1 M $CaCl_2$ solution and stirred (450 rpm) or sonicated at 55 W for 3 min.

As shown in Fig. 3, the $CaCO_3$ particles obtained under sonication are in the form of flakes, while the $CaCO_3$ particles obtained under stirring are in the form of lumps. And the particle sizes of $CaCO_3$ obtained under sonication are significantly reduced compared with stirring.
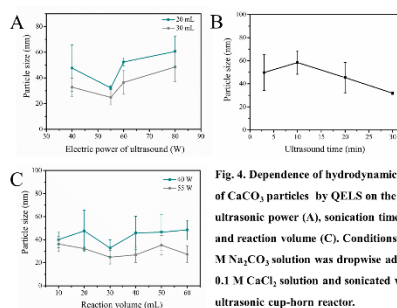
Fig. 4. Dependence of hydrodynamic size of $CaCO_3$ particles by QELS on the ultrasonic power (A), sonication time (B), and reaction volume (C). Conditions: 0.1 M Na_2CO_3 solution was dropwise added to 0.1 M $CaCl_2$ solution and sonicated with ultrasonic cup-horn reactor.

As shown in Fig. 4A, the particle size generally decreased with the ultrasonic power, but the smallest particle size was obtained when the ultrasonic power was 55 W.

As shown in Fig. 4B, the particle size generally decreased with the sonication time, but the largest particle size was obtained when the sonication time was 10 min.

As shown in Fig. 4C, the particle size slightly fluctuate with various sonication volumes at both 40 W and 55 w of ultrasonic power, while the smallest particle size was obtained with 30 mL of the sonication volume.

Conclusion

In summary, the particle size of synthesized $CaCO_3$ can be controlled by sonication. Ultrasonic power, sonication time, and reaction volume significantly affect the particle size of $CaCO_3$. Under the optimum reaction conditions, the smaller particle sizes (hydrodynamic particles size: ca 25 nm) were obtained with 30 mL of reaction volume under sonication at 19.5 kHz and 55 W for 3 min.

References

[1] D.B. Trushina, T.V. Bukreeva and M.N. Antipina, Size-controlled synthesis of vaterite calcium carbonate by the mixing method: aiming for nanosized particles. *Cryst. Growth Des.* 16 (2016) 1311-1319.

[2] J. Yu, M. Lei, B. Cheng and X. Zhao, Facile preparation of calcium carbonate particles with unusual morphologies by precipitation reaction. *J. Cryst. Growth* 261 (2004) 566-570.

[3] K.S. Suslick, and G.J. Price, Applications of ultrasound to materials chemistry. *Annu. Rev. Mater. Sci.* 29 (1999) 295-326.

[4] A. Gedanken, Using sonochemistry for the fabrication of nanomaterials. *Ultrason. Sonochem.* 11 (2004) 47-55.

[5] X.L. Liu, Z.L. Wu, R. Cavalli, and G. Cravotto, Sonochemical Preparation of Inorganic Nanoparticles and Nanocomposites for Drug Release–A Review. *Ind. Eng. Chem. Res.* 60 (2021) 10011-10032.

Resume

Personal Data|Information

Name: Liu Xiaolin   Gender: Male

Native Place: Linyi City, Shandong Province, China   Date of Birth: 06/03/1990

Folk: Han   Marital Status: unmarried

Education: Masters's degree   Major: Chemical Technology

English Level: CET-4 grade   Computer Level: CCT

Mobile: +39 3395645898   E-mail: xiaolin.liu@unito.it xlin.liu@hotmail.com

Education Experience

2019- Now	Turin University	Pharmaceutical and Biomolecular Sciences	Ph.D Student
2015.9-2018.7	Changzhou University	Major in Chemical Technology	Master Student
2011.9-2015.7	Jining University	Major in Chemical Engineering & Technology	Bachelor Student

Research|Work Experience

◎ 2018-2019   Lunan Pharmaceutical Group Corporation   Laboratory Researcher

Professional Skills

◎ Proficient in the literature review
◎ Analysis with HPLC, GC, UV,
◎ Specialized software: Origin, ChemBio Office, Nano Measure, Aspen Plus, AutoCAD, etc.

Hobby

◎ Cuisine, table tennis, billiards, jogging, mountain climbing

Awards

◎ 2018   Excellent thesis for the master's degree
◎ 2017   National Scholarship
◎ 2015   Provincial Outstanding Graduate, Excellent thesis for the master's degree
◎ 2014.08   Second Prize in The 8th National College Students Chemical Engineering Design Competition
◎ 2014.07   Second Prize in The 3rd Shandong College Students Chemical Process Experiment Skills
                  Competition

Scientific Research Achievements

Dissertation
1. Construction and property research of new drug delivery platform based on mesoporous silica. (Master)
2. The Design of Heat Exchange Network on 25 wt/a P-xylene. (Bachelor)

Publications
1. **Xiaolin Liu**, Dan Shou, Chuanxiang Chen, Huihui Mao, Yong Kong, Yongxin Tao, Construction of magnetic-targeted and NIR irradiation-controlled drug delivery platform with $Fe_3O_4@Au@SiO_2$ nanospheres. ***Materials Science & Engineering C***, **2017**, 81, 206-212.
2. **Xiaolin Liu**, Yongxin Tao, Huihui Mao, Yong Kong, Jian Shen, Linhong Deng, Linsong Yang, Core-shell structured polypyrrole/mesoporous SiO_2 nanocomposite capped with graphene quantum dots as gatekeeper for irradiation-controlled release of methotrexate. ***Ceramics International***, **2017**, 43, 5061-5067.
3. K. Zhang, C. Ding, **X. L. Liu**, J. Gao, D. Wu, Y. Qin, and Y. Kong, A redox and pH dual-triggered drug delivery platform based on chitosan grafted tubular mesoporous silica. **Ceramics International, 2019**, 45, 22603-22609.
4. Y. Yao, C. Ding, J. Gao, D. Wu, **X. L. Liu**, Y. Qin, and Y. Kong, Construction of Near-infrared Irradiation-controlled Drug Delivery System Based on Silica@ polypyrrole@ mesoporous Silica and PEG-PCL-PEG. **Bulletin of the Korean Chemical Society, 2019**, 40, 917-920.
5. **X. L. Liu,** Z. L. Wu, R. Cavalli, G. Cravotto*, Sonochemical Preparation of Inorganic Nanoparticles and Nanocomposites for Drug Release–A Review. **Industrial & Engineering Chemistry Research** 2021, 60, 10011-10032.
6. **X. L. Liu**, Z. L. Wu, R. Cavalli, G. Cravotto*, Optimization of sonochemical synthesis of silica nanoparticles using Box-Behnken response surface design. Abstract for ESS-JSS-AOSS 1st Joint Sonochemistry Conference (2021).
7. **X. L. Liu**, Z. L. Wu, R. Cavalli, and G. Cravottoa*, Sonochemical preparation of nanostructured calcium carbonate in a cup-horn reactor. Abstract for 17th Meeting of the European Society of Sonochemistry (2022).
8. **X. L. Liu**, Z. L. Wu*, M. Manzoli, L. Jicsinszky, R. Cavalli, L. Battaglia, and G. Cravotto*, Medium-high frequency sonication dominates spherical-SiO_2 nanoparticle size. **Ultrasonics Sonochemistry 2022**, 90, 106181.
9. S. K. Padhi, **X. L. Liu**, M. C. Valsania, L. Andreo, A. Agostino, A. Alessio, A. Giordana, Z. L. Wu, G. Cravottoa, M. Truccato*, Structure and Physicochemical Properties of Mgb_2 Nanosheets Obtained Via Sonochemical Liquid Phase Exfoliation. **Available at SSRN** 4229397.

Patents
1. A novel alginic acid/calcium ion/graphene oxide composite gel applied to pH and electrically regulated drug delivery. CN 107115269 A (China, 2017.09.01)
2. A novelchitosan/carboxymethyl cellulose-calcium ion-graphene oxide composite for drug delivery with pH regulation. CN 107096035 A (China, 2017.08.29)
3. Preparation of a chitosan/carboxymethyl cellulose-calcium ion-graphene oxide composite. CN 107022117 A (China, 2017.08.08)
4. A core-shell structure of polypyrrole/mesoporous silica/graphene quantum dots nanocomposite for drug delivery. CN 106974882 A (China, 2017.07.25)
5. Preparation method of polypyrrole/mesoporous silica/graphene quantum dot nano composite material with core-shell structure. CN 106727274 A (China, 2017.05.31)
6. A novel Fe_3O_4/Au/SiO_2 nanocomposite for targeted control drug delivery with NIR light irradiation. CN 106511299 A (China, 2017.03.22).